Understanding Elastin-Like Polypeptide Block Copolymer Self-assembly Behavior

by

Wafa Hassouneh

Department of Biomedical Engineering
Duke University

Date:_____

Approved:

_____
Ashutosh Chilkoti, Supervisor

_____
Stefan Zauscher

_____
Gabriel Lopez

_____
Michael Rubinstein

_____
Thomas LaBean

Dissertation submitted in partial fulfillment of
the requirements for the degree of Doctor
of Philosophy in the Department of
Biomedical Engineering in the Graduate School
of Duke University

2013

ABSTRACT

Understanding Elastin-Like Polypeptide Block Copolymer Self-assembly Behavior

by

Wafa Hassouneh

Department of Biomedical Engineering
Duke University

Date:_____
Approved:

_____
Ashutosh Chilkoti, Supervisor

_____
Stefan Zauscher

_____
Gabriel Lopez

_____
Michael Rubinstein

_____
Thomas LaBean

An abstract of a dissertation submitted in partial
fulfillment of the requirements for the degree
of Doctor of Philosophy in the Department of
Biomedical Engineering in the Graduate School of
Duke University

2013

Abstract

Elastin-like polypeptides (ELPs) are thermally responsive polymers composed of the pentapeptide repeat Valine-Proline-Glycine-X-Glycine where X is any amino acid except proline. ELP diblocks have been engineered by creating two ELP blocks with hydrophilic and hydrophobic guest residues. The hydrophobic block desolvates at a lower temperature and forms the core of a micelle while the still hydrated hydrophilic block forms the corona. ELP micelles are promising drug delivery vehicles for cancer therapeutics. ELP diblocks offer a unique method to display targeting proteins multivalently on micelles to improve tumor cell uptake. As ELPs are genetically encoded, proteins can be seamlessly fused at the genetic level to the ELP diblock. The protein ELP diblock fusions can be synthesized as one polypeptide chain that is of precise molecular weight and highly monodisperse, and no post-synthesis modification is necessary. Self-assembly behavior of ELP diblocks is known to tolerate fusion to small peptides (< 10 amino acids) but their self-assembly behavior has not be examined when fused to proteins that are 100-200 amino acids. Here, we hypothesize that molecular weight of the protein and the surface properties of the protein will be factors in determining its effect on ELP diblock self-assembly. In addition, the ELP block lengths and composition are hypothesized to be factors in the self-assembly behavior of protein ELP diblock fusions. This hypothesis is tested by fusing four proteins with different

properties to various ELP diblocks and characterizing their self-assembly behavior. The proteins were found to dominate the self-assembly behavior. Proteins that disrupted self-assembly did so for all ELP diblock lengths and compositions. Protein that did not disrupt self-assembly behavior affected the thermal behavior of the hydrophilic block. Hydrophilic proteins increased the micelle-to-aggregate transition temperature while hydrophobic proteins decreased it. We also sought to understand the self-assembly of ELP diblocks on a theoretical basis. A previously developed model for the self-assembly of synthetic polymers was applied to our polypeptide system. Two parameters, solvent quality of the corona and surface tension of the hydrophobic block, were experimentally measured and used to fit the model. Predictions of micelle radius and aggregation numbers were in good agreement with experimental data. However, the corona was found to be unstretched compared to its Gaussian size by this model. Therefore, a new model was developed describing what is termed as weak micelles in which the corona is not stretched but rather close to Gaussian size. The weak micelle model prediction were also in good agreement with experimental data suggesting that ELP micelles are in the crossover regime between the previous model and the new model.

Dedication

This dissertation is dedicated to Saadat, Kamilia and Samar.

Contents

List of Tables

List of Figures

Acknowledgements

I would like to acknowledge Professor Manfred Schmidt and Dr. Karl Fischer from University of Mainz (Germany) who were instrumental in obtaining the initial light scattering data and whose continued guidance during my subsequent light scattering experiments was a great learning opportunity. In addition, I would like to thank Robert Branscheid for his help in obtaining cryo-TEM images at University of Mainz. I would like to thank Dr. Ekaterina Zhulina and Professor Michael Rubinstein at University of North Carolina for their collaboration on applying their theoretical understanding of micelles to ELPs and their patience in familiarizing me with the world of polymer physics. I would like to also thank Kevin Vargo and Professor Dan Hammer at University of Pennsylvania for their help and expertise in imaging ELP particles with cryo-TEM. I would like to thank my advisor, Professor Ashutosh Chilkoti for his guidance and support through this process. To the labmates who have helped me along the way in experiments and in discussions, thank you.

1. Introduction

1.1 Elastin-like polypeptides and their lower critical solution temperature behavior

Elastin-like polypeptides (ELPs) are biopolymers derived from the hydrophobic domains of tropoelastin, a soluble precursor of the extracellular matrix component elastin[1, 2]. ELPs are composed of the pentapeptide repeat [Valine-Proline-Glycine-X-Glycine] where X is a guest residue that can be any amino acid except proline. The pentapeptide can be repeated anywhere from 10 to 330 times[3]. These polypeptides are genetically encoded and are thus expressed in and purified from *Escherichia coli (E. coli)*. As the genes encoding ELPs are constructed through recombinant DNA techniques, precise chain length and guest residue composition can be attained. Expression of the ELP gene results in a highly monodisperse polymer[4, 5]. Genetic encoding of ELPs also allows spatial control over the guest residues along the backbone of the polypeptide chain. Therefore, residues with functional side chains for conjugation such as cysteine[6, 7] can be placed at precise positions along the chain, and architectures such as block copolymers and random copolymers can be generated systematically[8, 9]. In addition, biological functionality can be linked to ELPs through seamless fusion of proteins or peptides at the genetic level at the N or C terminus of the ELP[10, 11] or embedded along the polypeptide[12, 13].

ELPs are temperature-responsive polymer as they exhibit lower critical solution temperature (LCST) behavior. For a given solution composition, below the cloud point,

the solution is homogenous and the polymer is soluble[14, 15]. As temperature is increased above the cloud point, the attraction between monomers dominates causing the solution to phase separate and an ELP-rich sediment forms. The phase transition is sharp and reversible upon cooling[10, 15]. This phase transition as related to the change in interaction between monomers with temperature is detailed below.

The interaction between two monomers at a given temperature is determined by their hard-core repulsion (negative potential well) and their attraction (positive potential well). These two contributions define the interaction potential expressed as a function of the distance between the two monomers (r), U(r). Excluded volume (v) is defined as the negative integral of the difference between the Boltzmann factor of U(r) and that of monomers at an infinite distance.

$$\mathrm{v} = -\int \left(\exp\left[-\frac{U(r)}{kT}\right] - 1\right) d^3r$$

The excluded volume decreases with temperature for an LCST polymer going from positive (good solvent) to zero (theta solvent) to negative (poor solvent). In good solvent, the polymer adopts an extended conformation. In theta solvent, the polymer conformation is that of a self-avoiding random walk. In poor solvent, the polymer collapses and forms globules (and phase separates)[14].

If the attraction between monomers is stronger than that between monomer-solvent then an attraction well exists. In good solvent, the attraction well is smaller than the hard-core repulsion ($v > 0$) causing the polymer to swell to an extended

conformation. In theta solvent, the attraction well and the hard-core repulsion cancel (v = 0) and the polymer chain adopts a self-avoiding walk conformation resulting in a Gaussian end-to-end distance (R_G), which is smaller than the end-to-end distance of a chain in good solvent. The polymer chain remains in Gaussian conformation within a temperature range around the theta-temperature for which the increase or decrease in the attraction well results in a net potential for the chain that is smaller than the thermal energy, kT, and thus the interactions are insufficient to swell or collapse the chain. As such, it is important to define a thermal length scale, or as referred to herein, the thermal blob. On length scales smaller than the thermal blob, the interactions energy between monomers along a chain, as defined by the excluded volume, are weaker than the thermal energy, kT. Therefore, the conformation of the segments of the chain smaller than the thermal blob scale is near Gaussian. In the theta regime, the thermal blob is larger than the end-to-end distance of the polymer chain and thus the entire chain is Gaussian[14].

Outside the theta regime, the attraction well is larger than the hard-core repulsion well ($v < 0$) and the monomers attract each other and collapse into globules. The globules are in contact with the solvent and that incurs an energetic cost due to surface tension. The globules minimize this cost by forming a polymer-rich sediment phase. A fraction of the chains remain is solution as globules as their surface energy is balanced by their translational entropy. The sediment phase has a high volume fraction

(ϕ'') while the globule phase has a low volume fraction (ϕ') (Figure 1). The boundary that distinguishes the one-phase from two-phase regimes within the phase diagram of temperature versus composition is known as the binodal (Figure 1). The binodal curve relates the solution composition to its cloud point (otherwise referred to as the transition temperature). The shape of the binodal indicates that an increase in polymer solution concentration will decrease the cloud point for compositions below a critical concentration (ϕ_c, lowest point on binodal). Above this critical concentration, a further increase in concentration leads to an increase in the cloud point[12].

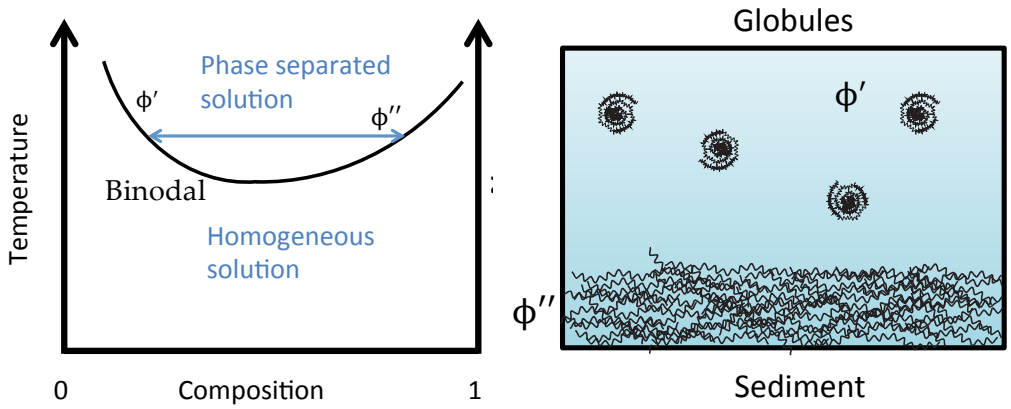

Figure 1: Schematic of LCST polymer phase diagram of temperature versus composition and the binodal that separates one-phase from two-phase regions (right) and a representation of a two-phase solution composed of a sediment and globules (left).

In addition to temperature and concentration, the ELP thermal behavior depends on the number of pentapeptides and the composition of the guest residues. An increase in N, the polymerization degree, shifts the phase boundary (binodal) to lower temperature values and the critical concentration (lowest point on binodal) shifts to

smaller solution compositions[3]. The guest residue also affects the phase diagram, as more hydrophobic residues such as tryptophan and phenylalanine will shift the binodal downward (i.e. to lower cloud point) while more hydrophilic residues such as serine will shift the binodal upward (i.e. to higher cloud point) as different guest residues will result in different interaction parameters[2, 4, 16].

The last factor to consider in relation to ELP thermal behavior is the ionic strength of the solution. As with proteins and other LCST polymers such as Poly(N-isopropylacrylamide), ELPs are sensitive to the types of ions in solution and ionic strength of the solution[17-20]. ELPs are more sensitive to salts compared to folded globular proteins. The effect of ions on ELPs follows the trend described by the Hofmeister series[19]. Anions exert a much larger effect compared to cations. Anions below Cl^- on the series are known as chaotropes and destabilize proteins and increase solubility. Anions above Cl^- on the series are known as kosmotropes and stabilize proteins and reduce solubility. Increased concentration of kosmotropes decreases the transition temperature of ELPs and thus salts such as NaCl and sodium citrate are used to trigger the phase separation of ELP solutions.

Urry and coworkers have previously determined the phase diagram of ELP with valine as a guest residue in water (Figure 2) [15, 21, 22]. ELP was chemically synthesized through a polymerization reaction and dialyzed with a 50 kDa molecular weight cut-off which yields ELP chains with approximately 120 pentapeptides and greater[21]. The

binodal was determined by measuring the increase in turbidity of a solution as temperature is increased with quasi-elastically scattered light (QELS)[21, 22]. The critical temperature (LCST) was found to be 28 °C and the critical concentration to be approximately 0.16[21]. The binodal curve for compositions above the critical composition is shallow. In addition, through fitting the Flory-Huggins model for phase diagrams, the ELP chain was approximated as a chain with an effective 50 segments that are independent freely-rotating segments[22]. The number of segments is smaller than the number of amino acids and pentapeptides in the ELP chain indicating a degree of stiffness in the chain. The stiffness is predicted to be due to the increase in type II β-turns in ELPs as evidenced by circular dichroism data collected at increasing temperatures[22].

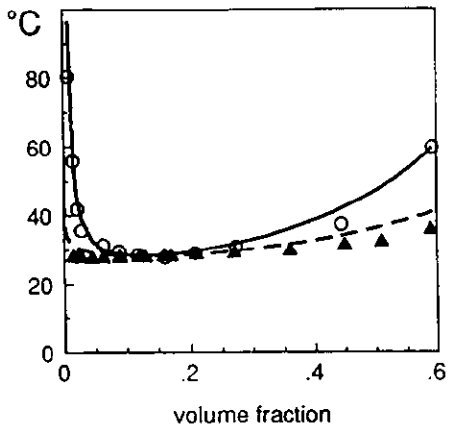

Figure 2: Phase diagram of $[VPGVG]_n$ where n ≈ 120 of temperature versus volume fraction. The circles are points on the spinodal while the triangles are points on the binodal. Adapted from Sciortino et al. 1993[22].

A polymer chain can be considered as composed of a number of freely-rotating segments at which the chain can change its direction; each segment is composed of a

number of monomers and the length of the segment is referred to as the Kuhn length[14]. The Kuhn length of an ELP with guest residue valine was experimentally determined by Schmidt and coworkers[23]. The Kuhn length was determined by measuring the hydrodynamic radius of dilute solutions at 20 °C with increasing ELP length using dynamic light scattering. ELPs with 20, 30, 40, 60 and 120 pentapeptides were used for this study. The fit of the hydrodynamic radius versus number of amino acids in the chain was used to fit the Kratky-Porod wormlike chain model. The amino acid monomer average size was estimated to be 0.365 nm (as estimated from known peptide bonds and angles). The Kuhn length was found to be 2.3 nm for an assumed chain cross-section of 1 nm. As consistent with Urry and coworkers' study, the ELP chain was found to have an inherent degree of stiffness, as the Kuhn length is greater than a pentapeptide's contour length.

1.2 Polypeptide self-assembly

The self-assembly behavior of a multitude of peptide-based systems has been explored as they are an interesting class of biomaterials for biomedical applications[24]. Different polypeptide sequences, lengths and architectures lead to the formation of different secondary structures and different self-assembled morphologies. The examples below will highlight a few of these polypeptide-based systems and the wide range of self-assembly behavior observed. Polypeptide diblocks studied by Deming and coworkers[25-27] such as the poly-lysine-poly-leucine diblocks formed micron sized vesicles

due to the combination of the highly charged corona and the α-helical structure of the hydrophobic block. The length of the two blocks and their ratio affected the observed morphology. An optimal hydrophobic block length was found for which the α-helical structure prefers to align and minimize curvature driving the formation of vesicles and sheet-like membranes[25]. Others have utilized the α-helical structure as well by engineering the self-assembly of coiled-coil sequences, heptapeptides that form an amphiphilic α-helix and associate with other heptapeptides to shield their hydrophobic side[28-30]. Polypeptides composed of repeats of coiled-coil sequences were engineered and were found to form α-helical fibers due to the staggering of the heptapeptide sequences along the fiber. Shorter amphiphilic peptides composed of a head of one or two hydrophilic charged residues (such as aspartic acid) followed by a tail of 4-6 hydrophobic residues (such as leucine or valine), such as those studied by Zhang and coworker, were found to self-assemble into nanovesicles and nanotube structures[31-33].

While the examples above are of chemically synthesized polypeptides, a unique class of polypeptides is elastomeric materials such as silk-like polypeptide, resilin-like polypeptides and elastin-like polypeptide, which can be genetically synthesized[34, 35]. Silk-like polypeptides are composed of GAGAGS repeats and self-assemble into crystalline structures through hydrogen bonding of β-sheets[35, 36]. To reduce the crystallinity, silk-elastin like polypeptide (SELP) hybrids have been synthesized by combining the silk domain (GAGAGS) with an elastin domain (VPGVG). These

materials were created at the genetic level and a range of behaviors can be observed depending on the ratio of the elastin to silk motifs. Cappello and coworkers reported the formation of SELP irreversible hydrogels at physiological conditions and confirmed their applicability as drug depots as they are able to trap and slowly release various molecules[37]. Ghandehari and coworkers created SELP compositions with a ratio of 1:8 of GAGAGS to VPGVG (a composition with less silk motifs than used by Cappello and coworkers) that were observed to be thermally responsive in a similar manner to ELPs[36]. In addition, they introduced pH sensitivity to SELPs by incorporating VPGEG repeats into the SELP sequence which lead to changes in the transition temperature upon changing the pH in a range around the pKa of glutamic acid. Ghandehari and coworkers also demonstrated the feasibility of SELP hydrogels with VPGKG motifs as DNA delivery depots for gene therapy[38]. Plasmid DNA was encapsulated in SELP hydrogels. The hydrogel was injected adjacent to a tumor and the reporter gene expression was quantified. The expression level indicated a sustained release of the plasmid for three days and improved uptake compared to injection of naked DNA.

Resilin-like polypeptides, the most recent to be studied, are promising materials due to their superior elastic properties and thus have great potential as bioactive scaffolds and biomaterials[34, 39]. The resilin-like polypeptides repeating units are generally more hydrophilic than those of elastin-like polypeptides. While resilin and silk-like polypeptides are somewhat limited in scope in current studies, elastin-like polypeptides

are perhaps the most interesting of this category of materials as they have been extensively engineered for numerous biomedical applications.

For drug delivery and tissue engineering applications, ELPs have been designed to form depots, hydrogels and nanoparticles [7, 8, 40-44]. These ELP systems have been functionalized by adding biological moieties through fusion to targeting peptides or therapeutic proteins[10, 41], or introducing additional stimulus responsiveness through altering guest residue compositions or interspersing peptides along the ELP chain[13, 45].To impart biological functionality, ELPs have been fused to cell penetrating peptides such as TAT and therapeutic peptides to improve uptake and delivery to tumor cells[10, 11]. ELPs have also been functionalized by fusing oligo-lysine peptides to ELPs to condense DNA for gene delivery[46]. In addition, fusion to ELPs can be utilized to enhance therapeutic protein delivery and retention by formation of depots upon subcutaneous injection due to its thermal behavior[40, 41]. For example, interleukin-1 receptor antagonist (IL-1Ra) was fused to ELPs to improve retention in joints for treatment of rheumatoid arthritis. Introducing additional stimuli responsiveness allows ELP systems to sense changes in their environment and respond for example by releasing loaded drug in response to these changes. ELPs that respond to stimuli such as pH, light or specific ions were accomplished respectively by creating ELPs with the guest residue histadine which has a pK_a of 6.4[45], chemically conjugating a light-sensitive group to a glutamic acid guest residue[47], or embedding calcium binding peptides along the backbone of the ELP[13].

While additional functionality is an important aspect in designing ELP systems, the underlying ELP architecture that generates the desired structures such as nanoparticles is an important design parameter as well. For the rest of this section, we focus on exploring the design of ELP architectures, in particular, creating block copolymers which self-assemble into nanoscaled structures. Conticello and coworkers synthesized the first amphiphlic diblock (AB) of ELPs with pentapeptides [(V/I)PGXG][48]. The hydrophilic block is composed of the pentapeptides [VPG**E**G-(IPG**A**G)$_4$]$_{14}$ and the hydrophobic block is composed of the pentapeptides [VPG**F**G-(IPG**V**G)$_4$]$_{16}$. The guest residues glutamic acid and alanine are more hydrophilic than the guest residues phenylalanine and valine creating a difference in transition temperature of the two blocks. The selective dehydration of the hydrophobic block was observed by differential scanning calorimetry at a temperature of 11.5 °C. The formation of nanoparticles was confirmed by dynamic light scattering. Nanoparticles of average radius 23.5 nm are detected at 25 °C, a temperature at which the hydrophobic block is desolvated, while unimers of average radius 7 nm are detected at 5°C, a temperature at which both blocks are soluble. This study illustrated the capability of creating amphiphilic ELPs that desolvate independently and form nanoparticles by altering the guest residue compositions.

Chaikof and coworkers showed that a triblock architecture BAB can also self-assemble into nanoparticles[44]. The triblock was composed of two hydrophobic blocks (B)

that flank a hydrophilic block (A). The hydrophobic block is composed of the pentapeptides [VPG**A**G-(IPG**A**G)$_4$]$_{16}$ while the hydrophilic block is composed of the pentapeptides [(VPG**V**G)$_2$-VPG**E**G-(VPG**V**G)$_2$]$_{48}$. The hydrophobic block was designed to transition around 20 °C while the hydrophilic block was designed to transition around 37 °C. The triblocks were found to self-assemble into spherical nanoparticles with a radius of approximately 122 nm at temperatures below the transition of both A and B blocks. Upon heating, the nanoparticles decrease in size to a radius of 95 nm and the light scattering intensity increased indicating that the hydrophobic block became less hydrated and a denser structure is formed. An increase of β-sheet structure in the core was hypothesized to induce tighter packing in the core.

In additional work, Chaikof and coworkers hypothesized that additional stabilization of ELP micelles can be attained by inserting 4 cysteine residues between the hydrophobic and hydrophilic block[49]. The hydrophilic block was composed of the pentapeptides VPGEG and VPGVG at a ratio of 1:4 respectively and a total length of 50 pentapeptides. The hydrophobic was composed of the pentapeptides IPGVG and VPGYG at a ratio of 1:4 respectively and a total length of 60 or 75 pentapeptides. The ELP diblock assembled above the transition temperature of the hydrophobic block (10 °C) into spherical nanoparticles that are 25 nm in radius. The stability of the micelles was studied after the cysteines at the interface of the core and corona were allowed to crosslink by incubation at 25 °C overnight. The micelles became stable at a range of

temperatures between 5 °C and 37°C and were susceptible to disruption only upon addition of a reducing agent. This example of ELP diblocks illustrates the wide range of engineering allowed by the precise genetic control over ELP architecture.

Rodriguez and coworkers explored the role of block length and block architecture on the morphology of self-assembled structures[50]. They created three block copolymers; two diblocks (AB) and one triblock of architecture ABA, where B is the hydrophobic block and A is the hydrophilic block. The same hydrophobic block was used in all three constructs and is composed of 40 repeats of VPGAG (A_{40}). The hydrophilic block was composed of either 10 or 20 repeats of [$(VPGVG)_2$-(VPGEG)-$(VPGVG)_2$] (E_{50} and E_{100}). The two diblocks were $E_{50}A_{40}$ and $E_{100}A_{40}$ and the triblock was $E_{50}A_{40}E_{50}$. Above their respective hydrophobic transition temperature, $E_{50}A_{40}$ was found to self-assemble into spherical micelles with radius of 74 nm while $E_{100}A_{40}$ and $E_{50}A_{40}E_{50}$ formed vesicles of approximately 100 nm. The size of the spherical micelles of $E_{50}A_{40}$ is larger than that expected for a diblock of this length. In addition, although surprising, the increase in the hydrophilic block length of the diblock lead to formation of vesicles. The triblock also formed vesicles of similar size but with half the aggregation number of $E_{100}A_{40}$ vesicles indicating that the architecture influenced the physical properties of vesicle.

ELP nanostructures were also obtained by fusing an ELP block to other self-assembling peptide motifs or hydrophilic polypeptides. Holland and coworkers fused

an ELP with composition $(VPGVG)_{40}$ at the genetic level to a peptide sequence known as a foldon[51, 52]. Foldons are composed of 27 amino acids, are negatively charged and form trimers. Fusion to the foldon domain decreased the transition temperature compared to that of an ELP with a similar length (40 pentapeptides) but with no foldon domain. Yet, the transition temperature of the ELP foldon fusion was still higher than that of a linear ELP that is composed of 120 pentapeptides which indicated that the architecture of the ELP plays a role in determining its transition behavior. While the ELP foldon fusion shows a sharp transition upon increasing temperature in phosphate buffered saline (PBS), decreasing the salt concentration below the 140 mM of NaCl in PBS altered the behavior of the ELP foldon fusion. At salt concentrations below 15 mM, spherical micelles of a diameter of approximately 30 nm formed. At salt concentrations between 15 and 45 mM, non-spherical micelles of a diameter of approximately 60 nm formed. The change in morphology and self-assembly behavior is predicted to be a result of the change in screening of electrostatics of the negatively charged foldon at these salt concentrations.

Kobatake and coworkers created a set of hybrid diblocks composed of the ELP pentapeptide $[(VPGVG)_{10}KI]_n$ where n is 2, 4, 12 or 16 and a polyaspartic acid $(D_{11}L)_m$ where m is 2, 4, 8, or 16[53]. The diblocks were fully genetically encoded. All diblocks with ELP lengths above 40 pentapeptides were found to self-assemble into small nanoparticles with a diameter between 25 to 65 nm upon the collapse of the ELP block.

One exception was the diblock with ELP block length of 160 pentapeptides and polyaspartic block length of 22 aspartic acids; this diblock formed nanoparticles of diameter 265 nm, which is most likely due to the ratio of the small hydrophilic block to the larger hydrophobic block. For a given ELP block length, increasing the polyaspartic block length increased the transition temperature of the diblock as expected due to the increased charge of the nanoparticles.

Sugawara-Narutaki and coworkers created a double hydrophobic block copolymer composed of ELP segments [VPGXG] and glycine rich segments [VGGXG][54]. Glycine-rich segments order upon increase in temperature and have the tendency to form β-sheets and order into amyloid-like fibrils. A triblock was synthesized which was composed of two glycine-rich segments flanking a hydrophobic ELP segment, $[VGGVG]_5$-$[(VPGVG)_2(VPGFG)(VPGVG)_2]_5$-$[VGGVG]_5$. The self-assembly was studied by atomic force microscopy and the triblock was found to form beaded nanofibers that are 20-70 nm in diameter. The fibers formed over the course of 7 days and are expected to be the result of the organization of the glycine-rich segments into β-sheets that form the link between the beads while the collapsed ELP domain is in the middle of the bead.

We have previously synthesized ELP diblocks (ELP_{BC}) that were observed to self-assemble into spherical micelles (Figure 3)[8]. The hydrophilic block is composed of the guest residues valine, alanine and glycine at a ratio 1:8:7 respectively while the hydrophobic block is composed of the guest residue valine. As alanine and glycine are

more hydrophilic than valine, fusing these two blocks with high and low transition temperatures creates an amphiphilic diblock. The hydrophobic block desolvates independently from the hydrophilic block. At temperatures below the transition of both blocks, the ELP_{BC} is a soluble unimer with a hydrodynamic radius of ~ 6 nm. Upon increasing the temperature above the transition temperature of the hydrophobic block, the hydrophobic block collapses and forms the core of a micelle while the hydrated hydrophilic block forms the corona. The temperature at which this transition occurs is known as the critical micelle temperature (CMT). The hydrodynamic radius of the micelles was measured to be between 30 to 40 nm. As the temperature is further increased, the hydrophilic block also collapses and aggregates forms resulting in a two-phase solution. The temperature at which these aggregates form is referred to as the micelle-to-aggregate transition temperature.

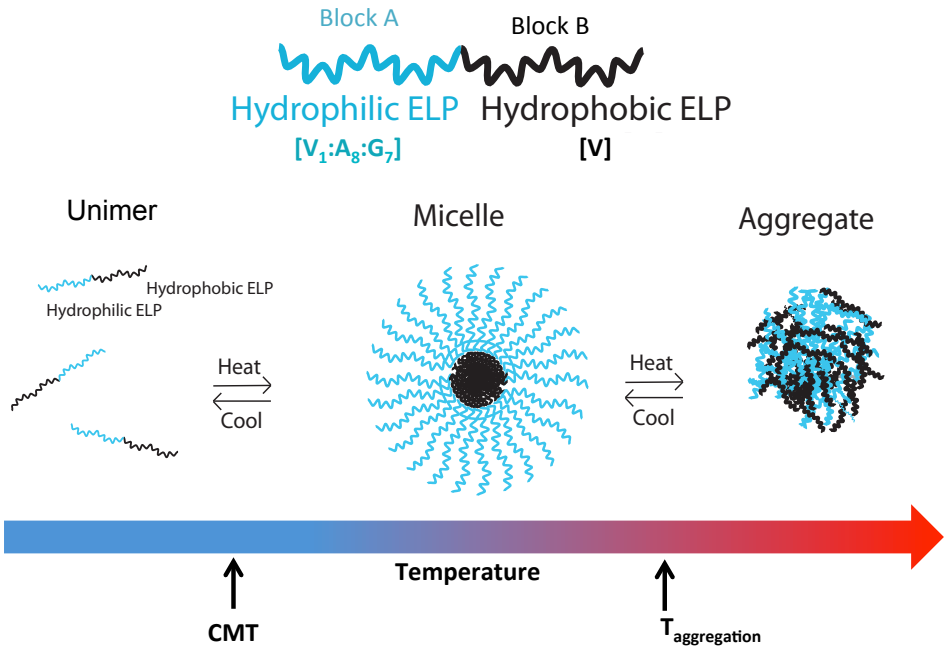

Figure 3: Self-assembly of ELP diblocks as temperature is increased. A transition between unimer to micelle occurs upon the collapse of the hydrophobic block. A transition between micelles and micron-sized aggregates occurs upon the collapse of the hydrophilic block.

Different block lengths of the hydrophobic and hydrophilic ELPs were fused to create a set of six ELP$_{BC}$. The ratio of the two block lengths was maintained between 1:2 to 2:1. The CMT was found to be 5 °C greater than the transition temperature of the hydrophobic ELP monoblock. The length of the hydrophilic block did not affect the CMT for a given hydrophobic block length. The micelle-to-aggregate transition temperature did not vary significantly for all hydrophilic and hydrophobic block lengths and ratios. In addition, while the CMT retained dependence on concentration, the micelle-to-aggregate transition temperature did not depend on changes in concentration.

The spherical morphology of the nanoparticles was confirmed through dynamic and static light scattering as well as cryo-TEM imaging.

These ELP_{BC} were functionalized with an RGD peptide to target the vasculature of tumors, as this motif is known to bind the $\alpha_v\beta_3$ integrin over expressed on the surface of endothelial cells[55]. The micelle's self-assembly behavior was unaffected by the presence of the short peptide. Cell uptake of the RDG decorated ELP_{BC} nanoparticles increased in comparison to the unimer state and the negative control of undecorated ELP_{BC} nanoparticles as measured by flow cytometry. This study demonstrated the capability of ELP_{BC} micelles for multivalently displaying targeting moieties on their surface.

1.3 Multivalent display of protein targeting moieties on nanoparticles

Cancer therapies have recently focused on the use of nanoparticles as carriers to deliver therapeutics and imaging agents to tumor sites[56-59]. These therapies are designed to target tumors by taking advantage of the enhanced permeability and retention (EPR) effect[58]. The EPR effect is characterized by 'leaky' tumor vasculature, which allows particles 10-100 nm in size to permeate into the tumor site, and by poor lymphatic clearance, which allows the particles to accumulate there[56]. In addition, this range of particle size is above the renal clearance threshold ensuring longer half-lives for the therapeutic carriers. Many polymeric systems that form nanoparticles (more specifically micelles) within this size range have been developed in which a hydrophobic core

encapsulates or is covalently linked to a hydrophobic drug while the corona is a comparatively hydrophilic block such as polyethylene glycol[59].

While the EPR effect allows for passive targeting, recent efforts to increase uptake by tumor cells have also relied on decorating nanoparticles with targeting moieties that bind over-expressed receptors on tumor cells[60]. The binding of receptors allows the nanoparticles to utilize receptor-mediated uptake pathways (clathrin-mediated and clathrin-independent endocytosis) as well as macropinocytosis[61-64]. Uptake through different mechanisms can lead to different trafficking pathways inside the cell and therefore different fates of the therapeutic drug. Furthermore, the presentation of targeting moieties on a nanoparticle (multivalent display) results in an increased apparent affinity, thereby increasing the chance that the nanoparticle will bind to the cell surface. The increase in affinity attributed to several binding events occurring per nanoparticle can be described quantitatively as follows[65]:

$$K_{nanoparticle} = (K_{unimer})^{\alpha N}$$

where $K_{nanoparticle}$ is the binding affinity of the nanoparticle, K_{unimer} is the binding affinity of the unimers, α is the degree of cooperativity and N is the number of unimers. Multivalent interactions are common in nature in events such as bacteria binding to macrophages or virus adhesion to a cell surface[65]. This phenomenon is particularly advantageous for targeting ligands with low affinity in the unimeric state such a RGD[66]. The increase in affinity is attributed to a lower k_{off} rate rather than an enhanced k_{on} rate[65,

[67]. Nanoparticles are decorated with targeting moieties such as carbohydrates and small organic molecules (folate, lactose, galactose)[68-70], aptamers[57], and proteins (mostly antibodies or fragments of them, antibody mimics, and transferrin)[71, 72]. These targeting moieties are conjugated to the polymeric micelles after each is synthesized separately[60] or in some examples the polymeric chain is grown from the surface of the targeting protein[73]. Protein targeting moieties are of particular interest as they can be engineered to bind a wide variety of targets. A few notable examples of protein-decorated nanoparticles are discussed below.

DeSimone and coworkers created poly(ethylene glycol)-based cylindrical nanoparticles (~300 nm) to which they conjugated transferrin, a targeting protein that binds and transports iron to tissues and is overexpressed in tumor cells[74]. The multivalent display of this protein was found to increase uptake in tumor cells. A systematic reduction of the number of transferrin molecules resulted in a decrease in cell uptake. The cell uptake was also dependent on the level of transferrin receptor expression in that cell line.

Merkx and coworkers explored the multivalent display of a collagen binding domain (CNA35) when conjugated to a pegylated phospholipid known to self-assemble into micelles[67]. CNA35 was mutated to obtain a dissociation constant in the mM range and the effect of the number of proteins on the surface of the micelle was examined in terms of binding affinity to its target, collagen. From surface plasmon resonance studies,

increased affinity was observed as the number of proteins displayed increased. CNA35 micelles were observed to have lower dissociation rates than CNA35 proteins as expected for multivalent interactions.

A similar pegylated phospholipid also known to self-assemble into micelles was used by Torchilin and coworkers to display monoclonal antibodies[75]. The micelles were loaded with a poorly soluble anticancer drug, taxol. The micelles decorated with the monoclonal antibodies showed better binding to tumor cells, and better accumulation and tumor growth inhibition than a control micelle with no targeting moiety. As opposed to entire antibodies, other studies have used anti-HER2 monoclonal antibody fragments (Fab' and scF_v) to decorate similar immunolipsome nanoparticles to target breast cancer and improve uptake[76]. Smaller targeting moieties (fragments of antibodies) might be more advantageous than entire antibodies as they could spatially allow for more binding events per micelle to occur[77].

While the examples above conjugated the protein to the nanocarrier through a covalent bond, Nolte and coworkers have attached proteins to synthetic diblocks composed of polystyrene-*b*-poly(ethylene glycol) by conjugating a protoporphyrin, a heme cofactor, to the polystyrene end[78]. Two proteins, myoglobin and horse radish peroxidase, were allowed to associate with the cofactor thus creating a triblock where the protein is linked to the hydrophobic block end. These diblocks are known to self-assemble into spherical micelles (for polystyrene block length of 48 monomers) but some

rod micelles are observed at a larger polystyrene block length (for polystyrene block length of 144 monomers). The attachment of the proteins changed the self-assembly behavior of the diblocks. For horse radish peroxidase, polydisperse vesicles were observed for the shorter polystyrene length but multiple morphologies including spherical, rod and Y-shaped micelles were also observed for the longer polystyrene block. For myoglobin, the triblock with the shorter polystyrene length formed spherical aggregates with lamellae-like structures while the triblock with the longer polystyrene length formed micellar structure as well as more unique shapes such as toroids.

The conjugation of the protein targeting moieties described here to their nanocarrier requires specific chemistry and is limited by the conjugation efficiency and the available functional groups. ELP$_{BC}$s offer an elegant solution to these shortcomings of chemically synthesized carriers as proteins can be seamlessly fused to ELP$_{BC}$s at the genetic level. Therefore, we explore a ubiquitous platform for all peptide-based targeting moieties that does not require any post-synthesis conjugation: a self-assembling elastin-like polypeptide block copolymer.

1.4 Effect of proteins on elastin-like polypeptide transition temperature

ELPs are an ideal purification tag for proteins because they are genetically encoded and display phase separation behavior. ELPs have been extensively studied as purification tags as an alternative cost-effective method that eliminates the need for chromatography[79-82]. Proteins are fused to ELPs at the genetic level and are expressed as

one chain. The protein ELP fusions retain LCST behavior, which is utilized to separate the target protein from contaminants by triggering the phase separation. While demonstrating the utility of ELPs as purification tags for a range of proteins, a perhaps more interesting phenomenon was observed; the transition temperature of the protein ELP fusion is different from that of the free ELP[83]. The protein exerts an effect on the transition temperature of the ELP and the shift in transition temperature is termed the "ΔT_t effect". The effect on the transition temperature is hypothesized to be related to the surface properties of the protein. Hydrophilic proteins increase the transition temperature with respect to the free ELP transition temperature while hydrophobic proteins decrease it. This protein effect is analogous to the effect of guest residue composition in which more hydrophobic guest residues will decrease the transition temperature.

A quantitative model was developed to relate the surface properties of proteins to the ΔT_t effect[84]. Six proteins were fused to an ELP composed of valine, glycine and alanine as guest residues at a ratio of 5:2:3 and is 90 pentapeptides long. The transition temperatures of the protein ELP fusions were determined and the shift in transition temperature with respect to that of the free ELP was calculated (ΔT_t). The surface properties of the protein were quantified from their crystal structures by computationally determining the fraction of the solvent accessible surface area of each residue and weighing it with a characteristic transition temperature for that residue as

determined by Urry and coworkers[2, 16]. The characteristic transition temperature of a residue is the transition temperature of an ELP composed entirely of that residue as the guest residue (measurements were performed for samples of a concentration of 40 g/L). As the transition temperature is related to the hydrophobicity/hydrophilicity of the guest residue, this characteristic transition temperature serves as a hydrophobicity scale for the 20 amino acids. The sum of the weighted solvent accessible area for all 20 amino acids is termed as the hydrophobicity index (HI) where large HI values indicate a hydrophilic protein.

A linear relationship was found between ΔT_t and HI in which an increase in HI leads to an increase in ΔT_t. The major contribution to this relationship was found to be from charged residues present at the protein surface as they have high characteristic transition temperatures. This finding supports the hypothesis that the surface properties of the protein affect the transition temperature of the ELP. The proteins studied ranged between 8 and 27 kDa in molecular weight. The molecular weight was not found to be a factor affecting the relationship between ΔT_t and HI.

This model, while useful, has its limitations in predicting the effect of proteins on ELPs: 1) the hydrophobicity scale used in the model was determined at one concentration using ELPs that were polydisperse as they are generated through chemical synthesis, and 2) one ELP composition and length was fused to the proteins. However, the model does provide a semi-quantitative approach to understanding the relationship

between proteins and ELPs. In addition, an important conclusion pertaining to the studies presented here is that the protein effect on ELP behavior is significant and the interaction between them contributes to the overall observed behavior.

1.5 Overview of motivation

1.5.1 Multivalent display of proteins through elastin-like polypeptide diblock self-assembly

ELP_{BC} that assemble into nanoparticles have been shown to be promising drug delivery vehicles for cancer therapies[8, 45, 55]. To improve uptake by tumor cells, ELP_{BC}s have been modified with targeting moieties that are short peptides (< 10 amino acids). However, to access a broader range of affinities and tumor targets, it is of interest to display folded proteins that are ~ 100-200 amino acids. ELP_{BC}s as a platform for multivalent display of proteins are advantageous in that proteins can be simply fused at the genetic level. The genetically encoded protein ELP_{BC} fusion once expressed yields a covalently linked product with precise molecular weight and high monodispersity. The protein ELP_{BC} fusion requires no post-modification and as opposed to chemically synthesized polymers does not suffer from yield limits of chemical conjugation efficiency. In addition, as the protein is linked covalently at the C-terminus to the ELP_{BC}, no amino acids on the surface of the protein are used for chemical conjugation to the polymer avoiding multiple conjugation sites or conjugation to amino acids essential to the function of the protein.

While the self-assembly of ELP$_{BC}$ tolerates the short peptides at the hydrophilic end, proteins of larger molecular weights (100-200 amino acids) are predicted to exert a greater effect on the self-assembly as evidenced by the change in transition temperature observed for protein fusions to ELP monoblocks[84]. We hypothesize that molecular weight and the surface properties of the proteins will affect the self-assembly behavior of ELP$_{BC}$s. Proteins with larger molecular weights and more hydrophobic surfaces are more likely to disrupt self-assembly of ELP$_{BC}$s. Proteins that do not disrupt the self-assembly are still expected to modify the transition temperatures of the ELP blocks. In addition, as previous studies showed that ELP$_{BC}$ block length and compositions affected self-assembly behavior, a logical extension is that these factors also will affect the behavior of protein ELP$_{BC}$ fusions.

The proteins will be fused to the ELP$_{BC}$ at the hydrophilic block end orienting the protein towards the surface of the micelle. We expect the self-assembly behavior of the protein ELP$_{BC}$ fusions to follow one of the two schematics illustrated in Figure 4. Proteins ELP$_{BC}$ that do self-assemble are expected to behave similarly to ELP$_{BC}$ and transition from unimers to micelles to aggregate as the temperature is increased. While the proteins that do disrupt the self-assembly of ELP$_{BC}$ are expected to force the protein ELP$_{BC}$ to transition from unimers to aggregates as the temperature is increased. The results of examining this premise are presented in chapter 2 and 3.

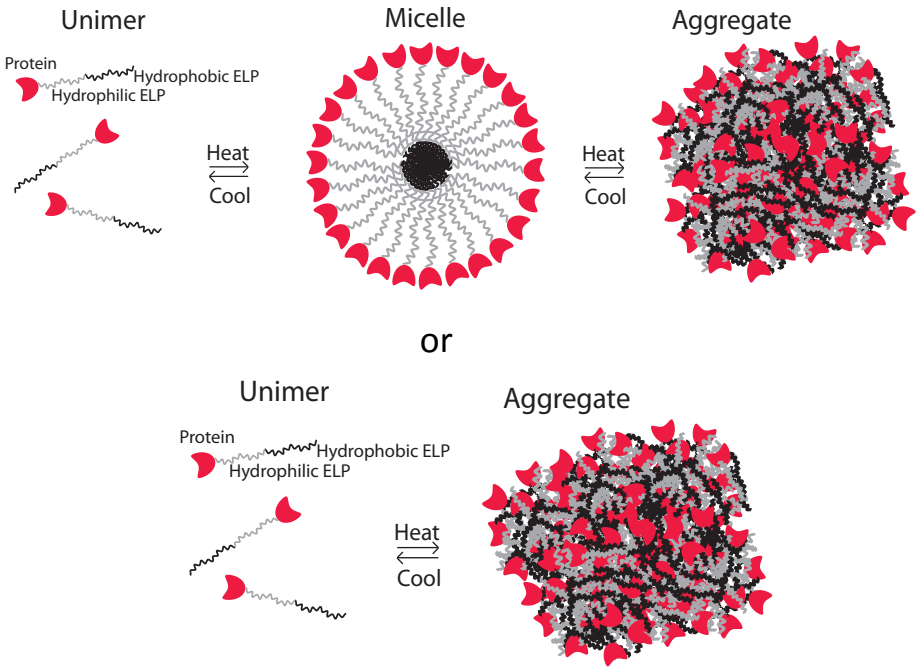

Figure 4: Schematic of predicted protein ELP$_{BC}$ fusion behavior. The top panel shows the expected protein ELP$_{BC}$ self-assembly if the protein does not disrupt self-assembly of ELP$_{BC}$; the protein ELP$_{BC}$ fusion transitions from unimer to micelle to aggregate as temperature is increased. The bottom panel shows the expected protein ELP$_{BC}$ self-assembly if the protein does disrupt self-assembly of ELP$_{BC}$; the protein ELP$_{BC}$ fusion transition from unimer to aggregate as the temperature is increased.

1.5.2 Theoretically understanding the self-assembly of elastin-like polypeptide diblocks

Theory describing the self-assembly of synthetic polymeric systems into micelles has been discussed and reported[85-87]. The theory is based on three free energies that control self-assembly of diblocks: corona elastic and interaction energy, surface free energy and core elastic energy. However, the applicability of this theory to polypeptide systems has yet to be determined. While the balance of the three free energy contributions are still expected to determine the properties of the self-assembled ELP

diblocks, additional contributions could arise due to the nature of polypeptides. ELPs are known to undergo an increase in secondary structure as the temperature is increased; specifically, an increase in type II β-turns is observed. The formation of secondary structures could contribute to the forces controlling self-assembly by incurring an entropic or enthalpic cost, or by increasing chain stiffness.

In this thesis, we describe the application of this theory to ELP diblocks. The motivation to understand the theory behind the self-assembly of ELPs is to enable the intelligent design of ELP_{BC} with the desired properties such as CMT and micelle-to-aggregate transition temperature. In addition, as synthetic polymers have been shown to self-assemble into different morphologies (spherical, cylindrical and lamellar) depending on the length of the hydrophilic and hydrophobic block lengths, we would like to predict the regimes of block lengths in which ELP_{BC}s will assemble into these morphologies. If the regimes are known then ELP_{BC} can be synthesized with block lengths within that regime to hopefully attain these morphologies.

The validity of the theoretical model is determined by comparing the predicted physical properties of the micelles with the corresponding experimental values. The physical properties are the micelle's radius and aggregation number. To fit the model, two parameters must be experimentally determined first. First, we must determine the quality of solvent of the coronal block, which can be inferred from the monomer-monomer interaction. The interaction is measured by constructing a Zimm plot through

static light scattering. Second, we measure the surface tension of the hydrophobic block, which can be determined from the relationship of concentration and the transition temperature at different pentapeptide lengths. The fitting of the model and comparison of the theoretical and experimental data is presented in chapter 4.

2. Multivalent protein presentation through Elastin-like polypeptide diblock self-assembly

2.1 Introduction

To create ELP nanoparticles with protein targeting moieties, a protein can be seamlessly fused to an ELP_{BC} at the N-terminus of the hydrophilic block so that it is oriented toward the outer surface of the corona. However, as adding a folded protein is analogous to adding a third block -albeit a block with complex surface properties and geometry- creating a triblock, it is important to study its effect on the self-assembly behavior. In considering the protein ELP_{BC} fusion systematically, the protein or the ELP_{BC} properties can be varied. In this chapter, the effect of proteins on the self-assembly of a set of ELP_{BC} that are previously known to form micelle is discussed.

2.1.1 Choice of protein and their properties

Proteins vary in their surface properties tremendously from the composition and distribution of exposed surface residues to the geometry of the protein. Four proteins were chosen for fusion with the ELP_{BC} based on their molecular weight and hydrophobicity: Thioredoxin (Trx), Blue Fluorescent Protein (BFP), humanized nanobody against lysozyme (VHH), fibronectin type III domain against $\alpha_v\beta_3$ integrin (Fn3). Table 1 summarizes the properties of these proteins. The proteins were chosen to naturally form unimers as formations of oligomers could affect self-assembly behavior. Furthermore, only proteins with structures in the Protein Data Bank were considered, as knowledge of their structure is essential in determining their surface properties. The

hydrophobicity of the four proteins is estimated based on the method developed by Trabbic-Carlson et al. and detailed in the methods section (2.2.1)[83]. The method calculates a hydrophobicity index (HI) based on the effect of each surface amino acid on the T_t. The more hydrophilic the protein is, the higher the HI value. Trx, VHH and Fn3 are proteins with similar molecular weights (~10 kDa) but varying hydrophobicities where Trx is the most hydrophilic and Fn3 and VHH are equally hydrophobic. BFP and Trx are of the same hydrophilicity but BFP is approximately twice the molecular weight. While Trx and BFP were chosen for being soluble stable proteins, Fn3 and VHH are clinically relevant proteins[88-93]. Both proteins are β-sheet scaffolds that can be engineered at their binding loops to have affinity to an array of targets[89, 93]. These versatile scaffolds have gained interest recently as potential replacements for antibodies in cancer treatments because of their low molecular weight, which intrinsically results in better tumor penetration, as well as their stability in comparison to antibody fragments[91].

Table 1: Protein Properties

Protein	Molecular weight (kDa)	Hydrophobicity Index (HI)	PDB
Thioredoxin (Trx)	12	84	1xob
Nanobody (VHH)	10	57	3eba
Fn3 $\alpha_v\beta_3$	11	55	1ttg
BFP	27	84	1BFP

2.1.2 Choice of Elastin-like polypeptide diblocks

A set of six ELP_{BC} with differing block lengths and length ratios known to self-assemble into micelles were used in this study[8]. For this set of ELP_{BC}, the hydrophilic

block guest residue composition is valine, alanine, and glycine at a ratio of 1:8:7 (ELP[V_1:A_8:G_7]) while the hydrophobic block guest residue composition is valine (ELP[V]). As alanine and glycine are more hydrophilic than valine, the hydrophilic block composition results in a higher T_t for that block compared to the purely valine hydrophobic block which has a much lower T_t. Each ELP block has been previously synthesized at a genetic level[3] and then the two blocks were combined at the genetic level to create ELP_{BC}s with block length ratios from 1:2 to 2:1 as detailed in Table 2. ELP_{BC} with block length ratios outside this range were found to not assemble into micelles. The ELP_{BC} block lengths are indicated by the number of pentapeptides of the hydrophilic block followed by that of the hydrophobic block. For example, ELP 96,90 is an ELP_{BC} with a hydrophilic ELP block of composition [V_1:A_8:G_7] and 96 pentapeptides and a hydrophobic ELP block of composition [V] and 90 pentapeptides.

Table 2: lengths hydrophilic and hydrophobic ELP_{BC} set in pentapeptides

ELP_{BC}	Hydrophilic	Hydrophobic
ELP 64,60	64	60
ELP 64,90	64	90
ELP 64,120	64	120
ELP 96,60	96	60
ELP 96,90	96	90
ELP 128,60	128	60

The thermal behavior of the ELP_{BC}s was investigated by measuring the change in absorbance with increasing temperature as well as light scattering. The ELP_{BC} were found to exhibit three state behavior: unimer, micelle, and aggregate (phase separated

solution). As temperature is increased, the hydrophobic block collapses as the solvent quality becomes poor. To decrease surface tension, the unimers form the core of the micelle while the hydrophilic block remains hydrated and forms the corona of the micelle at a temperature known as the critical micelle temperature (CMT). Upon further increasing the temperature, the hydrophilic block also collapses as the solvent quality becomes poor for it as well and the ELP_{BC} forms a two-phase solution. When the absorbance was monitored as temperature was increased, a small increase in optical density at 350 nm (O.D.350) of about ~ 0.1-0.5 was observed as the unimers formed micelles and upon additional heating, the hydrophilic block collapse was observed as a sharp large increase in O.D.350 of ~2 for a typical 25μM solution. The thermal behavior was confirmed with DLS and the change in hydrodynamic radius (R_h) matched the change in O.D.350. The unimer of radius ~7 nm transitioned to a micelle of a radius of ~35 nm.

The two transition temperatures were examined at a range of concentrations. The CMT decreased when the concentration was increased and had a logarithmic dependence on concentration similar to that of the hydrophobic ELP monoblock. The micelle-to-aggregate transition decrease when the concentration was increased is insignificant and is also independent of the length of either block. The desensitization to the change in concentrations can be explained by the increased local concentration of the hydrophilic block in the corona.

2.2 Methods

2.2.1 Hydrophobicity calculation

To estimate the hydrophobicity of the protein, we must determined the amino acid composition of the protein accessible surface area ($ASA_{protein}$) to water. First, explicit hydrogens were added to the NMR or X-ray crystallography structures and Asn, Gln and His side chains were optimized using the program Molprobity and REDUCE (http://molprobity.biochem.duke.edu/)[94, 95]. These three residues have symmetric electron densities and thus can be positioned at less favorable orientation easily. REDUCE flips the residues by 180° and determines the optimum orientation for sterics and hydrogen bonding. Then, using the software Probe developed by the Richardson group at Duke University, a sphere with a radius of 1.4 Å to approximate a water molecule was rolled on the van-der-Waal surface of the protein. The contacts made with each type of amino acid on the surface were recorded as dots. The contact dots for each amino acid divided by the total number of contact dots gives the fraction of protein accessible surface area of that amino acid (ASA_{aa}). Next, a scale of hydrophobicity must be chosen to determine the effect of the surface amino acids on the transition temperature. Although multiple hydrophobicity scales for amino acids have been developed, the scale developed by Urry and coworkers is the most applicable to the protein ELP fusions[2, 16]. Urry and coworkers created libraries of ELPs for each amino acid; each library is composed of two guest residues, Valine and one of the remaining 19 amino acids. The ratio of the two

guest residues is increased within the same library so that the fraction of valine decreases and the other amino acid increases. After measuring the transition temperatures of the libraries at a fixed concentration of 40 mg/mL, the transition temperature of an ELP with 100% guest residue composition termed the characteristic T_t (T_{tc}) can be extrapolated from the plot of transition temperature versus guest residue fraction. As more hydrophobic guest residues will have a low T_{tc} while hydrophilic guest residues will have a high T_{tc}, this T_{tc} scale for amino acids can be used to quantify the effect of the presence of a specific amino acid at the protein surface on the T_t of the ELP. To quantify this effect, a hydrophobicity index (HI) was defined and calculated as follows: the total amount of contact dots for each amino acid was divided by the total amount of contact dots and then multiplied by the T_{tc} for the corresponding amino acid and the product was summed for all 20 amino acids.

$$HI = \sum_{aa} \mathrm{T_{tc}} \times \frac{ASA_{aa}}{ASA_{protien}}$$

2.2.2 ELP synthesis

The protein genes were inserted at the N-terminus of the ELP_{BC} gene resulting in a fusion of the order: protein-$ELP_{hydrophilic}$-$ELP_{hydrophobic}$. A set of six ELP_{BC} genes previously constructed in pET-25b+ by our group provided the starting point for the synthesis of the protein ELP_{BC} fusions. These ELP_{BC}s have a guest residue composition of valine, glycine and alanine at a ratio of 1:7:8 for the hydrophilic block and valine for the hydrophobic block. The gene encoding *E. coli* Trx was obtained from the vector pET-32a

(Novagen), the BFP gene was available from a previous study, the VHH gene against lysozyme was synthesized by Mr. gene (Regensburg , Germany) and the Fn3 gene against $\alpha_v\beta_3$ was available from a previous study by Dr. Liu (UNC)[88]. The four genes were amplified using PCR with primers encoding for *Nde* I restriction enzyme site at each end. The amplified genes were digested using the *Nde* I restriction enzyme (NEB) and ligated (NEB T4 ligase) to each of the ELP_{BC} vectors that had also been digested with the same restriction enzyme and subsequently dephosphorylated using calf intestine phosphatase (CIP) (NEB). The resulting colonies were screened using colony PCR. The successfully sequenced clones were transformed into BL21(DE3) *E. coli* cells. The BL21(DE3) cells with the constructed plasmids were grown in 1 liter of terrific broth for 24 hours at 37 °C with continuous shaking at 200 rpm. The proteins were extracted and purified as described in Meyer et al[80]. The ELP_{BC} was used as a purification tag for the proteins ELP_{BC} fusion and inverse transition cycling (ITC) was used to separate the protein ELP_{BC} fusion from contaminants. Briefly, the 1 liter culture was centrifuged at 4 °C at 3000 rpm and the resulting pellet was resuspended in phosphate buffered saline (PBS) up to a volume of 45 mL and was transferred into a 50 mL conical tube. The cells were sonicated for 9 mins (10 secs on, 20 secs off) at 85 Watts to lyse them. The lysed cells were mixed with polyethyleneimine (PEI) (2 mL of 10 w/v% per liter of culture) to precipitate negatively charged molecules such as DNA. The mixture was centrifuged for 15 mins at 14000 rpm at 4°C. The supernatant was transferred to clean tubes and sodium

citrate was added to isothermally trigger the phase transition of the protein ELP_{BC} and form a protein ELP_{BC} rich sediment. The phase-separated solution was centrifuged for 10 mins at 13200 rpm at room temperature to form a dense pellet; this step is referred to as a hot spin. The supernatant was removed and the pellet was resuspended in PBS. The redissolved pellet was centrifuged for 10 mins at 13200 rpm at 4°C to remove insoluble contaminates; this step is referred to as a cold spin. The hot and cold spins were repeated until the protein ELP_{BC} is pure. The purity of the samples was verified by visualization using sodium dodecyl sulfate polyacrylamide gel electrophoresis (SDS-PAGE) to ensure that one band at the correct molecular weight is observed.

2.2.3 UV spectroscopy thermal characterization

The thermal characteristics of the protein ELP_{BC} fusions were investigated using a UV-Vis spectrophotometer (Cary 300 Bio; Varian Inc.). Upon dilution to the desired concentration, 900μL of the sample were added to a washed cuvette and the absorbance was set to zero for each cuvette separately so that only the increase in absorbance was observed and the difference in initial absorbance between samples was eliminated. The samples were heated at a rate of 1 °C/min as absorbance measurements at 350 nm were recorded at 0.3°C intervals. The samples were prepared in PBS at a desired concentration by determining the stock concentration and diluting into PBS. The stock concentration was determined by measuring the absorbance at 280 nm. The extinction coefficient was determined by summing the number of tryptophans, tyrosines and S-S

bonds and multiplying by their extinction coefficient of 5690 M^{-1} cm^{-1}, 1280 M^{-1} cm^{-1}, and 120 M^{-1} cm^{-1} respectively.

2.2.4 Dynamic and static light scattering

Hydrodynamic radii (R_h) were measured at different temperatures using a temperature controlled dynamic light scattering (DLS) instrument (DynaPro, Wyatt technologies, Santa Barbra, CA). A single detector at 90° measured intensity fluctuations as the temperature was increased in 1°C increments. Three acquisitions each 1 min were recorded at each temperature. The samples were prepared in PBS at 25 μM and 100μL were filtered through Anotop 10 Whatman 20 nm filters directly into a pre-washed cuvette. The autocorrelation curves were fit using a regularization fit. The measured R_h indicates the radius of a sphere with a diffusion coefficient equivalent to that of the nanoparticle formed by the protein ELP_{BC} fusions.

Additional information about the formed nanoparticles can be obtained by measuring the change in diffusion coefficient with scattering angle, as the slope is indicative of the topology and polydispersity of the nanoparticles. Furthermore, static light scattering (SLS) in which an average intensity is measured at a range of scattering angles provides information about the topology of the nanoparticle and its molecular weight from which the aggregation number (monomers/nanoparticle) can be calculated. A Zimm plot was created by measuring the normalized intensity of scattered light (expressed as Raleigh scattering ratio, R) at multiple scattering angles (expressed as the

scattering wavevector, q). By fitting the equation below with a linear fit, the radius of gyration (R_g), which is a measure of the distribution of mass around the center of mass, and the weight average molecular weight were calculated from the slope and y-intercept respectively[14].

$$\frac{Kc}{R} = \frac{1}{M_w} + \frac{1}{3M_w} q^2 R_g^2$$

$$K = \frac{4\pi^2 n^2}{\lambda^4 N_{Av}} \left(\frac{dn}{dc}\right)^2$$

where R is the Raleigh ratio, q is the scattering wave vector (related to angle), c is the concentration of the sample, K is the optical constant, n is the refractive index, N_{AV} is Avogadro's number, λ is the wavelength and dn/dc is the change in refractive index with concentration.

DLS/SLS measurements were performed using the ALV/CGS-3 goniometer system or the ALV/CGS-8F platform based goniometer system (ALV, Langen, Germany). Measurements on the ALV/CGS-8F system were performed at Johannes Gutenberg University in Mainz, Germany. Samples for the ALV/CGS-8F goniometer system were prepared by filtering solutions of the protein ELP_{BC} fusions through an Anotop 10 Whatman 20nm filter using a Luer lock syringe (10mL, Hamilton, Reno, NV) into a quartz glass 20mm-diameter cylindrical cuvette (custom designed SUPRASIL quartz, Hellma, Müllheim, Germany). Filtration was carried out in a laminar flow cabinet. The cuvettes were precleaned using a refluxing acetone fountain to remove dust for at least 20 min. ALV/CGS-8F is a multi-detector system with 8 detectors set 17° apart.

The SLS measurements were set up so that the first detector moved from 25° to 39.875° in 2.125° steps. The DLS measurements were set up so that the first detector moved from 30° to 39° in one step. DLS measurements were set to 5 acquisitions, 60 seconds each at each angle. SLS measurements were set to 10 acquisitions, 10 seconds each at each angle. Samples for the ALV/CGS-3 goniometer system were prepared by filtering solutions of the protein ELP_{BC} fusions through an Anotop 10 Whatman 20 nm filter into a 10 mm disposable borosilicate glass tube (Fischer). The tubes were precleaned by washing three times with ethanol filtered through a 0.2 μm cellulose acetate filter. Simultaneous SLS/DLS measurement were obtained for angles between 30°-150° at 5° increments set to 3 acquisitions, each 30 or 15 seconds at each angle.

2.2.5 Cell uptake of Fn3 ELP_{BC}

A cell uptake assay for Fn3 fused to ELP 96,90 was performed to confirm that the proteins once displayed in micelle form remained bioactive and showed enhanced binding compared to that of the unimeric form.

2.2.5.1 Fluorophore conjugation:

To detect cellular uptake of Fn3 micelles by tumor cells, Alexa Fluor® 488 sulfodichlorophenol ester dye (Invitrogen) was conjugated to Fn3 ELP 96,90 or the control of ligand-negative ELP 96,90 by reacting the dye to the lysine residues present in either construct. The ligand-negative ELP 96,90 has one lysine within the N-terminal leader sequence. A 250 μM solution of each sample was prepared. Within one ITC

round, the samples were resuspended in 0.1 M sodium bicarbonate buffer pH 8.3. 1 mg of Alexa Flour® 488 was dissolved in 100 μL of anhydrous dimethylsulfoxide (DMSO). The dissolved Alexa Flour® 488 was added to 1 mL of 250 μM of the sample while vortexing to ensure mixing. The mixture was set to rotate at room temperature for 1 hour. After the reaction was completed, a round of ITC was used to separate the ELP constructs from unreacted dye. The samples were further purified using PD-10 Sephadex™ G-25 M columns (GE healthcare). The degree of labeling was then calculated. First, the protein absorbance ($A_{protein}$) was corrected using the following equation:

$$A_{protein} = A_{280} - \frac{A_{280\ free\ dye}}{A_{488\ free\ dye}} \times A_{488}$$

where A_{280} and A_{488} are the measured absorbance at 280nm and 488 nm respectively. The ratio of the absorbances for the free dye is a value given by the manufacturer. Then, the degree of labeling (D.O.L) was calculated using the following equation:

$$D.O.L = \frac{A_{488} \times \varepsilon_{protein}}{A_{protein} \times \varepsilon_{dye}}$$

where $\varepsilon_{protein}$ and ε_{dye} are the extinction coefficient of the protein and the dye respectively.

Once the degree of labeling was calculated, the two samples (Fn3 ELP 96,90 and ELP 96,90) were mixed with the corresponding unlabeled constructs to obtain the same degree of labeling for both samples. The labeled constructs were characterized through temperature controlled absorbance measurements as well as DLS measurements to

ensure that they retained self-assembly behavior as described in previous sections (2.2.3 and 2.2.4).

2.2.5.2 Cell culture:

Two human leukemia tumor cell lines, wild type K562 (K562/WT) and K562 that overexpress the $\alpha_v\beta_3$ integrin (K562/$\alpha_v\beta_3$), were available from previous studies by Dr. Liu (UNC)[88]. The cell lines were cultured in RPMI 1640 media (Invitrogen) supplemented with 10% FBS and 1% penicillin/streptomycin. The K562/$\alpha_v\beta_3$ media also contained 500 μg/mL G418 (Invitrogen). The cell cultures were maintained at 37°C and 5% CO_2. Cell cultures were started from frozen stocks and were split every 48 hrs.

2.2.5.3 Cell uptake

A total of 500,000 K562/WT or K562/$\alpha_v\beta_3$ cells were plated in 6-well plates and allowed to incubate overnight. The cells were rinsed twice and resuspended in 500 μL of a 10 μM Fn3 ELP 96,90-Alexa488 or ELP 96,90-Alexa488 in HBSS. The cells were incubated at either room temperature (below CMT) or 38 °C (above CMT) in normal atmosphere for 1 hour. The cells were then rinsed twice in binding buffer. Cells for flow cytometry were fixed in 4% PFA for 20 min and stored at 4 °C.

2.2.5.4 Flow cytometry:

Cell samples were analyzed using a LSRII Flow cytometer (BD Biosciences, San Jose, CA). Viable cells were gated using the forward and side scatter plots of unstained control cells. 10,000 live cells were analyzed for each sample. Fold increase in median

fluorescence was calculated by dividing the median of the cell fluorescence intensity histogram above the CMT by that below the CMT for a given sample (Fn3 ELP 96,90 or ELP 96,90) and cell line (K562/WT or K562/$\alpha_v\beta_3$).

2.3 Results and discussion

2.3.1 Thermal properties of protein elastin-like polypeptide diblock fusions

First, the effect of the proteins on the thermal properties of the ELP_{BC} is examined. The thermal properties of the protein ELP_{BC} fusions were determined by monitoring their absorbance at 350 nm while heating the sample at a rate of 1°C/min. While a monoblock ELPs show a single sharp step increase in absorbance (O.D.350 of ~2 for a 25 μM solution) indicative of a unimer-to-aggregate transition, ELP_{BC}s that exhibit self-assembly behavior show a different pattern of change in absorbance with increasing temperature. First, an initial slight increase in absorbance (O.D.350 of ~0.1-0.5) is observed and upon further increase in temperature a much larger increase in absorbance (O.D.350 ~2) is observed. The initial slight increase in absorbance has been found to indicate nanoparticle formation as the ELP_{BC} transitions from unimer to micelle upon the collapse of the hydrophobic block. The temperature at which the unimer-to-micelle transition occurs is known as the critical micelle temperature (CMT). As the solution is heated to a higher temperature than the CMT, the ELP_{BC} transitions from a micelle to micron-sized aggregates upon the collapse of the hydrophilic block and a two-phase solution forms (globules and sediment) as both ELP blocks are now is poor solvent. The

proteins can effect this thermal behavior of the diblocks in multiple ways: 1) if the self-assembly is disrupted, the thermal behavior is expected to be more similar to a single block; 2) if the self-assembly behavior is maintained, the thermal behavior would be similar to that of the ELP$_{BC}$ but the CMT and the micelle-to-aggregate transition temperature may shift.

Four proteins were fused to six ELP$_{BC}$s known to self-assemble. Of the four protein ELP$_{BC}$ sets, two sets of protein ELP$_{BC}$ fusions, Trx and Fn3, retained the three state behavior of the ELP$_{BC}$ (unimer, micelle, and aggregate) as indicated by the similar pattern of change in absorbance with increasing temperature. The slight increase in absorbance indicates the formation of nanoparticles between the transition temperature of the hydrophobic and hydrophilic blocks. Both transitions were reversible for temperature ranges below protein denaturation temperature. BFP and VHH ELP$_{BC}$ fusion sets did not exhibit self-assembly behavior. The change in absorbance with temperature indicated a transition from unimer to aggregate with no temperature range in which stable nanoparticles form. An interesting observation was that each protein either disrupted or retained the self-assembly behavior of ELP$_{BC}$ over the entire range of block lengths and ratios.

In comparing the behavior of the four proteins when fused to ELP 96,60 to that of the free ELP 96,60, several observations can be made about the effect of the protein on the transition temperatures of the ELP$_{BC}$ (Figure 5). For both Trx and Fn3, the CMT did

not change compared to that of the corresponding free ELP_{BC}, suggesting that the fused proteins did not have an effect on the hydrophobic block transition temperature. However, fusion of these two proteins to the ELP_{BC}s had a significant effect on the micelle-to-aggregate transition temperature. The more hydrophobic protein, Fn3, depressed the micelle-to-aggregate transition temperature while the more hydrophilic one, Trx, elevated that transition temperature. These results agree with the previously observed "ΔT_t effect" of proteins fused to an ELP monoblock wherein the fused protein increases or decreases the T_t of an ELP depending on whether its accessible surface area is hydrophilic or hydrophobic. The BFP and VHH ELP_{BC} appear to transition at temperatures close to the CMT of the free ELP_{BC} suggesting that the entire protein ELP_{BC} fusion transitions as the hydrophobic block transitions. Although, BFP and VHH disrupt self-assembly of the diblock, the fusions do not behave exactly as a monoblock ELP would (Figure 6 and Figure 7). The transition observed for VHH and BFP ELP_{BC} fusions differs from ELP monoblocks in that it is not as smooth and sharp of a transition. VHH ELP_{BC} fusions, however, show an initial increase in absorbance that can be attributed to a small population of large particles (~200-300 nm as confirmed by DLS) (Figure 8). The VHH and BFP ELP_{BC} fusion behavior suggest one of two or both scenarios: 1) these proteins interact solely with the block they are fused to (i.e. with the hydrophilic block) leading to a decrease in its T_t thereby shifting it close to that of the hydrophobic block T_t so that one transition is observed or 2) proteins interact with the hydrophobic block and

prefer the environment of the core once it is formed forcing the hydrophilic block to transition.

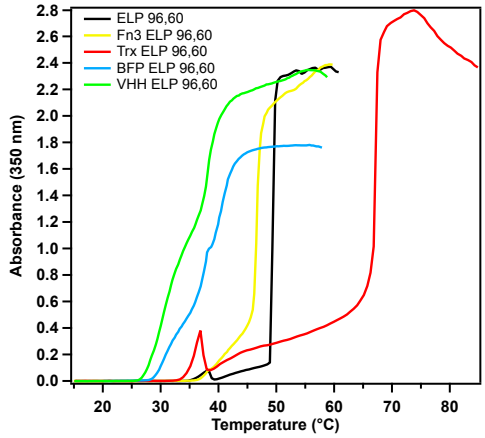

Figure 5: Thermal behavior of four protein ELP 96,60 fusions compared to free ELP 96,60. The absorbance at 350 nm was measured as samples at a concentration of 25 µM in PBS were heated at a rate of 1°C/min. Trx ELP 96,60 (red) and Fn3 ELP 96,60 (yellow) form micelles at the same temperature as free ELP 96,60 (black) but transition from micelle-to-aggregate at different temperatures compared to free ELP 96,60. The more hydrophilic protein, Trx, increases the micelle-to-aggregate transition compared to the free ELP 96,60. The more hydrophobic protein, Fn3, decreases the micelle-to-aggregate transition compared to the free ELP 96,60. BFP ELP 96,60 (blue) and VHH ELP 96,60 (green) show a transition close to the CMT.

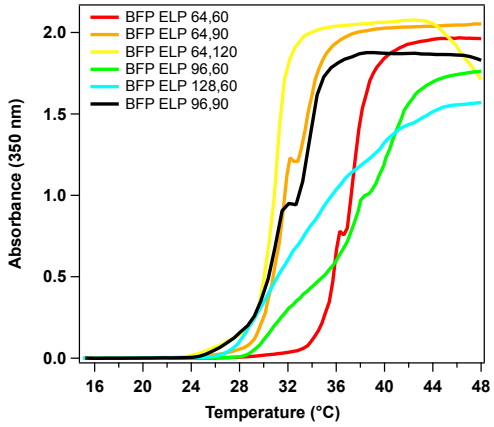

Figure 6: Thermal behavior of BFP ELP$_{BC}$ fusions. BFP is fused to six ELP diblocks with varying block lengths and ratios. The absorbance at 350 nm was measured as samples at a concentration of 25 µM in PBS were heated at a rate of 1°C/min.

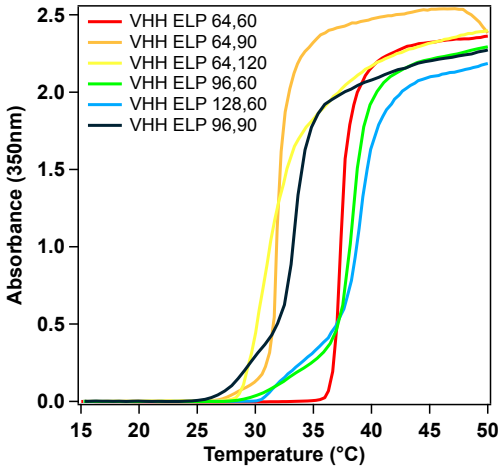

Figure 7: Thermal behavior of VHH ELP$_{BC}$ fusions. VHH is fused to six ELP diblocks with varying block lengths and ratios. The absorbance at 350 nm was measured as samples at a concentration of 25 μM in PBS were heated at a rate of 1°C/min.

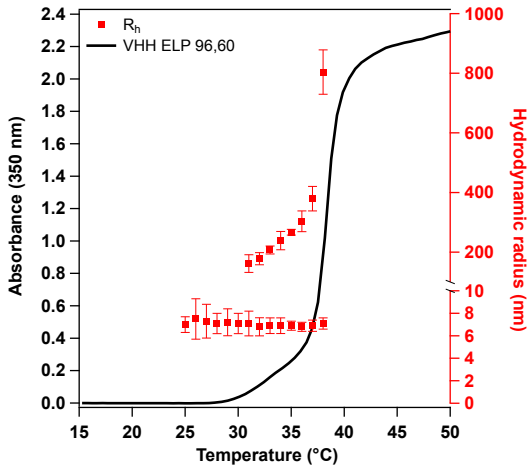

Figure 8: Thermal behavior of VHH ELP 96,60 as determined by temperature-programmed turbidity and dynamic light scattering. Hydrodynamic radius (red dots) shows that VHH ELP 96,60 transition from unimer to aggregate. The slight increase in O.D.350 (black line) between 30-35°C is due to formation of particles between ~200-400 nm that are 10% in mass of the sample.

The four proteins were chosen to control for protein properties such as molecular weight and hydrophilicity/hydrophobicity. Although as expected the more hydrophilic protein, Trx, did not disrupt self-assembly, BFP which is also hydrophilic, as determined

by the calculated hydrophobicity index, but has twice the molecular weight did disrupt self-assembly. VHH and Fn3 have similar molecular weights and hydrophobicities but had different effects. This suggests that the surface properties of the proteins have a complex interaction with the ELP_{BC} that requires quantification through experimental rather than computational methods.

Next, we examine the effect of the protein within one set of protein ELP_{BC} fusions. First, we examine the thermal behavior of proteins that do not disrupt self-assembly (Trx and Fn3 ELP_{BC} fusions) over the range of block lengths and ratios. Figure 9A shows the thermal profiles of three Trx ELP_{BC} fusions with increasing hydrophobic block lengths (60, 90 and 120 pentapeptide repeats). Increasing the hydrophobic block length decreased the CMT as consistent with the well-documented effect of increased length in decreasing monoblock ELP T_t[3] but the micelle-to-aggregate transition was unaffected. Similarly, Figure 10A shows the thermal profiles of Fn3 fused to the same three ELP_{BC}s. The same effect on the CMT with increasing hydrophobic block lengths was observed. However, the micelle-to-aggregate transition temperature is also affected; the transition temperature decreases with increasing hydrophobic block length. This effect is unexpected and has not been previously observed suggesting that the protein is affected by the hydrophobic block length and in turn affects the hydrophilic block.

Increasing the hydrophilic block length showed opposite trends for the hydrophilic (Trx) vs. the hydrophobic (Fn3) protein (Figure 9B and Figure 10B). For Trx,

increasing the hydrophilic block lengths (64, 96, and 128 pentapeptides) resulted in lower micelle-to-aggregate transition temperatures, which is also consistent with the effect of increased length on ELP T_t and the CMT was unaffected as expected. For Fn3, while the CMT remained unaffected, increasing the hydrophilic block lengths resulted in higher micelle-to-aggregate transition temperatures. This later unexpected effect may be due to the relative hydrophobicity of the protein which when attached to the shorter hydrophilic blocks is in closer proximity to the collapsed hydrophobic block and would favor that environment resulting in lower transitions temperatures.

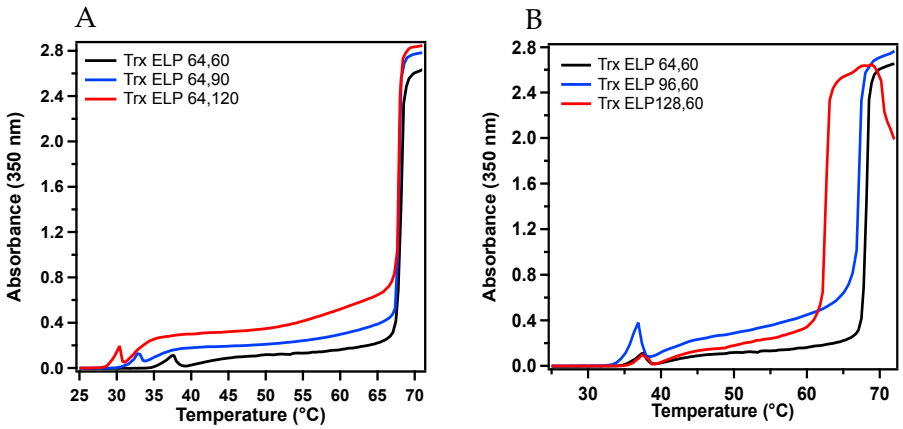

Figure 9: A. Thermal behavior of Trx ELP$_{BC}$ with a hydrophilic block with 64 pentapeptide repeats and increasing lengths of the hydrophobic block (60, 90, and 120 pentapeptide repeats). The absorbance at 350 nm was measured for a 25 μM solution in PBS while heating the samples at a rate of 1 °C/min. The unimer-to-micelle transition occurs at lower temperatures with increasing hydrophobic lengths. The micelle-to-aggregate transition is unaffected by the length of the hydrophobic block. B. Thermal behavior of Trx ELP$_{BC}$ with a hydrophobic block with 60 pentapeptide repeats and increasing lengths of the hydrophilic block (64, 96, and 128 pentapeptide repeats). The CMT is unaffected by the length of the hydrophilic block. The micelle-to-aggregate transition occurs at lower temperatures with increasing hydrophilic lengths.

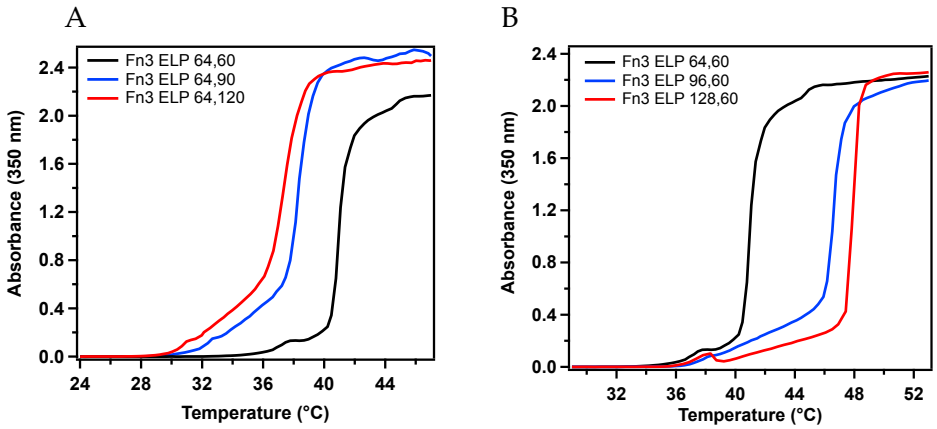

Figure 10: A. Thermal behavior of Fn3 ELP$_{BC}$ with a hydrophilic block with 64 pentapeptide repeats and increasing lengths of the hydrophobic block (60, 90, and 120 pentapeptide repeats). The absorbance at 350 nm was measured for a 25 μM solution in PBS while heating at a rate of 1 °C/min. The CMT and micelle-to-aggregate transition are both affected by the length of the hydrophobic block; both transitions occur at lower temperatures with increasing length of the hydrophobic block. B. Thermal behavior of Fn3 ELP$_{BC}$ with a hydrophobic block with 60 pentapeptide repeats and increasing lengths on the hydrophilic block (64, 96, and 128 pentapeptide repeats). The micelle-to-aggregate transitions occur at higher temperatures with increasing hydrophilic lengths while the CMT is unaffected.

Figure 11 shows the effect of concentration on the thermal behavior of Trx ELP 64,120. As observed previously from studying the thermal behavior of the diblocks, the CMT is affected more than the micelle-to-aggregate transition by the change in concentration. While the CMT decreased by ~3.3°C when the concentration is increased from 10μM to 100μM, the micelle-to-aggregate transition only drops by ~0.7°C. In addition, the increase in absorbance pattern suggests that self-assembly is observed over the range of concentrations between 10 μM and 100 μM; however, for further characterization a concentration of 25 μM is preferable as this concentration is well above the critical micelle concentration but avoids the large continuous increase in

absorbance the 100 μM concentration shows over the micelle-forming temperature range.

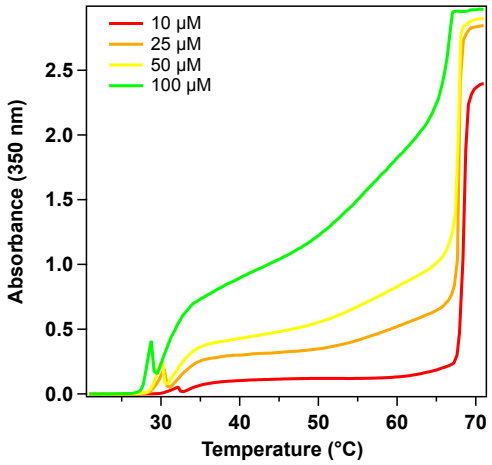

Figure 11: Thermal behavior of Trx ELP 64,120 at various concentrations (10, 25, 50 and 100 μM). The absorbance at 350 nm was measured for a solution at a given concentration in PBS while heating at a rate of 1°C/min. Increasing the concentration lowers the CMT and to a lesser extent the micelle-to-aggregate transition temperature.

Next, we examine the effect of proteins that do disrupt self-assembly behavior (BFP and VHH ELP$_{BC}$s) on the thermal behavior of ELP$_{BC}$. Although BFP and VHH disrupt self-assembly, the transition temperature of BFP and VHH ELP$_{BC}$ decreases with increasing hydrophobic block length (60, 90, 120) as seen in Figure 12 but does not appear to be significantly affected by the protein attached. In addition, both BFP and VHH ELP$_{BC}$ transitions are concentration dependent. However, as can be observed from Figure 13 and Figure 14, the temperature at which the absorbance starts to increase is unaffected by the concentration.

A few factors were investigated to better understand the disruption of self-assembly by VHH. First, although Fn3 and VHH are the same molecular weight and

hydrophobicity, Fn3 is separated from the ELP_{BC} by a hydrophilic peptide linker (GGTSGGTSGS) and this linker is not accounted for in the hydrophobicity index calculations, as it is not part of the crystal structure. To control for the effect of this linker, a VHH-GGTSGGTSGS-ELP 96,90 construct was synthesized and expressed. The thermal behavior is compared to that of VHH ELP 96,90 and no significant difference is observed (Figure 15). Second, to investigate the thermal denaturation of VHH, VHH ELP 96,90 was thermally cycled through two rounds of heating to a maximum of 50°C and cooling to 15°C and the transition was found to be reversible and reproducible through two cycles (Figure 16). However, when the sample was incubated at 75°C to thermally denature the sample, cooled to 15°C, and then the absorbance was measured as the sample was heated from 15°C to 50°C at a rate of 1°C/min again, the sample remains turbid with a starting O.D. 350 of 1.5 indicating an irreversible aggregation occurred upon heating to 75 °C that was not previously observed but a transition still occurs near the initial increase in absorbance observed for the previous two thermal cycles. Finally, to eliminate the possibility that VHH is unfolded due a unformed disulfide bond due to the reducing environment of the *E. coli* cytoplasm, VHH ELP 96,90 was expressed and purified from a modified *E. coli* strain Shuffle® T7 express as it has been shown that successful purification of VHH from this strain yields a folded functional protein[96]. This strain has been modified to enable formation of disulfide bonds within the cytoplasm through the deletions of the genes for glutaredoxin

reductase and thioredoxin reductase (*Δgor ΔtrxB*). In addition, this strain contains a chromosomal copy of the periplasmic disulfide bond isomerase DsbC which has been shown to promote disulfide bond formation. As seen in Figure 17, VHH expressed within the oxidizing environment still disrupted the self-assembly of ELP 96,90. Furthermore, resuspending VHH ELP 96,90 in 20 mM TCEP and dialyzing does not affect the thermal behavior (neither does the presence of TCEP in solution during the thermal scan). In conclusion, while these sets of experiments do not preclude that VHH could be unfolded, they strongly suggest that VHH's effect is not due to unfolding but to its surface properties and interactions with the ELP$_{BC}$.

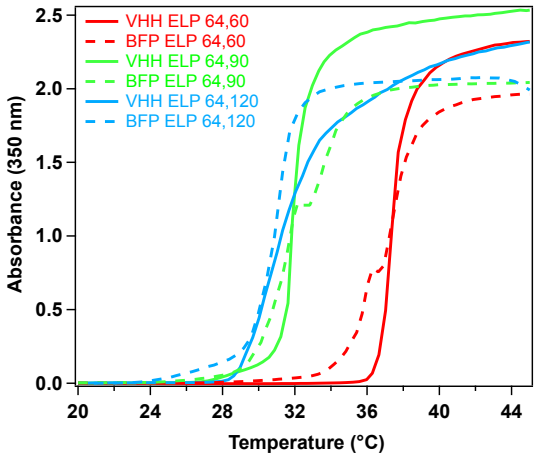

Figure 12: Thermal behavior of VHH ELP$_{BC}$ and BFP ELP$_{BC}$ with 64 pentapeptide repeats of the hydrophilic block and increasing lengths of the hydrophobic block (60, 90, and 120 pentapeptide repeats). The absorbance at 350 nm was measured for a 25 μM sample in PBS while heating at a rate of 1°C/min. The transition temperature decreased with increasing hydrophobic block length.

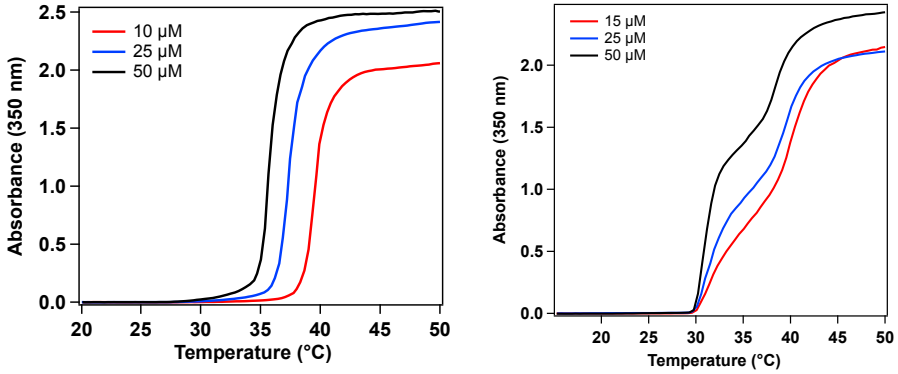

Figure 13: Concentration dependence of thermal behavior of VHH ELP 96,60 (left) and VHH ELP 128,60 (right). The absorbance at 350 nm was measured for a sample in PBS that is heated at a rate of 1°C/min. As expected, increasing the concentration decreased the transition temperature. However, the point at which the initial increase in absorbance is observed for VHH ELP 128,60 is not affected by an increase in concentration.

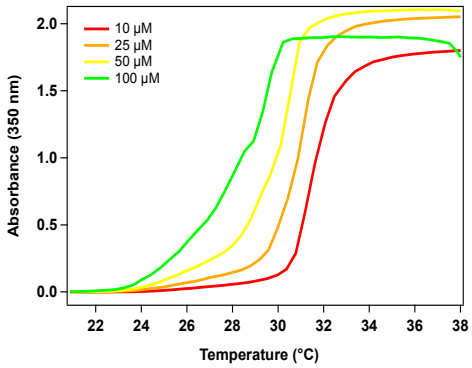

Figure 14: Concentration dependence of thermal behavior of BFP ELP 64,120. The absorbance at 350 nm was measured for a sample in PBS that is heated at a rate of 1°C/min. As expected, increasing the concentration decreased the transition temperature. However, the point at which the initial increase in absorbance is observed is not affected by an increase in concentration.

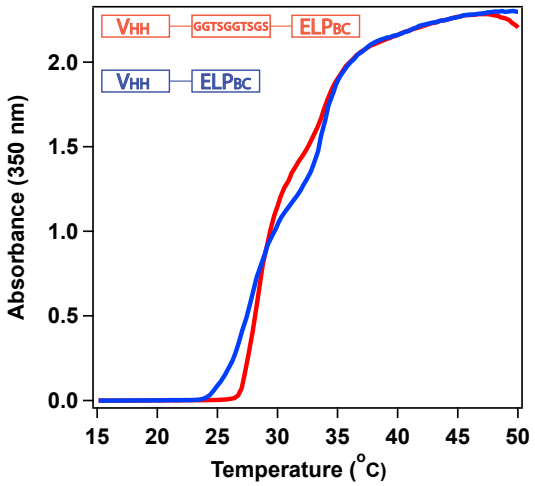

Figure 15: Thermal behavior of VHH ELP 96,90 (blue) and VHH-GGTSGGTSGS-ELP 96,90 (red). The absorbance at 350 nm was measured for a 25 µM sample in PBS while heating at a rate of 1°C/min. The hydrophilic linker between VHH and ELP 96,90 does not affect the thermal behavior of the fusion.

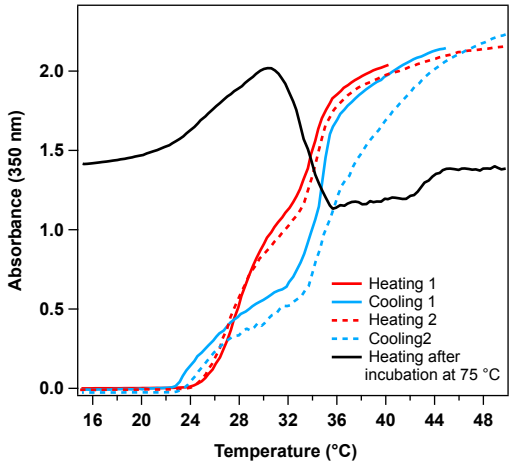

Figure 16: Thermal cycling of VHH ELP 96,90. The absorbance at 350 nm was measured for a 25 µM sample while heating and cooling at a rate of 1°C/min. The sample was cycled through two thermal cycles and the thermal behavior was found to be reversible and reproducible. However, if the sample is incubated at 75°C and then heated from 15°C to 50°C, the sample is turbid and shows a broad transition starting from the same temperature as the two previous thermal cycles.

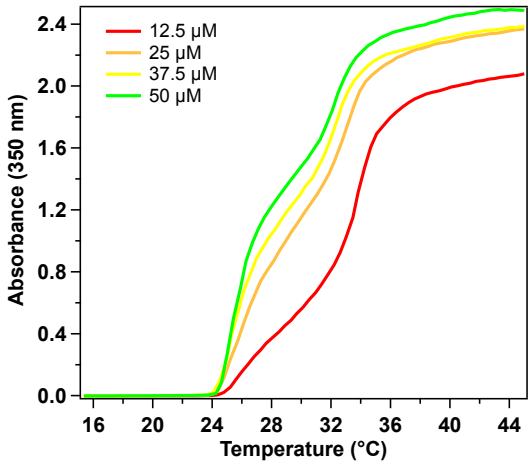

Figure 17: Thermal behavior of VHH ELP 96,90 expressed and purified from SHuffle® cells at a range of concentrations. The absorbance at 350 nm was measured for a sample in PBS while heating at a rate of 1°C/min. VHH still disrupts the self-assembly behavior of ELP 96,90.

The four proteins were fused to a monoblock ELP with the same composition as the hydrophilic block and is 96 pentapeptides long (ELP[V_1:A_8:G_7]-96) to observe the effect of the protein on the known simple behavior of one ELP segment as opposed to the complexity inherent in the ELP_{BC} thermal behavior (Figure 18). From previous work, it is known that the effect of the protein on the transition temperature correlates with its surface properties (i.e. hydrophobicity/hydrophilicty). The transition temperature of ELP[V_1:A_8:G_7]-96 is not within a measurable range of temperatures; however, a trend among the four proteins can still be observed. Although hydrophobicity index calculations indicate that Fn3 and VHH are of the same hydrophobicity, the transition temperature of the Fn3 ELP[V_1:A_8:G_7]-96 is 10°C higher than that of VHH ELP[V_1:A_8:G_7]-96 indicating that VHH is more hydrophobic. BFP has a wide transition which could

affect the self-assembly behavior when attached to the ELP_{BC} disrupting a clean unimer-to-micelle transition and in addition the transition temperature is lower by ~25 °C than that of Trx which has similar hydrophobicity index, indicating that BFP is more hydrophobic than initially predicted. Trx as expected has the highest transition temperature. However, as Trx is predicted to increase the transition temperature of the ELP, ELP[V_1:A_8:G_7]-96 has no observable transition below 90°C, and Trx has a melting temperature of 75 °C, the observed increase in absorbance could be due to denaturation. Upon the addition of 0.5M NaCl the transition temperature of ELP[V_1:A_8:G_7]-96 and Trx-ELP[V_1:A_8:G_7]-96 drops to 65 °C and 70°C respectively. The transition temperatures were measured in the presence of 0.5M NaCl to ensure that increase in absorbance for the three other proteins is not due to denaturation of the protein. Denaturation temperature should not be significantly affected by the presence of 0.5 M NaCl while the phase transition is highly sensitive to the increase in ionic strength. As seen in Figure 18, all the transition temperatures are suppressed by the addition of salt indicating that the increase in absorbance is due to a phase transition rather than denaturation.

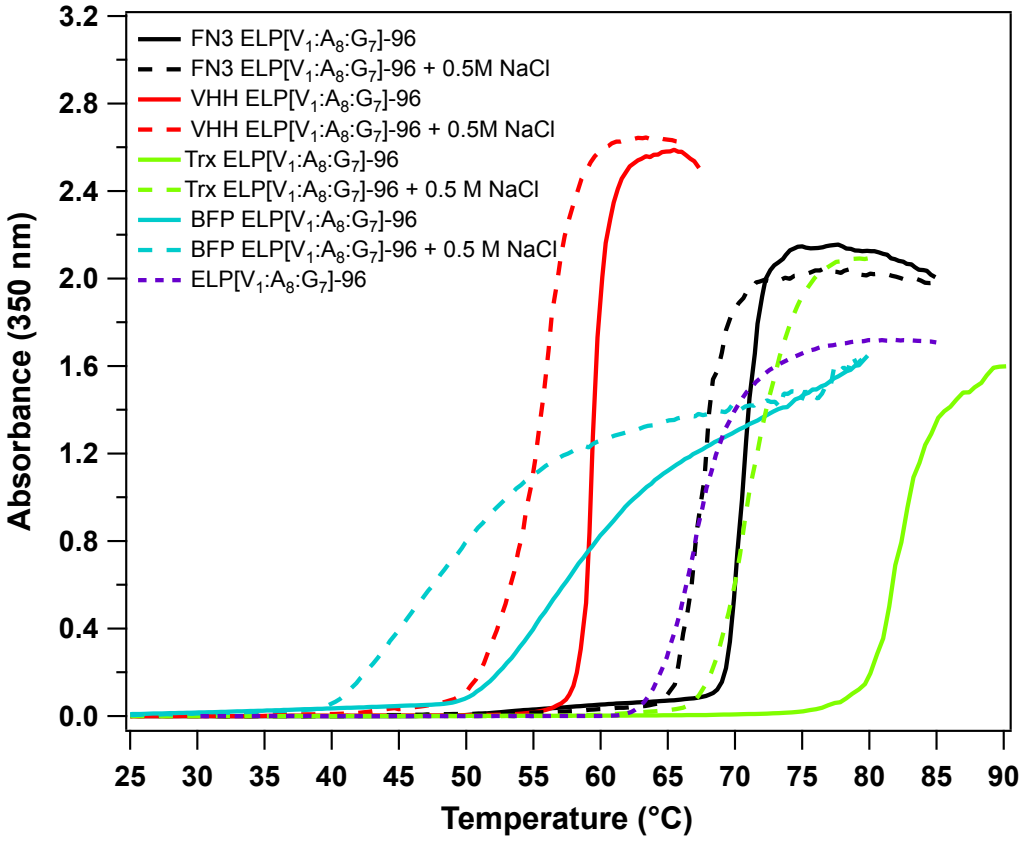

Figure 18: Thermal behavior of four protein ELP[V_1:A_8:G_7]-96 fusions without (solid lines) and with (dashed lines) 0.5 M NaCl. The absorbance at 350 nm was measured for a 25 μM sample in PBS that is heated at a rate of 1°C/min.

2.3.2 Dynamic and static light scattering

The protein ELP_{BC} fusions, which did self-assemble, were further characterized by light scattering. Light scattering is a more accurate and sensitive method compared to turbidity measurements to characterize the self-assembly of ELP_{BC}. Dynamic and static light scattering measure different physical quantities that together indicate the topology of the particle.

First, the thermal behavior as determined by the change in absorbance upon heating was verified by DLS. DLS was carried out to determine the change in hydrodynamic radius (R_h) as the temperature was increased in 1°C increments. The measured radii and the change in absorbance are plotted together in Figure 19. The change in R_h with temperature confirms the three-state behavior (unimer, micelle and aggregate) for Trx ELP_{BC} and Fn3 ELP_{BC} fusions. The transition temperature at which the unimer assembles into a micelle as measured by DLS agrees with that measured by the change of absorbance as a function of temperature. Below the CMT, the protein ELP_{BC} fusions are unimers with R_h in the range of 6-7.5 nm. Above their CMT, the protein ELP_{BC} fusions formed monodisperse nanoparticles with radii in the range of 24-36.6 nm depending on the protein and ELP_{BC}. Similarly, upon further increase in temperature past the CMT, the collapse of the hydrophilic block resulted in the formation of micron-sized aggregates. These aggregates were first detected by DLS at the same temperature at which the large step increase in absorbance occurs. However, this data is not included as measurements of these aggregates are not accurate and the aggregates are not stable; they phase separate into globules and sediment.

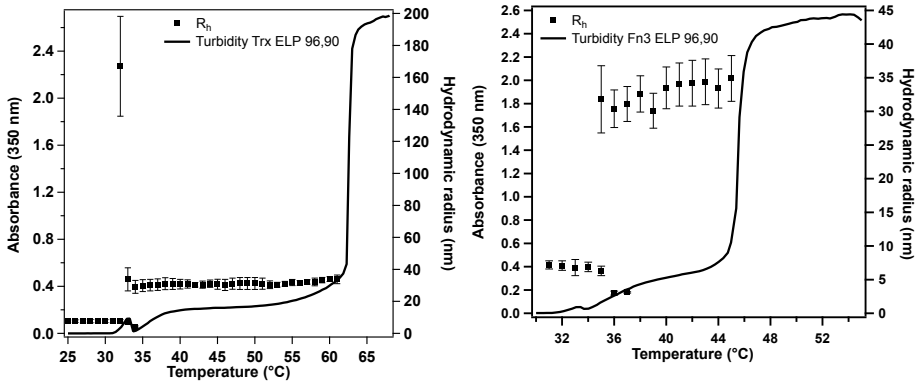

Figure 19: Left: Thermal behavior as determined by change in absorbance and hydrodynamic radius (R_h) with increasing temperature for Trx ELP 96,90 at 25 μM in PBS. The thermal behavior correlates between the two methods. The unimer (7 nm) transitions into a micelle (31 nm) at 35 °C. The R_h of the micelle is constant until the micelle-to-aggregate transition at ~62 °C. Right: Thermal behavior as determined by change in absorbance and hydrodynamic radius with increasing temperature for Fn3 ELP 96,90 at 25 μM in PBS. The thermal behavior correlates between the two methods. The unimer (7 nm) transitions into a micelle (35 nm) at 35 °C. Thermal behavior of all protein ELP_{BC} fusions as determined by DLS is presented in Appendix A.

The DLS measurements showed no significant changes in R_h with increasing temperature over the temperature range for which nanoparticles were detected. The effect of protein ELP_{BC} fusion concentration on the micelle size was examined for Trx ELP 96,90. No significant change in R_h was observed over a range of concentrations above the critical micelle concentration (CMC) (Figure 20). The change in R_h with temperature and concentration was measured using a detector set to a scattering angle of 90°. However, additional information can be obtained by measuring R_h at different scattering angles. R_h showed no dependence on angle, which indicated that the particles were monodisperse and spherical (Figure 21)[97].

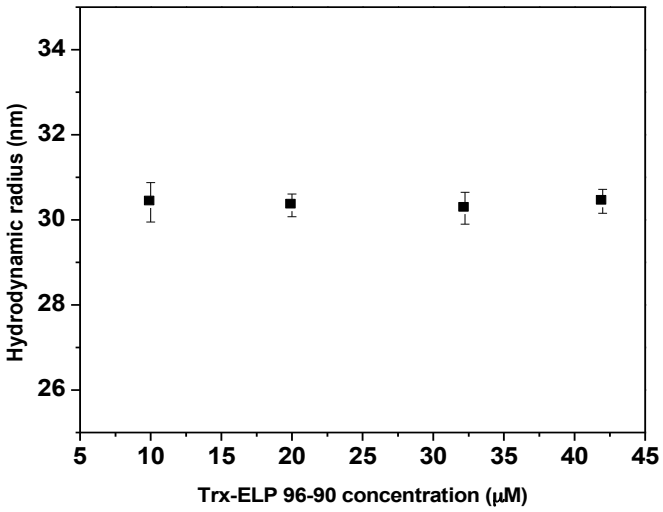

Figure 20: Influence of concentration on hydrodynamic radius of Trx ELP 96,90 micelles at 40 °C. No change in hydrodynamic radius of the micelles is observed over a range of concentrations.

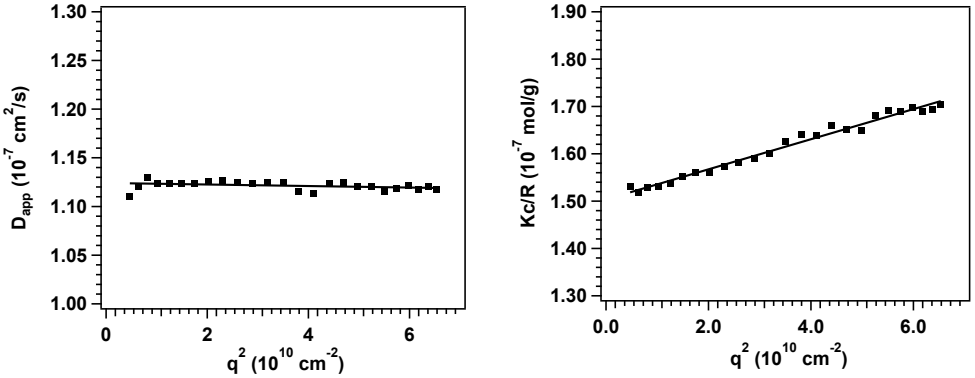

Figure 21: Light scattering of Trx ELP 96,90 at 40°C in PBS at 1 g/L. The left panel shows the change in the apparent diffusion coefficient with change in scattering wavevector as measured by DLS. No angular dependence was observed indicating monodisperse spherical particles. The right panel shows a Zimm plot obtained at a range of angles (30° to 150°) by SLS. The intercept was used to calculate the M_W while the slope was used to calculate R_g. The M_W was found to be 6.6 x 10^6 g/mol while R_g was determined to be 25 nm.

SLS measurements were performed by measuring the intensity of light scattered as a as a function of scattering angle to create a Zimm plot and from the linear fit the

molecular weight and radius of gyration (R_g) were calculated (Figure 21). The properties of the nanoparticles formed by the two sets of protein ELP_{BC} fusions are summarized in

Table 3. The molecular weight of the particle allows calculation of the aggregation number (i.e. number of unimers per micelle). The aggregation numbers of both sets range from 30 to 150 unimers/micelle, which is typical for micelles. These numbers were not corrected for the CMC. The R_g was used to determine the ratio of R_g to R_h, known as ρ, which is indicative of the topology of the nanoparticle. Theoretically, a hard uniform sphere has a ρ value of 0.775; a hollow sphere has a ρ value of 1; and a random coil has a ρ value of 1.5[97]. Lower ρ values than the theoretical hard sphere ρ value are observed for soft spherical particles such as micelles[98, 99]. Trx ELP_{BC} nanoparticles have ρ values of 0.6-0.82 and Fn3 ELP_{BC} nanoparticles have ρ values of 0.6-0.74. These values indicate the formation of spherical micelles by both protein ELP_{BC} fusion sets.

Table 3: SLS and DLS measurements of protein ELP$_{BC}$

Protein ELP$_{BC}$	MW (kDa)*	Temp (°C)	R_g (nm)	R_h (nm)	ρ	Aggregation number**
Trx ELP 64,60	61	45	16.2	24.0	0.68	32
Trx ELP 64,90	75	40	19.3	27.9	0.69	78
Trx ELP 64,120	86	40	22.3	32.2	0.69	49
Trx ELP 96,60	75	45	21.8	28.7	0.76	68
Trx ELP 128,60	87	50	19.6	28.5	0.69	61
Trx ELP 96,90	86	40	25.2	30.6	0.82	81
Fn3 ELP 64,90	73	35	20.8	31.1	0.67	88
Fn3 ELP 64,120	84	35	26.5	36.6	0.72	150
Fn3 ELP 96,60	73	45	24	32.4	0.74	139
Fn3 ELP 128,60	85	45	18.7	31.0	0.60	69
Fn3 ELP 96,90	84	40	23.5	34.9	0.67	122

* Theoretical unimer MW
**Not corrected for CMC

To determine the effect of temperature on the properties of the micelles, Fn3 ELP 96,90 R_g and aggregation number were measured at three temperatures (Figure 22). A significant change in the aggregation number is observed as it increased by ~40% over a 4°C range. However, no significant change is observed for R_g suggesting a perhaps denser core with increased temperature. In addition, the change in aggregation number suggests that for multivalent display of targeting ligands, the temperature at which the

treatment is administered (body temperature or hyperthermia) will change the density of the displayed ligands.

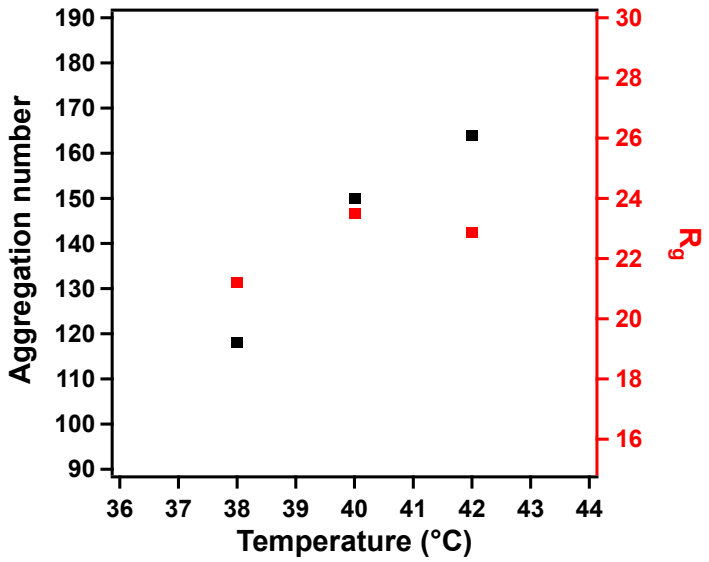

Figure 22: Change in aggregation number (black) and R_g (red) with increasing temperature for Fn3 ELP 96,90 at 25 μM. A significant change in aggregation number is observed but R_g does not significantly change with temperature.

The CMC can be determined through fluorescent techniques that rely on the partitioning of hydrophobic dyes such as pyrene into the core. However, a more accurate method is SLS measurements of weighted average molecular weight at various concentrations. Figure 23 shows the weighted average molecular weight of Fn3 ELP 96,90 at 40°C at concentrations from 0.1 g/L to 1.6 g/L. At concentrations below 0.6 g/L, the aggregation number starts to decrease; however, even below 0.1 g/L the aggregation numbers indicate micelles are still present. The CMC, defined as the concentration at which the unimer concentration is equal to that of the unimers incorporated into micelles, is between 0.1-0.2 g/L (i.e. ~1-2 μM).

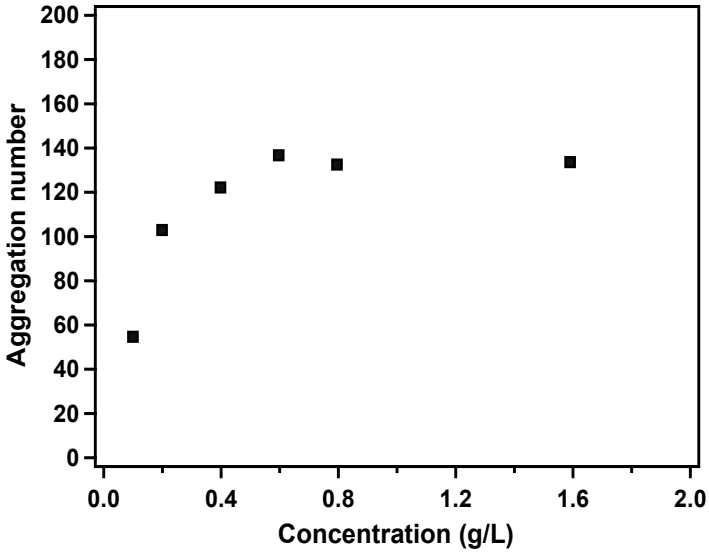

Figure 23: Change in aggregation number of Fn3 ELP 96,90 with decreasing concentrations at 40°C.

2.3.3 Cryogenic-Transmission Electron Microscopy of Elastin-like polypeptide micelles

To directly visualize the self-assembled structures, cryogenic-Transmission Electron Microscopy (cryo-TEM) images of Trx ELP 96,90 micelles were obtained for samples prepared at 55 °C, which for this protein ELP_{BC} fusion is above its CMT (Figure 24). The images show spherical particles that are larger than 50 nm in diameter, which corresponds to the measured hydrodynamic diameter of 61.2 nm for this construct. No other particle morphologies were observed in the cryo-TEM images.

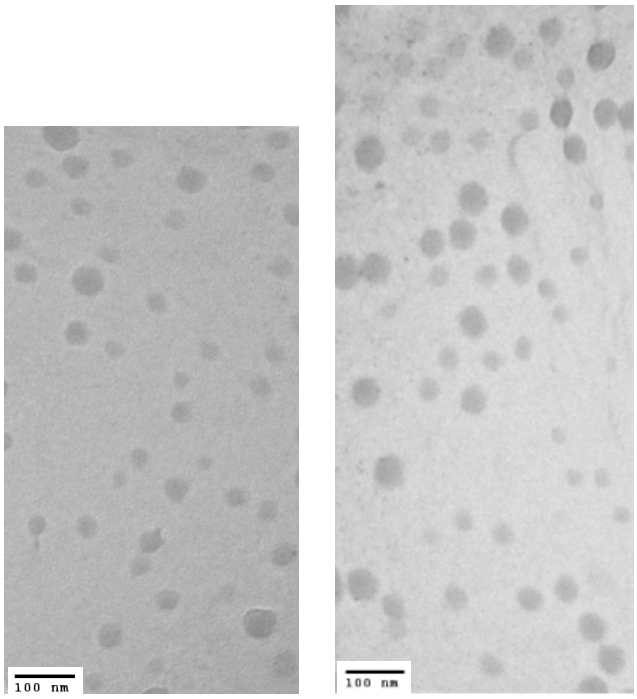

Figure 24: Cryo-TEM of Trx ELP 96,90 vitrified at a temperature that induced micelle formation (55 °C) in PBS at 10 μM. Panels A and B are different representative images of the micelles; both panels show spherical particles of diameter ~ 60 nm.

2.3.4 Bioactivity of proteins presented on Elastin-like polypeptides micelles

To determine the bioactivity and availability of proteins when fused to micelle-forming ELP_{BC}, the binding of Fn3 to its target $\alpha_v\beta_3$ integrin was assessed when Fn3 was fused to ELP 96,90. A transfected human leukemia cell line, K562, that overexpresses the $\alpha_v\beta_3$ integrin (K562/$\alpha_v\beta_3$) was available from previous studies, as was the wild-type K562 cell line (K562/WT) that exhibits low baseline level of expression of this integrin. The binding of a fluorescently labeled Fn3 ELP 96,90 was measured below and above the CMT (room temperature and 38°C respectively) to determine the effect of micellar presentation of the Fn3 domain on cell uptake in comparison to the unimeric form. ELP

96,90 was used as a ligand-negative ELP control to measure the nonspecific cell uptake of ELP micelles. The binding was quantified through flow cytometry. The fluorescence intensity histogram of K562/$\alpha_v\beta_3$ cells showed a shift towards more fluorescent cells when they were exposed to Fn3 ELP_{BC} micelles (38°C) as compared to unimers (room temperature) (Figure 25 top) indicating that multivalent display by micelles is more effective at promoting cell uptake than the unimers. Interpretation of this result is however convoluted by two effects: the effect of micelle self-assembly and that of multivalency. To deconvolute these effects from each other, cell uptake by K562/$\alpha_v\beta_3$ cells was compared for Fn3 ELP 96,90 micelles with the ligand-negative ELP96,90 micelles (Figure 25 middle). Fn3 ELP 96,90 micelles showed significantly greater uptake as compared to the ligand-negative ELP 96,90 micelles, indicating that the effect observed in Figure 25 is largely due to the multivalent presentation of the Fn3 domain, rather than the self-assembly of the ELP 96,90 into micelles. Integrin-mediated uptake was also confirmed by using the receptor-negative control K562/WT cell line that does not overexpress the $\alpha_v\beta_3$ integrin. A significant increase in fluorescence intensity was observed when Fn3 ELP 96,90 micelles were incubated with K562/$\alpha_v\beta_3$ cells in comparison to K562/WT cells (Figure 25 bottom). These findings confirm that highest uptake occurs when cells overexpressing the $\alpha_v\beta_3$ integrin are incubated with ELP_{BC} micelles that present multiple copies of the Fn3 domain, as such, this result would indicate that the Fn3 is still bioactive and present at the surface of the micelle.

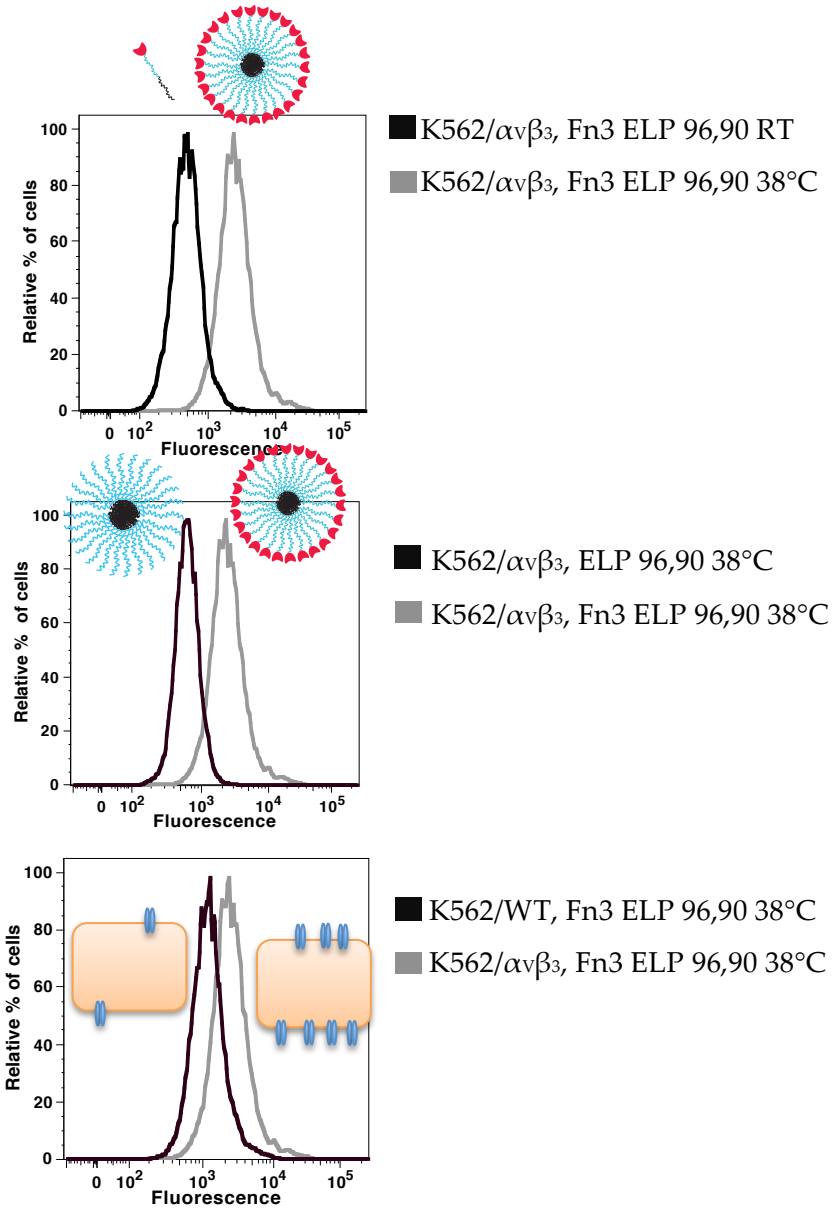

Figure 25: Flow cytometry analysis of K562/WT and K562/αvβ3 cells following incubation with 10 μM Fn3 ELP 96,90 or ELP 96,90, above and below CMT. The top panel shows the histograms of K562/αvβ3 cells incubated with Fn3 ELP 96,90 above (gray) and below (black) CMT. A shift in the median fluorescence was observed indicating enhanced uptake of Fn3 ELP 96,90 micelles compared to unimers. The middle panel shows the histograms of K562/αvβ3 cells incubated with Fn3 ELP 96,90 (gray) and ELP 96,90 (black). A shift in the median fluorescence was observed indicating enhanced uptake of Fn3 ELP 96,90 over ELP 96,90. The bottom panel shows the histogram of K562/WT (black) and K562/ αvβ3 (gray) cells incubated with Fn3 ELP 96,90 above the CMT. A shift in the fluorescence median is observed indicating enhanced uptake for K562/αvβ3 cells.

The fold-increase of the median fluorescent intensities of K562/$\alpha_v\beta_3$ and K562/WT cells above the CMT (micelle) compared to that below the CMT (unimer) is plotted for cells treated with Fn3 ELP 96,90 and ELP 96,90 in Figure 26. No significant difference was observed between the two cell lines (K562/WT and K562/$\alpha_v\beta_3$) when incubated with ligand-negative ELP 96,90. However, a significant difference in the fold-increase was observed for the cell lines incubated with Fn3 ELP 96,90; double the fold increase is observed for K562/$\alpha_v\beta_3$ cells compared to K562/WT indicating enhanced uptake in the presence of the Fn3 domain. These results clearly show that the Fn3 domain presented on the ELP_{BC} micelle is bioactive and exhibits improved targeting and uptake by multivalent presentation as compared to its unimer.

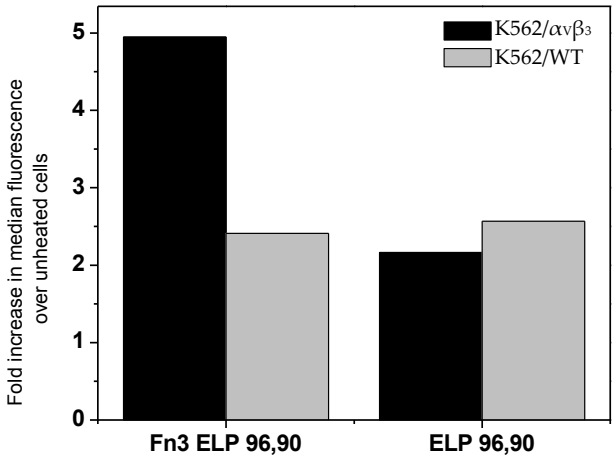

Figure 26: Fold increase in median fluorescence of K562/WT and K562/$\alpha_v\beta_3$ cells incubated above the CMT over those incubated below the CMT. The cells were incubated with 10 μM of either Fn3 ELP 96,90 or ELP 96,90. K562/$\alpha_v\beta_3$ cells (black) show higher fold increase only when incubated with Fn3 ELP 96,90.

2.4 conclusion

Proteins can be seamlessly fused to ELP_{BC}. Of the four protein ELP_{BC} fusions created, Trx and Fn3 ELP_{BC} still showed self-assembly behavior. The proteins affected the temperature range in which self-assembly is observed by changing the micelle-to-aggregate transition while the CMT was unaffected. The surface properties of the protein dictated whether the micelle-to-aggregate temperature increased or decreased similar to the "ΔT_t effect" observed for monoblock ELPs. The protein ELP_{BC} fusions still formed micelles ranging between 24-37 nm as evidenced by DLS/SLS and cryo-TEM. The proteins are available on the surface of the micelle as evidenced by the bioactivity and multivalency of Fn3 when in micellar form. VHH and BFP disrupted the self-assembly of ELP_{BC} and one transition at the temperature corresponding to that of the hydrophobic block is observed. The molecular weight as well as the broadening of the phase transition could be the reason that BFP disrupts assembly. For VHH, it was found that experimentally its hydrophobicity is larger than the calculations based on its structure as determined by its effect in depressing the T_t of a monoblock ELP. Also, no evidence of the denaturation of VHH was found indicating that VHH is perhaps simply too hydrophobic to remain in solution in the presence of a collapsed hydrophobic core. Interestingly, the four proteins either retained or disrupted self-assembly behavior of all six ELP_{BC} regardless of block length or ratio.

3. Exploring effect of diblock composition on self-assembly of protein ELP diblock fusions

3.1 Introduction

In understanding the behavior of protein ELP_{BC}, one variable worth examining is the effect of the ELP blocks' relative hydrophobicity/hydrophilicity on the self-assembly process. Trx and Fn3 affected the micelle-to-aggregate transition temperature, which indicates that the proteins alter the behavior of the hydrophilic block. Therefore, BFP and VHH may disrupt self-assembly by decreasing the micelle-to-aggregate transition temperature sufficiently that the hydrophilic block no longer transitions independently of the hydrophobic block. The hypothesis; therefore, is that an increase in the difference in T_t between the two blocks could create micelles capable of self-assembling with proteins such as BFP and VHH which disrupted the previous ELP_{BC} self-assembly. This hypothesis will be explored by altering the T_t of the ELP blocks through changing the guest residue compositions, which can be precisely controlled at the genetic level. The change in guest residue, and hence T_t, effectively alters the hydrophobicity and hydrophilicity of the two blocks making the difference in amphiphilicty greater.

The new compositions were chosen based on the ELP-based amino acid hydrophobicity scale developed by Urry et al. which tabulates the T_t values for ELPs with one single amino acid as its guest residue for each of the 20 amino acids[2, 16]. Herein, this T_t will be referred to as the characteristic T_t for that amino acid (T_{tc}). The scale was used as a predicative guide rather than an accurate quantitative scale. Three amino acids

were chosen to increase the hydrophobicity of the core block: leucine, isoleucine and tryptophan with T_{tc} values of 5°C, 10°C, -105°C respectively. These T_{tc} values are a significant drop compared to that of valine (T_{tc} of 26°C), valine being the sole guest residue of the hydrophobic block of the initial ELP_{BC} set. While these residues were chosen to increase the hydrophobicity of the core, the corona was also altered to become more hydrophilic (i.e. higher T_t). To increase the hydrophilicity of the corona block compared to the previous block, ELP[V_1:A_7:G_8], the valine residue was eliminated so that only alanine and glycine are the guest residues present at a ratio of 1:1. Eliminating the valine residue results in an increase of approximately 20°C in T_t. However, the maximum hydrophilicty is obtained by using serine as a guest residue (T_{tc} of 60°C) as it has the highest T_{tc} for an uncharged residue.

Using the newly chosen guest residues, seven new ELP_{BC} were designed and are listed in Table 4 and illustrated in Figure 27. Hydrophobic blocks are combined with the hydrophilic blocks as follows: 1) **WELP**: a hydrophilic block with a guest residue composition of alanine and glycine at a ratio of 1:1 and a pentapeptide repeat length of 80 (ELP[A_1:G_1]-80) is fused to a hydrophobic block with a guest residue composition of tryptophan and valine at a ratio of 1:4 respectively and a pentapeptide repeat length of 40 or 80 (ELP[W_1:V_4]-40 or ELP[W_1:V_4]-80). 2) **LELP** and **IELP**: a hydrophilic block with a guest residue composition of alanine and glycine at a ratio of 1:1 and a pentapeptide repeat length of 80 (ELP[A_1:G_1]-80) is fused to a hydrophobic block composed of two

blocks: the first with a guest residue composition of valine and a pentapeptide repeat length of 40 followed at the C-terminal by a 40 pentapeptide block with guest residue of either leucine or isoleucine. **4) ELP S-80-V-40:** a hydrophilic block with serine as a guest residue and pentapeptide repeat length of 80 is fused to a hydrophobic block with a guest residue composition of valine and a pentapeptide repeat length of 40. 5) **ELP S-80-V-80:** a hydrophilic block with serine as a guest residue and pentapeptide repeat length of 80 is fused to a hydrophobic block with a guest residue composition of valine and a pentapeptide repeat length of 80. **6) ELP S-80-W-40:** a hydrophilic block with serine as a guest residue and pentapeptide repeat length of 80 is fused to a hydrophobic block with a guest residue composition of tryptophan and valine at a ratio of 1:4 respectively and a pentapeptide repeat length of 40.

Table 4: Composition of new ELP$_{BC}$

ELP$_{BC}$	Hydrophilic Block	Hydrophobic Block
WELP	[A_1:G_1]-80	[W_1:V_4]-40 or 80
LELP	[A_1:G_1]-80	[V]-40, [L]-40
IELP	[A_1:G_1]-80	[V]-40, [I]-40
ELP S-80-V-40	[S]-80	[V]-40
ELP S-80-V-80	[S]-80	[V]-80
ELP S-80-W-40	[S]-80	[W_1:V_4]-40

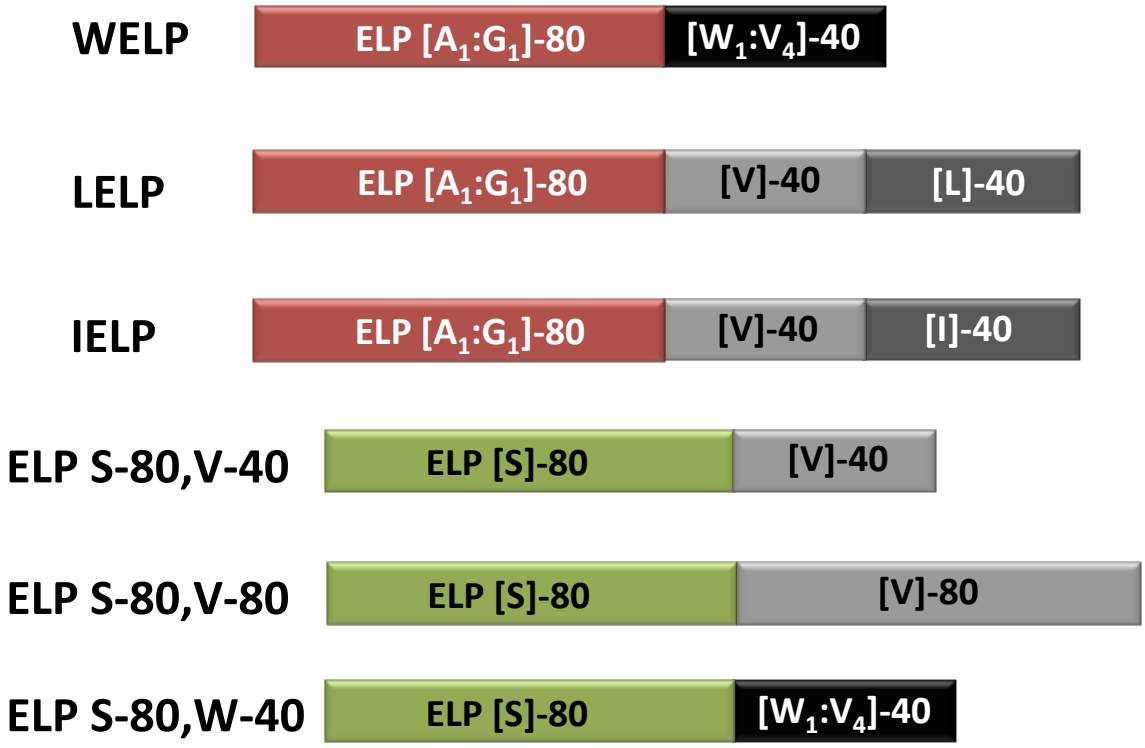

Figure 27: Schematic of new ELP$_{BC}$ architecture.

In creating this set of ELP$_{BC}$, we wish to understand how the degree of hydrophobicity/hydrophilicity and the length of the block affect the transition temperature of the other block and thereby the micelle-forming temperature range. An additional consideration is that these ELP$_{BC}$ could form nanostructures of morphologies other than spherical micelles. Thus, the self-assembly behavior of the ELP$_{BC}$ is first studied and consequently, the effect of the protein can be examined on the self-assembly of ELP$_{BC}$ with different compositions.

3.2 Methods

3.2.1 Synthesizing new ELP_{BC}

New hydrophilic blocks and hydrophobic blocks were synthesized and fused at the genetic level using a method termed recursive directional ligation by plasmid reconstruction (PRe-RDL)[100]. Briefly, an oligomer encoding for 5 or 10 pentapeptide repeats was inserted into a modified pET24d+. The modified pET24d+ has an oligomer encoding for unique restriction enzyme sites (BseRI and AcuI) as well as a start and stop codon. The plasmid was digested with BseRI and ligated to an excess of the oligomers encoding the pentapeptides in what is termed the concatemerization reaction. After screening for the plasmid containing the ELP oligomer, the plasmid was digested in two separate reactions with either BseRI and BglI or AcuI and BglI. The digested fragments were separated using electrophoresis and the fragment containing the ELP oligomer in each digestion reaction was purified. The two fragments containing the ELP oligomer from the two reactions were ligated to reassemble the plasmid and double the size of the ELP. The process was repeated to obtain the desired length of ELP. The ELP_{BC} were then fused in a similar fashion such that the hydrophilic block was contained in the fragment generated by the BseRI and BglI reaction while the hydrophobic block was contained in the fragment generated by the AcuI and BglI reaction. Upon ligation, the two ELP blocks were fused at the genetic level. The ELP_{BC} were expressed in BL21(DE3) *E. coli* and purified using ITC as described previously.

3.2.2. Characterization of new ELP_{BC}

The purity of the samples was analyzed using SDS-PAGE; the sample was considered pure when one band at the expected molecular weight was observed. Fusions of BFP were exposed to UV radiation to observe blue fluorescence as an indication of proper folding and function. An UV-Vis spectrophotometer (Cary 300 Bio; Varian Inc.) was used to determine the thermal behavior of the new ELP_{BC} by monitoring the change in absorbance while heating the solution at a rate of 1°C/min. ELP_{BC} compositions whose thermal behavior indicated nanoparticle formation were further analyzed by light scattering.

Temperature controlled DLS as well as simultaneous DLS/SLS measurements were used to determine size and topology of the nanoparticle. Hydrodynamic radii were measured at different temperatures using a temperature controlled dynamic light scattering (DLS) instrument (DynaPro, Wyatt technologies, Santa Barbra, CA). A single detector at 90° measured intensity fluctuations as the temperature was increased in 1°C increments. Three acquisitions each 1 min were recorded at each temperature. The samples were prepared in PBS at 25 μM and 100μL were filtered through Anotop 10 Whatman 20 nm filters directly into a pre-washed cuvette. The autocorrelation curves were fit using a regularization fit.

DLS/SLS measurements were performed using the ALV/CGS-3 goniometer system (ALV, Langen, Germany). Samples for the ALV/CGS-3 goniometer system were

prepared by filtering solutions of the protein ELP_{BC} fusions through an Anotop 10 Whatman 100 nm filter into a 10 mm disposable borosilicate glass tube (Fischer). The tubes were precleaned by washing three times with ethanol filtered through a 0.2 μm cellulose acetate filter. Simultaneous SLS/DLS measurement were obtained for angles between 30°-150° at 5° increments set to 3 acquisitions, each 15 seconds at each angle.

The four proteins chosen previously were fused at the genetic level to the new ELP_{BC} to determine their effect on self-assembly. The proteins were fused to the hydrophilic block's N-terminus. The new sets of protein ELP_{BC} fusions were expressed in BL21(DE3) *E. coli* and purified using ITC as previously described. The purity of the samples was analyzed using SDS-PAGE. The self-assembly of these fusions was also characterized as described above.

3.3 Results and Discussion

3.3.1 Elastin-like polypeptide block copolymer expression and purification

WELP (ELP[A_1:G_1]-80, [W_1:V_4]-80) plasmid was transformed into *E. coli* cells and grown at 37 °C overnight but was found to not express. The lack of expression is hypothesized to be the result of the highly hydrophobic block. However, the six remaining new ELP_{BC} constructs were successfully expressed and purified.

3.3.2 Thermal properties of the new Elastin-like polypeptide block copolymer

The self-assembly behavior of the new ELP_{BC} was first examined by monitoring the change in UV absorbance with increasing temperature. All six new ELP_{BC} compositions show thermal behavior that indicated nanoparticle formation. The absorbance was observed to first increase to an O.D.350 of ~0.05-0.1 indicating the collapse of the hydrophobic block and upon further heating was followed by a sharp increase in O.D. (~1.8-2.4) indicating the collapse of the hydrophilic block and formation of micron-sized aggregates.

First, we examine the three ELP_{BC} with the same hydrophilic ELP block composition of alanine and glycine at a ratio of 1:1and a total length of 80 pentapeptides: LELP, IELP and WELP (Figure 28). LELP has a lower CMT than IELP (22 °C, 26 °C respectively) as predicted from the T_{tc} scale (leucine T_{tc} = 5 °C, isoleucine T_{tc} = 10 °C). WELP has a CMT of 24 °C. The 40 pentapeptide repeats of WELP consist of a total of 32 valine guest residues and 8 tryptophan guest residues while IELP and LELP consist of a total of 40 valine guest residues and 40 isoleucine or leucine guest residues respectively. The shorter yet more hydrophobic block of WELP resulted in a similar CMT as the longer and less hydrophobic blocks of LELP and IELP. No quantitative analysis is drawn for the LELP, IELP, and WELP CMT as the T_{tc} scale provides a qualitative not quantitative scale because when the T_{tc} values were determined the length of ELP chains was not kept constant but rather the total concentration was kept constant at 40 mg/mL.

All three ELP_{BC} have a lower CMT than the hydrophobic block ELP[V] by 7-20 °C (ELP[V] with 120 pentapeptide repeats had a CMT of 33 °C and with 60 pentapeptide repeats had a CMT of 42°C). The CMT of these new ELP_{BC} is ~2 °C higher than the transition temperature of the corresponding hydrophobic ELP monoblock. For example, the T_t of the hydrophobic monoblock of LELP is 20°C while the CMT of LELP is 22°C. The minimal increase in transition temperature upon fusion to the hydrophilic ELP is consistent with the behavior of the previous ELP_{BC} set. The micelle-to-aggregate transition for the three ELP_{BC} occurs at 54°C which is higher than that of the previous hydrophilic block ELP[V_1:A_8:G_7] (49-51 °C). The hydrophilic block is not affected by the composition or length of the hydrophobic block indicating that the increase in local concentration of the hydrophilic block upon micelle formation is more likely to be the factor dictating the micelle-to-aggregate transition temperature. When varying the concentration (Figure 29), the CMT (~6 °C drop) is affected more than the micelle-to-aggregate transition temperature (~ 1.5 °C drop). These new ELP_{BC} compositions have an extended range of micelle-forming temperatures in comparison to the previous ELP_{BC} composition by ~ 17-22 °C.

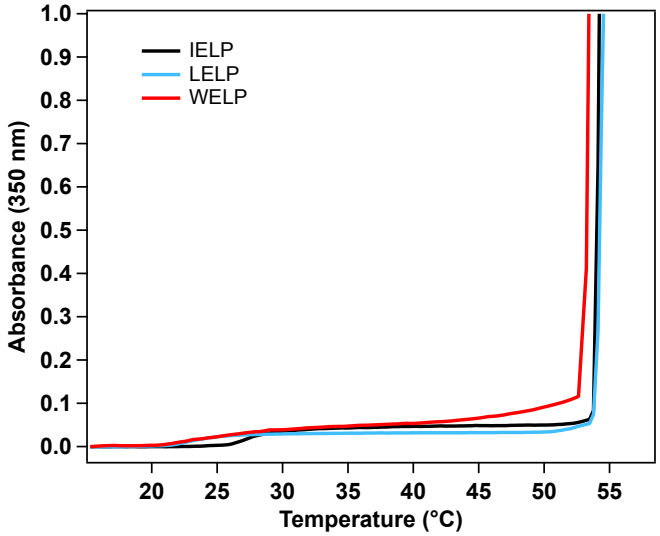

Figure 28: Thermal behavior of new ELP$_{BC}$ with ELP[A$_1$:G$_1$]-80 as hydrophilic block and ELP[V-40,L-40] (LELP), ELP[V-40,I-40] (IELP) or ELP[W$_1$:V$_4$]-40 (WELP) as a hydrophobic block. The absorbance at 350 nm was measured for a sample of 25 µM while heating at a rate of 1°C/min. LELP and WELP have a lower CMT than IELP. All three ELP$_{BC}$ have a similar micelle-to-aggregate transition.

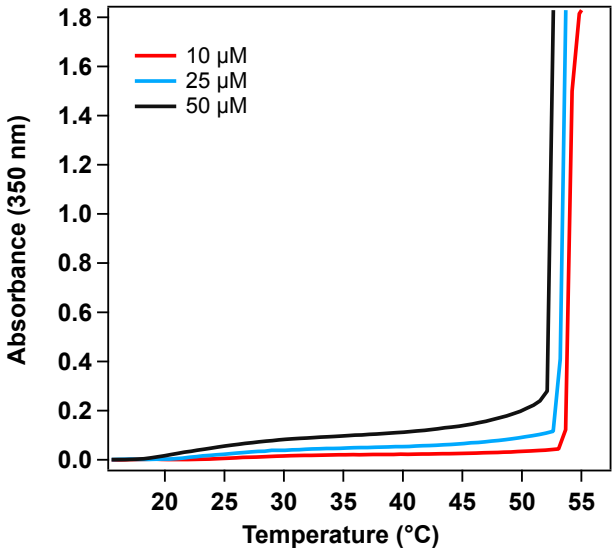

Figure 29: Thermal behavior of WELP at varying concentrations (10, 25, 50 µM).

To create ELP_{BC} with even wider micelle-forming temperature ranges, serine was chosen as the hydrophilic block guest residue. The serine hydrophilic block was fused to three different hydrophobic blocks with compositions and lengths as follows: 1) valine as guest residue and 40 pentapeptides; 2) valine as guest residue and 80 pentapeptides; and 3) valine and tryptophan as guest residues at a ratio of 1:4 and a total of 40 pentapeptides. As can be seen in Figure 30, the three ELP_{BC} showed thermal behavior that indicates self-assembly behavior. Again, the hydrophilic block is not significantly affected by the attached hydrophobic block's composition (ELP[V]-40 versus ELP[W_1:V_4]-40) or length (ELP[V]-40 versus ELP[V]-80). All three ELP_{BC} have micelle-to-aggregate transition temperatures between 72-74 °C. This observation confirms the notion that the micelle-to-aggregate transition depends on the increase in local concentration and is unaffected by the core composition. In addition, the CMT is unaffected by the corona composition as can be observed from the identical CMT (24 °C) of WELP and ELP S-80-W-40 which have the same hydrophobic block composition and length but different hydrophilic blocks. This behavior informs an important design rule for creating new ELP_{BC} as the micelle-forming temperature range can be designed by simply choosing the ELP block composition that gives the desired transition temperature without considering the effect of the other block.

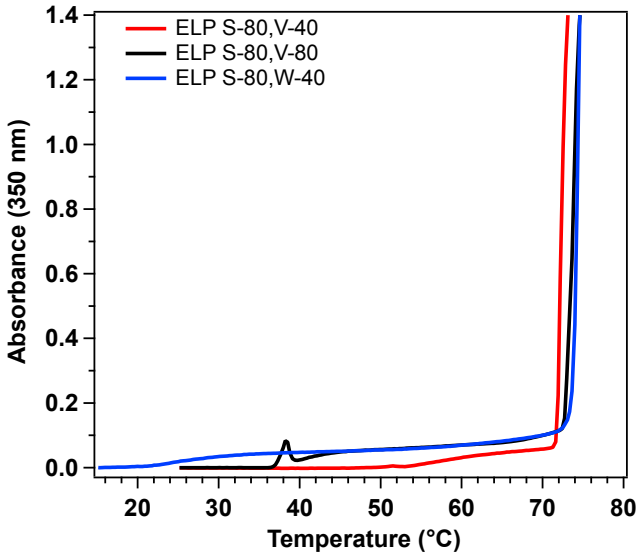

Figure 30: Thermal behavior of new ELP$_{BC}$ with ELP[S]-80 as hydrophilic block and ELP [V]-40, ELP[V]-80 or ELP[W$_1$:V$_4$]-40 as hydrophobic blocks. The absorbance at 350 nm was measured for a sample of 25 μM while heating at a rate of 1°C/min.

Temperature controlled DLS confirms the formation of nanoparticles for all six new ELP$_{BC}$. Figure 31 shows the hydrodynamic radius measured at intervals of 1 °C as well as the change in absorbance with increasing temperature for each of the six ELP$_{BC}$s. Nanoparticles formation was first detected at temperatures that correspond to the initial increase in absorbance. The R_h of the nanoparticles did not significantly increase with an increase in temperature. The R_h of WELP nanoparticles is 24 nm while LELP and IELP nanoparticles have an R_h of 30 nm. The difference in size is due to the shorter total length of WELP (total of 120 pentapeptide repeats) as compared to LELP and IELP (total of 160 pentapeptide repeats). Similarly, ELP S-80,V-40 nanoparticles have an R_h of 25 nm, ELP S-80,W-40 nanoparticles have an R_h of 24 nm, while the larger ELP S-80,V-80 nanoparticle have an R_h of 32 nm. The sizes of the nanoparticles (25 nm versus 32 nm)

again scales with the total pentapeptide length (120 versus 160). The different ELP_{BC} guest residue compositions did not lead to significant difference in overall radii but the size was rather controlled by the total pentapeptide length. The change in R_h with scattering angle for the six ELP_{BC}s was not significant indicating monodisperse spherical nanoparticles (Figure 32; a complete set of light scattering data for the ELP_{BC} can be found in Appendix B). It should be noted that ELP_{BC}s LELP, WELP and ELP S-80,W-40, have a small population (< 5% of total mass) of particles (~50 nm) at temperatures below the CMT. However, this population is not present once micelles are formed.

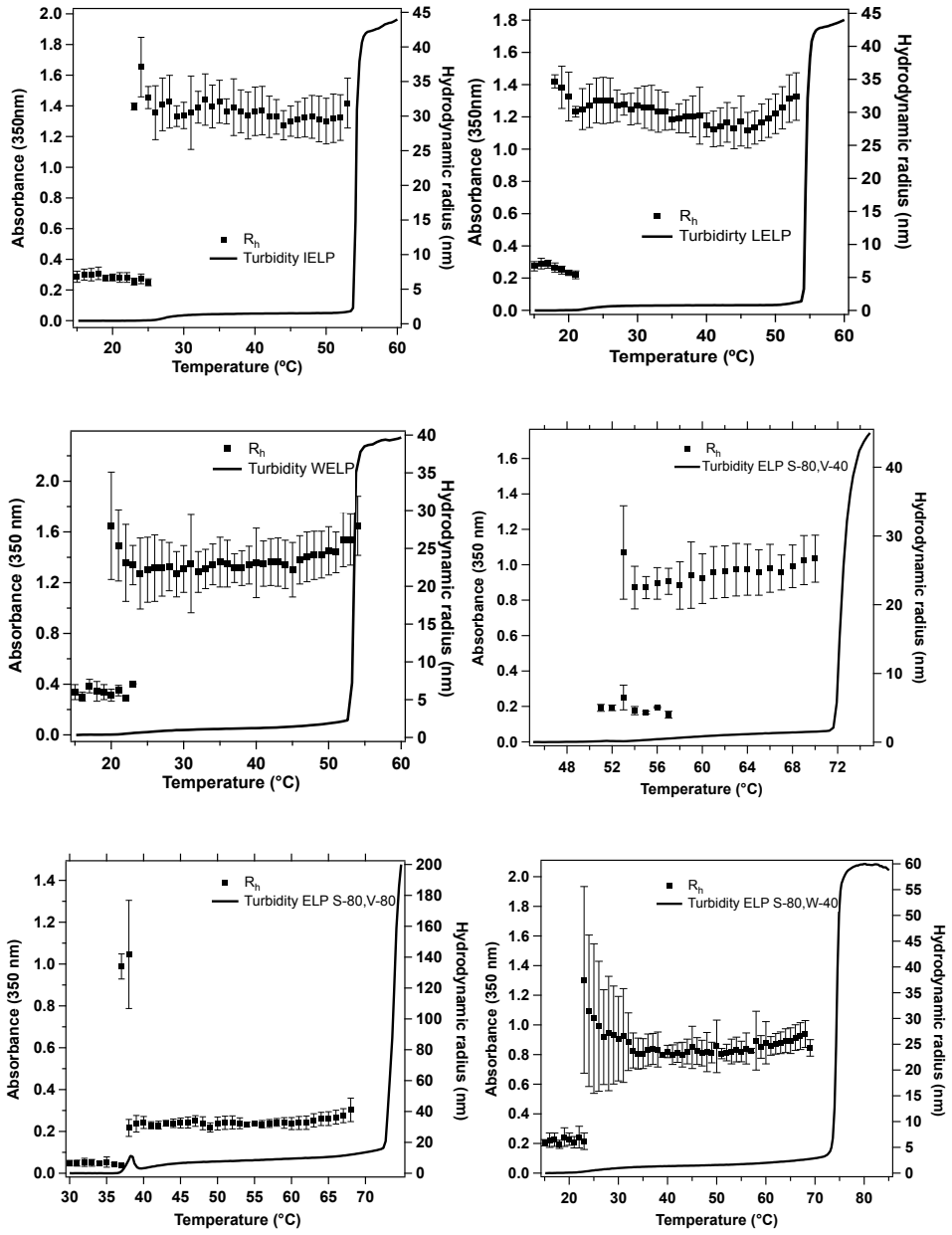

Figure 31: Thermal behavior of new ELP$_{BC}$ as determined by change in absorbance and hydrodynamic radius (R_h) with increasing temperature at 25μM in PBS. The thermal behavior correlates between the two methods. The size of the nanoparticles correlates with the number of total pentapeptides. No significant change in R_h is observed over the micelle-forming temperature range.

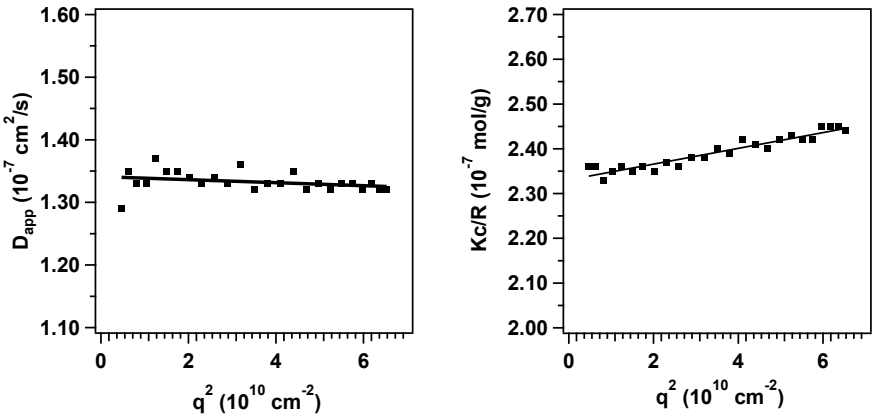

Figure 32: Light scattering of WELP at 35°C in PBS at 1.7 g/L. The left figure shows the change in the apparent diffusion coefficient with change in scattering wavevector as measured by DLS. No angular dependence was observed indicating monodisperse spherical particles. The right figure shows a Zimm plot obtained at a range of angles (30° to 150°) by SLS. The intercept was used to calculate the Mw while the slope was used to calculate R_g. The M_w was found to be 4.3x 10^6 g/mol while R_g was determined to be 15 nm.

Table 5 summarizes the physical characteristics of the nanoparticles. The ρ values indicate a micellar structure; although the theoretical value of ρ for uniform spheres is 0.775, micelles are known to have lower ρ values. However, LELP has an aggregation number of 19 while IELP has an aggregation number of 35. These aggregation numbers are low compared to that of WELP (100 unimers/micelle). An increase in temperature to 45 °C did not increase the aggregation number significantly for LELP (22 unimers/micelle). This difference in aggregation number compared to WELP could be due to the triblock structure of LELP and IELP, which could change the core structure. Of the three ELP_{BC} compositions with ELP[S]-80 as the hydrophilic block, ELP S-80,W-40 shows the largest micelle-forming temperature range of 48 °C which is at minimum an

increase of ~ 37 °C over the previous set of ELP_{BC} (Figure 33). Hence, ELP S-80,W-40 was chosen to be explored further. As indicated in Table 5, the aggregation number is 50 unimers/micelle, which is smaller than that for WELP but higher than LELP and IELP. The ρ value is 0.72 indicating micelle formation.

Table 5: SLS and DLS measurements of new ELP_{BC}

ELP_{BC}	Temp (°C)	R_g (nm)	R_h (nm)	ρ	Aggregation number
IELP	35	18.6	32.6	0.57	35
LELP	35	23.5	32.4	0.72	19
WELP	35	15.7	23.6	0.67	100
ELP S,80-W-40	35	16.4	22.7	0.72	50

One difference is noted between ELP_{BC} with hydrophobic blocks ELP[W_1:V_4] and ELP[V]; while the absorbance for ELP[V] cores continues to increase after the initial increase at the CMT, no additional increase is observed for ELP[W_1:V_4] cores (Figure 33). This difference is attributed to the difference in change in aggregation number with increasing temperature. While ELP[V] cores increase in number of chains significantly (increase > 10 unimers over 1°C), ELP[W_1:V_4] cores, as can be seen in Figure 34, only increase by 25 unimer chains over a 11 °C range (average increase of ~2 unimers over 1°C). This observation indicates that the aggregation number has a week dependence on temperature for ELP[W_1:V_4] cores, which suggests that aggregation number is independent of surface tension of the core.

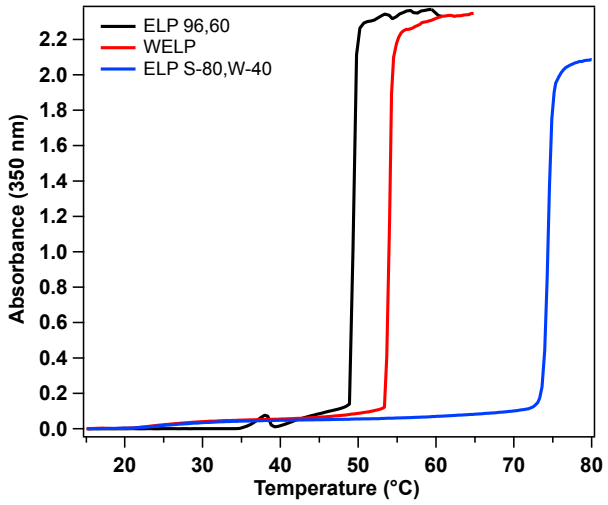

Figure 33: Thermal behavior of ELP$_{BC}$s ELP 96,60, WELP and ELP S-80,W-40. The absorbance at 350 nm was measured for a sample of 25 µM while heating at a rate of 1°C/min. The large increase in micelle forming temperature range can be observed as the block compositions are made more hydrophobic/hydrophilic.

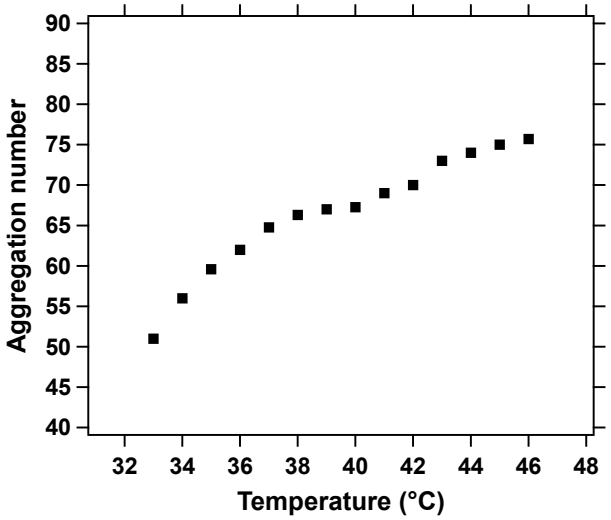

Figure 34: Aggregation number of ELP S-80,W-40 at a range of temperatures as determined by SLS. The aggregation number increases with temperature but not as steeply as previous ELP$_{BC}$ compositions.

3.3.2 Thermal behavior of new protein ELP_{BC} fusions

This section will focus on the behavior of the four proteins when fused to the new ELP_{BC} with the extended micelle-forming temperature range. Specifically, WELP and ELP S-80,W-40 are discussed. For IELP and LELP, briefly, these structures were explored upon fusion to proteins but were found to exhibit behavior similar to the protein WELP fusions indicating that the smaller aggregation number (i.e. less crowding at micelle surface) as well as the difference in architecture (triblock) did not alter the effect of the proteins in self-assembly (Appendix B Figure 71 shows the thermal behavior of protein LELP fusions).

WELP was fused to the four proteins previously described in chapter 2 (BFP, Trx, VHH, and Fn3) to determine their effect on self-assembly. The thermal properties of the fusions indicated whether the protein disrupted self-assembly or retained self-assembly behavior. As seen in Figure 35, it was observed that Fn3 WELP and Trx WELP turbidity profiles indicate self-assemble into nanoparticles. These two proteins had the same effect on self-assembly as with the previous ELP_{BC} composition ($ELP[V_1:A_8:G_7]_n$-$[V]_m$). For VHH WELP, the increase in micelle-forming temperature range did not change its behavior significantly; the transition temperature of the fusion occurs at a temperature that slightly above WELP's CMT. VHH WELP micelles form in a small temperature range (between ~26°C and 29°C) and form 10-30% of the population by mass. However, VHH still depressed the micelle-to-aggregate transition temperature significantly

decreasing it from 54 °C to 30°C. BFP WELP's transition was broad and more complicated as seen in Figure 36. DLS measurements of BFP WELP show populations of unimers, micelles, and aggregates at temperatures above the CMT. Micelles with a radius of 26 nm formed ~ 30% of total mass or more consistently at temperatures higher than 24 °C which corresponds to WELP's CMT. The mass percent of micelles varied between ~30-90% of total mass at different temperatures. However, unimers and aggregates (> 1000 nm) were present at these temperatures for which micelle formation were observed. The aggregates formed at temperatures above the CMT as can be observed from the shape of the autocorrelation functions at different temperatures. However, due to the multiple populations contributing to the measured autocorrelations, fits of size and estimation of mass percentage of each population is approximate. In an attempt to remove the aggregates to see whether these aggregates are a result of nucleation around trace contaminants (similar behavior is observed for protein ELP[V_1:A_8:G_7]$_n$-[V]$_m$ diblocks at specific temperatures) , a BFP WELP sample was incubated and filtered at 37 °C, a temperature at which the aggregates form and should be removed by filtering through a 220 nm filter (simply filtering at room temperature through a 100 nm filter does not yield the same results). As see in Figure 36, upon filtration, the sample's change in absorbance with temperature was found to be similar to that of WELP. However, filtration did not eliminate the presence of aggregates but reduced it. A second increase in absorbance, which usually indicates collapse of the

hydrophilic block, is observed to start at the temperature at which WELP forms aggregates. Yet, a sharp large step increase in absorbance similar to that of WELP is not observed; the transition is broad and only reaches an absorbance of ~0.6-1 indicating that micelles are still present. This complex behavior of BFP WELP is interesting indicating that BFP ELP$_{BC}$ can still self-assemble into nanoparticles but interactions are more complex creating multiple populations.

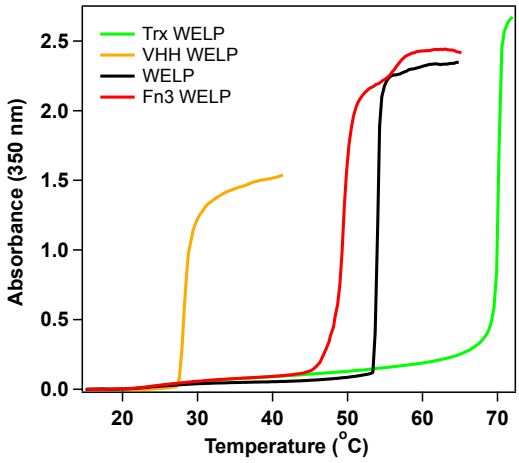

Figure 35: Thermal behavior of protein WELP fusions. The absorbance at 350 was measured for a sample of 25 μM in PBS while heating at a rate of 1°C/min. Fn3 WELP and Trx WELP displayed self-assembly behavior. VHH still disrupted self-assembly behavior of WELP.

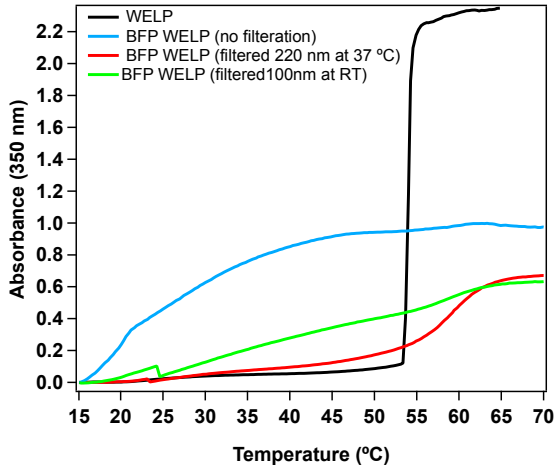

Figure 36: Thermal behavior of BFP WELP with filtration through different pore sizes and at different temperature. BFP WELP forms multiple populations as temperature is increased.

While the extension in the micelle-forming temperature range of WELP altered BFP's effect of self-assembly, the increase in the range was not sufficient to completely alter the behavior of VHH or BFP. Therefore, a larger difference in T_t of the hydrophilic and hydrophobic block was investigated by fusing the four proteins to ELP S-80,W-40. As seen in Figure 37, the increased ELP_{BC} hydrophobicity/hydrophilicty of the blocks did not change the effect of the proteins. Trx ELP S-80,W-40 and Fn3 ELP S-80,W-40 still self-assembled into nanoparticles. VHH depressed the micelle-to-aggregate transition temperature of ELP S-80,W-40 significantly from 72 °C to 30 °C. VHH ELP S-80,W-40 are observed between 21 °C and 26°C. BFP ELP S-80,W-40 behaved similarly to BFP WELP (Figure 38) displaying a complex behavior in which the change in absorbance with temperature was not similar to that of ELP S-80,W-40 suggesting a population of

micelles as well as aggregates were present. In addition, no large sharp increase indicating the collapse of the hydrophilic block is observed for the BFP fusion

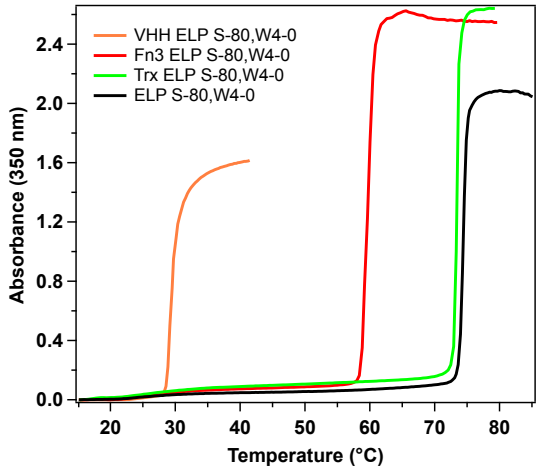

Figure 37: Thermal behavior of protein ELP S-80,W-40 fusions. Trx ELP S-80,W-40 and Fn3 ELP S-80,W-40 display behavior similar to ELP S-80,W-40, while VHH ELP S-80,W-40 significantly decreased the micelle-to-aggregate transition.

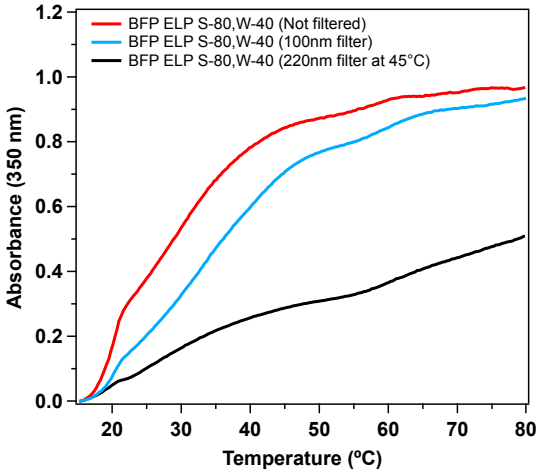

Figure 38: Thermal behavior of BFP ELP S-80,W-40. The sample is filtered at multiple temperatures and filter pore sizes to examine the more complex behavior of BFP ELP S-80,W-40.

As seen in Figure 39 and Figure 40, fusion to Fn3 and Trx affect the micelle-to-aggregate transition temperature but did not change the CMT as seen previously. Fn3 lowered the second transition temperature compared to free WELP and free ELP S-80,W-40. Trx increased the second transition temperature of WELP but did not affect that of ELP S-80,W-40. This effect is unexpected and suggests that there is perhaps a limit to the effect of proteins on the T_t of an ELP segment whether due to matching of hydrophilicity of the protein and the hydrophilic block or protein unfolding. In the case of the clinically relevant Fn3, these new ELP$_{BC}$ compositions have the advantage of extending the micelle-forming temperature range and the aggregation number is stabilized which improve upon the existing libraries of ELP$_{BC}$s drug delivery vehicles.

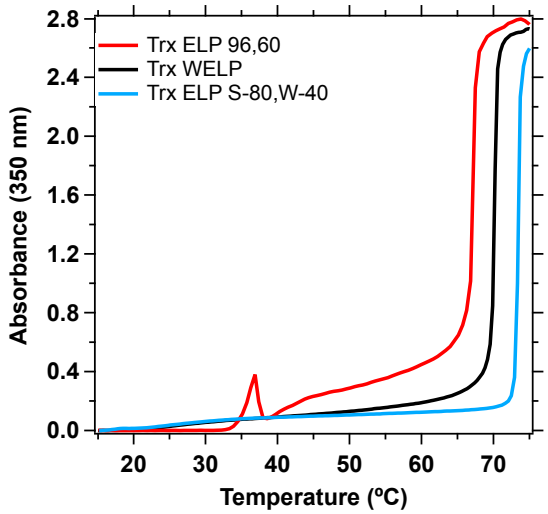

Figure 39: Thermal behavior of Trx ELP$_{BC}$ fusions with increasing hydrophilicity/hydrophobicity of ELP$_{BC}$ blocks.

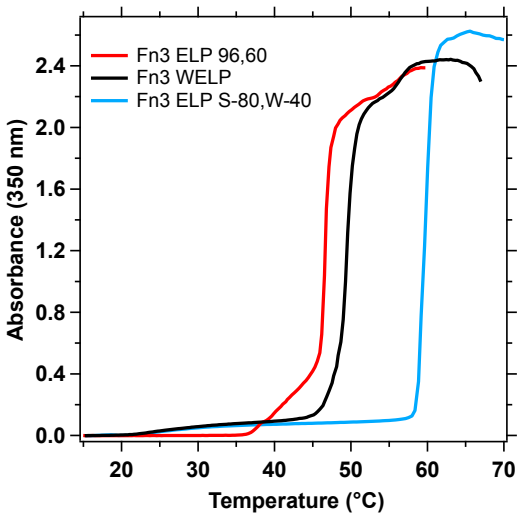

Figure 40: Thermal behavior of Fn3 ELP$_{BC}$ fusions with increasing hydrophilicity/hydrophobicity of ELP$_{BC}$ blocks.

In examining the behavior of protein ELP$_{BC}$, one factor that we sought to examine was the composition of the ELP blocks. In increasing the difference between the guest residue compositions of the two blocks, first by using serine, the most hydrophilic residue within the non-charged amino acids, as the guest residue for the hydrophilic block and second by incorporating tryptophan into the valine hydrophobic block, a 48 °C micelle-forming temperature range is obtained as compared to the previous 12 °C temperature range. Although BFP behavior was altered by the change in the hydrophilicity/hydrophobicity of the blocks, VHH and BFP's self-assembly behavior did not match that of Fn3 and Trx suggesting that their effect is not as simple as solely depressing the micelle-to-aggregate transition temperature till one transition is observed. A change in diblock composition was not successful in entirely altering the effect of the protein on self-assembly which suggests that the protein fused to the ELP$_{BC}$

dominates the forces directing self-assembly through its interaction with both blocks. Trx and Fn3's effect on the micelle-to-aggregate transition temperature indicates an interaction with the hydrophilic block while the implication of this study is that VHH and BFP do not interact solely with the ELP block to which they are directly fused (i.e. the hydrophilic block) but also with the hydrophobic block. As such, merely controlling the diblock composition might not be sufficient for a subpopulation of proteins to retain self-assembly behavior of the ELP_{BC}.

3.4 Conclusions

In this chapter, we examined the effect of the ELP_{BC} composition on protein ELP_{BC} self-assembly. In creating six new ELP_{BC} with varying compositions a wide set of micelle-forming temperatures ranges are achieved. In examining the thermal behavior of the diblock, one design rule was deduced: the CMT and the micelle-to-aggregate transition temperature of the ELP_{BC} are unaffected by composition and length of the hydrophilic and hydrophobic block respectively. The micelle-to-aggregate transition temperature is perhaps determined more so by the critical temperature of its monoblock's phase diagram. Therefore, if a block's transition temperature when part of an ELP_{BC} is known, it can be expected to behave similarly within any other ELP_{BC}.

Through using serine and tryptophan as guest residues, the micelle-forming temperature range was significantly extended (from ~12 to ~48 °C). In addition, it was found that ELP cores with tryptophan did not change aggregation number significantly

with increasing temperature. However, the effect of the protein on self-assembly was similar to that previously observed. Trx and Fn3 ELP_{BC} self-assembled while VHH significantly depressed the micelle-to-aggregate transition temperature (micelles were observed over a small range of a few degrees). BFP was the exception in that upon the collapse of the hydrophobic block two populations of micelles and aggregates formed. The protein interactions seem to dominate the forces that govern ELP_{BC} self-assembly. From Trx and Fn3, we can see that the hydrophilic block is affected by the proteins while the hydrophobic block is unaffected. While VHH and BFP indicate that interaction with the hydrophobic block particularly upon its collapse is a dominant interaction. From the behavior of these four proteins, we can conclude that perhaps the protein's interaction with one or both of the blocks dominates the forces driving self-assembly. If the protein has a strong interaction with the hydrophobic block, the self-assembly is more likely to be disrupted.

4. Theoretical understanding of Elastin-like polypeptide diblock self-assembly behavior

4.1 Introduction

Self-assembly of a polymeric diblock is driven by the preferential solvation of one block over the other. One block's monomers prefer to interact with each other as compared to the solvent (i.e. the block is in poor solvent) resulting in its collapse. Therefore, this block prefers to associate with other chains to reduce surface tension and forms the core of a micelle. The other block remains solvated as the corona. Models have been developed to describe the self-assembly of synthetic polymer diblocks[85-87]. Theoretical predictions of micelle properties such as radius and aggregation number from these models were found to be in good agreement with experimental data. However, it has yet to be determined whether the self-assembly of elastin-like polypeptides, and polypeptides generally as a class, can be described as well by this theory. As such, we sought to determine whether the theory of synthetic polymers is applicable to ELP diblocks self-assembly.

The balance of three energetic contributions determines the self-assembly behavior of the diblock: the free energy of the corona, interface and core. The corona energy is determined by the balance of monomer-monomer interactions and the elastic energy resulting from the stretching due to monomer-monomer repulsion. The monomer-monomer interaction is determined by solvent quality (two-body interaction (good solvent) and three-body interaction (theta solvent)). The interface energy arises

from the interaction of the hydrophobic monomers with the solvent present at the core/corona interface. The core energy is determined by the monomer-monomer attraction and the elastic energy due to stretching of the core block. As the monomer-monomer interaction within a single collapsed unimer is the same as within the core of a micelle, this energetic contribution is omitted from further consideration.

Changes in lengths of the two blocks leads to changes in the self-assembled structure's morphology from spherical to cylindrical and from cylindrical to lamellar as the total energy of one morphology becomes preferable (lower) than the other (Figure 41). Typically in determining physical properties such as aggregation number and radius, the two dominant energies, corona energy and interface energy, are considered. However, while the elastic energy of the core plays a smaller role, it determines the transition between the various morphologies: spherical to cylindrical to lamellar.

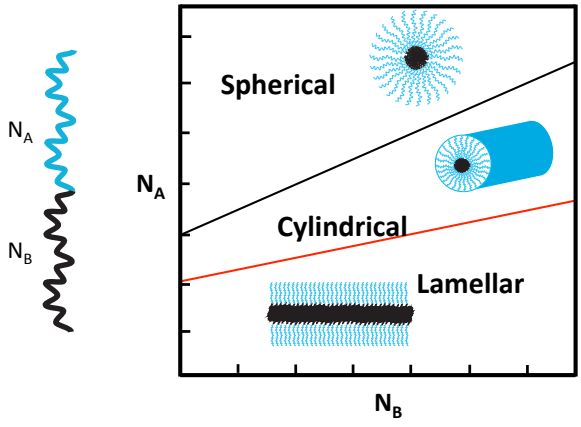

Figure 41: Schematic of morphological changes between spherical, cylindrical and lamellar for diblocks of hydrophilic A block and hydrophobic B block. Larger N_A values prefer spherical morphologies while increasingly smaller N_A drive transitions to cylindrical and lamellar morphologies.

Coronas always prefer spherical geometries as this morphology has the greatest curvature and thus affords the most volume for the hydrophilic chain. Therefore, diblocks with large hydrophilic blocks form star-like micelles in which the size of the corona is larger than the core. However, as the hydrophilic chain becomes shorter, the preference weakens and the core preference of being in cylindrical or lamellar becomes important. The transition between spherical to cylindrical and cylindrical to lamellar occur when the micelles are within the regime of crew-cut micelles. This regime is defined by a core size that is larger than the corona thickness. The corona in this regime can be approximated to be a planar brush. The values of N_A and N_B at which the spherical-to-cylindrical and cylindrical-to-lamellar transitions occur are determined as the points at which sum of the three free energy components for the two morphologies are equal.

A previous study applied a model describing the self-assembly of synthetic polymers to a polystyrene-polyisoprene (PS-PI) diblock in heptane using experimentally determined parameter for this system[85]. These diblocks has been experimentally shown to form spheres, cylinders and lamella depending on the degree of polymerization of each block. The theoretical predications were found to be in good agreement with experimentally determined values of radius and aggregation numbers. The model could also predict the boundaries between the morphologies accurately. Therefore, we will use this model to predict the properties of ELP diblock.

To apply the model to the ELP system, two parameters must be determined experimentally: the solvent quality of the hydrophilic block and the surface tension of the hydrophobic block. The solvent quality will determine whether two-body or three-body dominate the interactions in the corona. The solvent quality can be determined by measuring the second virial coefficient using static light scattering. The surface tension can be calculated from equating the chemical potential of a globule to that of sediment in a two-phase solution. This derivation gives a relationship between surface tension, concentration and block length. The surface tension is then related to temperature by determining the relation between concentration and cloud point.

The exciting and new aspect of studying ELPs is that while they are LCST polymers, they are also polypeptides. As such, there are two properties that differentiate them from synthetic polymers that warrant consideration: 1) the change in composition between the hydrophilic and hydrophobic block is not as distinct as with synthetic polymers. The hydrophobic block shares the same structure of the four repeating amino acids (VPGXG) within the pentapeptide unit. The ELP diblocks chosen for this study are the ELP_{BC} previously described in chapter 2. For this set of ELP_{BC}, the hydrophilic block guest residue composition is valine, alanine, and glycine at a ratio of 1:8:7 ($ELP[V_1:A_8:G_7]$) while the hydrophobic block guest residue composition is valine (ELP[V]). This ELP_{BC} set was chosen in part as it is the most characterized set but in addition this set spans a range of the N_A and N_B space for the same compositions of

block A and block B. For this set, the hydrophobic and hydrophilic blocks also share a guest residue, valine, that is present in different percentages in the two blocks. 2) ELPs are known to increase in β-turns as they undergo the phase transition[15], which could add another energetic component to the free energy as well as result in a change in the stiffness of the chain with increasing temperature for both blocks. In addition, the morphology phase boundaries shift with changes in temperature as the free energies of the micelles are temperature dependent and therefore, we examine the boundaries and the physical properties as they change with temperature.

4.2 Defining a monomer for elastin-like polypeptides

In considering an ELP chain, we would like to define a symmetrical monomer for the hydrophilic block A, a_A, and hydrophobic block B, a_B, which is repeated N_A and N_B times respectively. To accomplish this, we consider a pentapeptide repeat with the guest residue valine. This pentapeptide has a molecular weight of 427 g/mol and contour length (L) of 1.82 nm (each amino acid is assumed to have an average length of 0.365 nm as estimated from known peptide bonds[23]). With a density (ρ) of approximately 1 g/cm^3 (close to water density), the size of the monomer can be calculated as follows:

$$a = \sqrt{\frac{M}{\rho N_{AV} L}}$$

where N_{AV} is Avogadro's number. This equation yields a value of 0.63 nm for the monomer size. The hydrophilic block is composed of guest residues valine, alanine and glycine. The variation in composition to glycine and alanine changes the molecular

weight to 385 or 400 g/mol, which results in a monomer size of 0.60 or 0.61 nm, respectively. The change is relatively small and the value of the monomer size of the pentapeptide with valine as guest residue was used. The monomer size of the block A and block B were assumed to be equal ($a_A = a_B$).

4.3 Determining surface tension

To derive an expression for surface tension, we equate the chemical potential (μ) of a globule and sediment of the hydrophobic ELP monoblock in a two-phase solution. The globule chemical potential is composed of the sum of its entropy, surface energy and interaction energy. The sediment chemical potential is composed of the sum of its interaction energy and entropy. The interaction energy in the globule and sediment are assumed to be equal as they only depend on the monomers in consideration. As derived below, equating the two terms and rearranging, we get an expression for surface tension per area unit ($\tilde{\gamma}$) in terms of globule volume fraction in solution (ϕ′).

$$\mu_{globule} = \mu_{sediment}$$

$$kT\ln(\phi') + 4\pi R^2_{globule}\tilde{\gamma} = kT\ln(\phi'')$$

$$\tilde{\gamma} = \frac{kT}{4\pi R_{globule}{}^2}\ln\left(\frac{\phi''}{\phi'}\right)$$

where $R_{globule}$ is the radius of globules and ϕ′′ is the volume fraction of the sediment. We ignore the contribution of the sediment entropy ($kT\ln(\phi'')$) as the sediment volume fraction is assumed to be much larger than that of the globules and thus the entropy is negligible. We can express $R_{globule}$ in terms of the globule molecular weight and volume

fraction inside the globule (ϕ'') (the volume fraction of the polymer inside the globule is assumed to be the same as the sediment's volume fraction) as follows:

$$R_{globule} = (\frac{3}{4\pi}\frac{M_{aa}.N_B}{\rho.\phi''}\frac{1}{N_{av}})^{\frac{1}{3}}$$

where ρ is the density within the globule, M_{aa} is the average molecular weight of the amino acids. Substituting back into the equation for surface tension, we obtain an expression for surface tension in terms of the two variables globule volume fraction and degree of polymerization as follows:

$$\frac{\tilde{\gamma}}{\phi''^{\frac{2}{3}}} = \frac{kT}{4\pi(\frac{3}{4\pi}\frac{M_{aa}}{\rho N_{av}})^{\frac{2}{3}}}\left[\frac{1}{N_B}\right]^{\frac{2}{3}}\ln(\frac{1}{\phi'})$$

A dependence of ϕ' on temperature can be experimentally determined for each of the three hydrophobic block lengths by determining the binodal curve for each length. By measuring the change in absorbance of the hydrophobic ELP[V] monoblock with increasing temperature, the temperature at which the phase separation occurs at a given concentration can be determined by finding the temperature at which the tangent through the steepest part of the absorbance curve intercepts the temperature x-axis. As shown in Figure 42, the T_t is determined for all three hydrophobic block lengths (60, 90 and 120 pentapeptides) at range of concentrations between 0.002 and 2 g/L. Experimental details are discussed in Appendix C. At these concentrations, the range of the measured T_t encompasses the CMT range meaning that the surface tension is measured within the range of temperatures relevant to micellization.

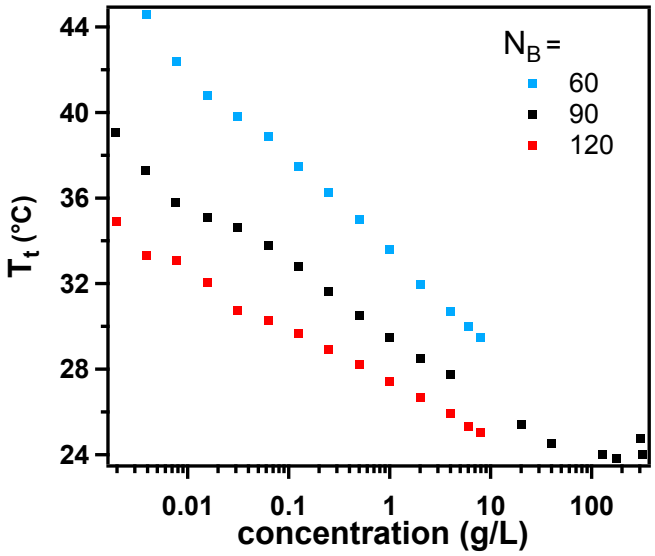

Figure 42: Transition temperatures of hydrophobic ELP[V] monoblock versus concentration for pentapeptide lengths 60, 90 and 120. The absorbance was measured at 350 nm while the temperature was increased at a rate of 1°C/min. The transition temperature is defined as the temperature at which the tangent through the steepest part of the absorbance curve intercepts the x-axis.

To find an expression for surface tension, we express concentration as $\frac{1}{N_B^{\frac{2}{3}}}\ln(\frac{1}{\phi'})$.

The normalization of the concentration by the degree of polymerization (N_B) collapses all three curves in Figure 42 onto one line (Figure 43). By obtaining the linear fit of this plot, we now can express surface tension as a linear equation of temperature as follows:

$$\frac{\tilde{\gamma}}{\phi'^{\frac{2}{3}}} = \frac{kT}{nm^2}(0.00733\times T - 2.13)$$

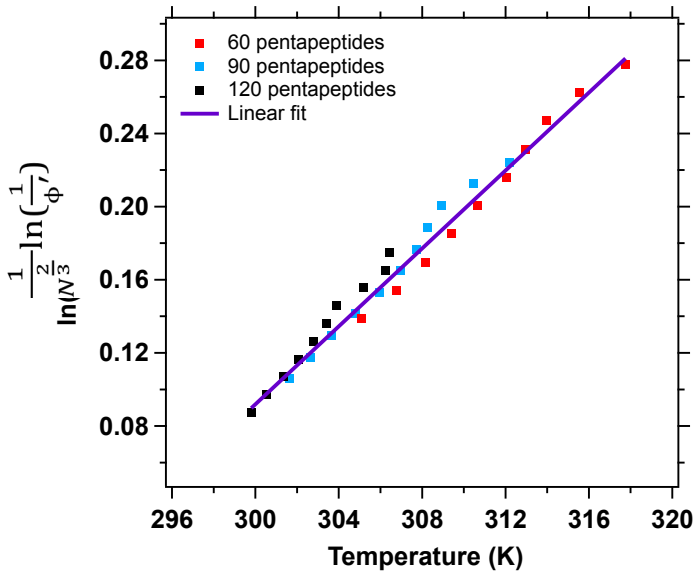

Figure 43: Determining relationship between temperature and concentration for surface tension of hydrophobic block calculations. The Log of inverse volume fraction of ELP normalized by $N_B^{2/3}$ is plotted against the measured transition temperature. Three hydrophobic ELP monoblock lengths collapse onto one curve and a single linear fit (purple line) relates the concentration term to the transition temperature.

4.4 Determining solvent quality of the hydrophilic block

In determining the expression for the interaction energy of the corona, the solvent quality will dictate whether the two-body or three body interactions are dominant. The solvent quality is determined from the excluded volume, which is a measure of monomer-monomer interaction. Experimentally, the second virial coefficient can be measured using static light scattering and can then be used to calculate the excluded volume. By constructing a Zimm plot through measuring averaged intensity over a range of scattering angles and solution concentrations, the second virial coefficient can be determined.

The hydrophilic ELP monoblock (ELP[V_1:A_8:G_7]-96) was expressed and used to measure the second virial coefficient (A_2). The dn/dc, the change in refractive index with concentration, was measured at each temperature and is listed in Table 6. The dn/dc is part of the optical constant (K) as shown in the scattering equation below.

$$\frac{Kc}{R_\theta} = \frac{1}{M_w P(q)} + 2A_2 c$$

where R_θ is the Raleigh ratio, P(q) is the form factor, K is an optical constant, and c is concentration in g/mL. When extrapolated to scattering angle zero, the form factor becomes P(0)=1 and thus the equation can be written as:

$$\frac{Kc}{R_0} = \frac{1}{M_w P(0)} + 2A_2 c = \frac{1}{M_w} + 2A_2 c$$

The samples were measured at temperatures 23, 30, 35, 40 and 45 °C. As shown in Figure 44, a Zimm plot is constructed and A_2 is found from the slope of the linear fit of Kc/R extrapolated to scattering angle zero versus concentration (equation below). Zimm plots at higher temperatures are shown in Appendix C.

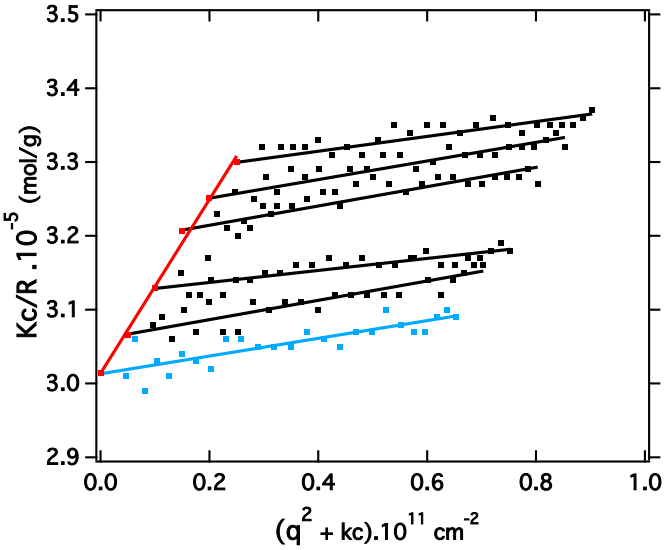

Figure 44: Zimm plot of ELP[V_1:A_8:G_7]-96 at 23 °C. A_2 is obtained from slope of linear fit of Kc/R_0 versus q^2 (red line). The blue line is the extrapolation to concentration = 0. The y-intercept is the weight average molecular weight. The arbitrary constant, k, used for this Zimm plot is 50.

Figure 45 shows the change in A_2 with temperature. As expected, A_2 decreases with temperature and becomes negative between 40-45 °C (shaded area). The change in interaction from repulsion to attraction as indicated by the change in A_2 from positive to negative indicates that the theta-temperature is between 40-45 °C. From A_2, the excluded volume can be calculated.

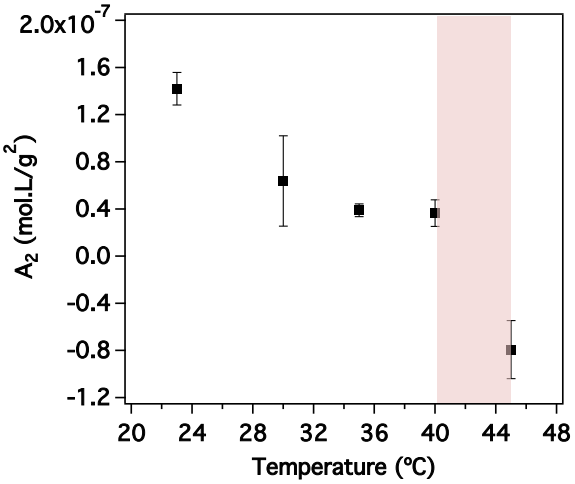

Figure 45: Change in A_2 of ELP[V_1:A_8:G_7]-96 with increasing temperature as determined from Zimm plots. A change from repulsion to attraction between monomers occurs between 40-45 °C (i.e. theta-temperature is between 40-45 °C).

The excluded volume (ν) can be calculated from A_2 using the following equation:

$$\nu = \frac{2A_2M_o^2}{a_A^3N_{AV}}$$

where M_o is the mass of one a_A monomer. This equation is valid for temperatures close to the theta temperature. The solvent quality is determined by calculating at which scale the magnitude of two-body interactions becomes significant (i.e. larger than thermal energy, kT) to cause swelling (i.e. on a scale larger than the thermal blob). The corona can be thought of as correlation blobs which are non-overlapping blobs in the normal direction from the interface surface. The interaction energy of a correlation blob is on the order of kT. The correlation blob size increases as you move radially away from the core. If the thermal blob is larger than the largest correlation blob within the corona brush,

then the corona is in theta solvent (Figure 46). The excluded volume can be used to calculate the size of the thermal blob (ξ_t) as follows:

$$\xi_t = a_A p_A^2 \nu^{-1}$$

where a_A = 0.63 nm and p_A is the ratio of the Kuhn length to the monomer size and is calculated to be 3.5 as based on ELP Kuhn length of 2.2 nm as measured by Schmidt and coworkers[23].

Table 6 shows the values of A_2, ν, and ξ_t at different temperatures. The size of the thermal blob in all cases is greater than the radius of the micelles (~30-40 nm) (Figure 46). This comparison then indicates that the corona is in theta-solvent at all temperatures studied and three-body interactions dominate the interaction energy of the corona.

Table 6: Determining solvent quality of corona from measured monomer-monomer interaction

Temperature (°C)	dn/dc (mL/g)	A_2 (mol.L/g$_2$)	ν	M_W (kDa)	ξ_t (nm)
23	0.160	1.42E-07	0.114	39	68
30	0.160	6.39E-08	0.0511	37	151
35	0.159	3.89E-08	0.0311	39	248
40	0.158	3.65E-08	0.0292	39	264
45	0.156	-9.06E-08	-0.0725	40	106

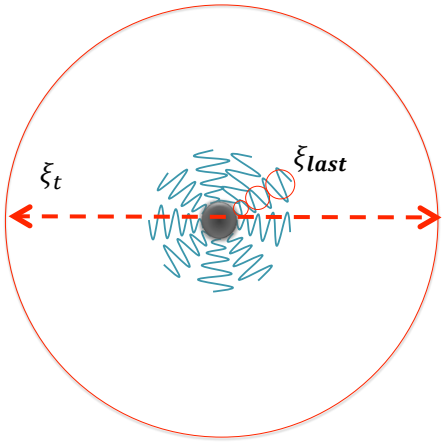

Figure 46: Scale of thermal blob at 30 °C in relation to spherical micelle (~30 nm radius). ξ_{last} is the largest correlation blob size within the corona.

4.5 Model of diblock self-assembly

We consider, herein, a micelle with a hydrophilic block A with N_A monomers for which the solvent is a theta solvent, and a hydrophobic block B with N_B monomers for which the solvent is a poor solvent. The expression of total free energy for a given micelle morphology (j) is the sum of three energies: corona, interface free energy, and core.

$$F_j = F_{j,coreelastic} + F_{j,interface} + F_{j,corona}$$

where j =1 for lamella, j =2 for cylinders, and j =3 for spheres. The interface free energy per chain is related to the surface area per chain (s) and the surface tension per area of monomer (γ):

$$F_{j,interface} = kT\gamma \frac{s}{a_B^2}$$

For a spherical morphology (j =3), the surface free energy expression is as follows:

$$F_{3,interface} = kT \frac{3\gamma a_B N_B}{\phi_B R_{3,core}}$$

The elastic energy of the core is related to the stretching of the hydrophobic block. The elastic energy is related to the ratio of the core radius to the Gaussian end-to-end distance of the hydrophobic chain as follows:

$$F_{j,coreelastic} = kT(k_j \frac{R_{j,core}^2}{R_G^2}) = kT\ (k_j \frac{R_{j,core}^2}{a_B^2 N_B p_B})$$

where k_j is a numerical coefficient dependent on morphology, R_G is the Gaussian end-to-end distance, p_B is the ratio of Kuhn length to monomer size, and $R_{j,core}$ is the core radius. For lamella, j =1 and $k_1 = \pi^2/8$; for cylindrical micelles, j=2 and $k_2 = \pi^2/16$; for spherical micelles, j=3 and $k_3 = 3\ \pi^2/80$.

The corona energy is dependent on the micelle morphology as the hydrophilic chains can be considered brushes tethered to the surface of the micelle core. In lamellar morphology, the corona is a planar brush. For a planar brush, the corona energy is the sum of elastic and three-body interaction energy as follows:

$$F_{1,corona} = F_{corona,elastic} + F_{corona,\ interaction}$$

$$F_{1,corona} = \frac{3}{2} kT \frac{H_1^2}{a_A^2 N_A p_A} + kT \frac{\omega a_A^6 N_A^3}{s^2 H_1^2}$$

where H_1 is the thickness of the corona brush in the lamellar morphology, s is the surface area per chain. For spherical and cylindrical morphologies, the corona free energy expression above is adjusted for the increase in surface area per chain radially. The expression for the total free energy for a spherical micelle (F_3) is as follows:

$$\frac{F_3}{kT} = kT\gamma \frac{jN_B a_B}{\phi_B R_{3,core}} + \frac{3\pi^2 R_{3,core}^2}{80 a_B^2 N_B p_B} + \frac{1}{2\sqrt{3}} C_F p_A^{-3/4} \frac{R_{3,core}^{3/2} \phi_B{}^{1/2}}{N_B^{1/2} a_B^{3/2}} ln \left[1 + \frac{2C_H p_A^{1/4} N_A \phi_B{}^{1/2} a_A^2}{\sqrt{3} R_{3,core}^{1/2} N_B^{1/2} a_B^{3/2}}\right]$$

where C_F and C_H are numerical coefficients. The free energy minimum is determined by taking the derivative of F_3 with respect to core radius ($R_{3,core}$) which results in a nonlinear equation that determines $R_{3,core}$ ($\frac{\partial F_3}{\partial R_{3,core}} = 0$). The nonlinear equation can be solved numerically. Upon determining the radius of the core, H_3, R_{total} and aggregation number (Q) as well as the phase boundaries between morphologies can be calculated. For spherical micelles, the expression for the these properties are as follows:

$$R_{total} = H_3 + R_3$$

$$H_3 = R_3 \left[\left(1 + \frac{2C_H p_A^{1/4} N_A \phi_B{}^{1/2} a_A^2}{\sqrt{3} R_{3,core}^{1/2} N_B^{1/2} a_B^{3/2}} \right)^{\frac{1}{2}} - 1 \right]$$

$$Q = \frac{4\pi \phi_B R_3^3}{3 N_B a_B^3}$$

4.6 Comparison of experimental and theoretical predictions

To validate the model, the physical properties of spherical micelles predicted by the model were compared to experimental data. First, we compared theoretical and experimental values at one temperature, 43°C. R_h and Q for all six ELP_{BC} were determined experimentally by DLS and SLS respectively (Table 7) at a concentration of 25 μM. Experimental details are described in appendix C. The morphologies for four ELP_{BC} were determined, by DLS/SLS and cryo-TEM, to be spherical. These spherical micelles are thermodynamically stable as discussed in appendix C. However, two ELP_{BC} (ELP 64,90 and ELP 64,120) are composed of two populations at 43 °C, spherical and larger particles (100-200 nm). Cryo-TEM imaging suggested that these larger particles

are clusters of the spherical micelles rather than distinct morphologies such as cylindrical micelles. However, at this time, we cannot conclude whether or not these morphologies were not observed due to the method of preparation of the sample.

Table 7: Morphology and physical properties of ELP_{BC} as experimentally determined at 43°C and 25 μM.

ELP_{BC}	Hydrophilic	Hydrophobic	Morphology at 43 °C	Q	R_h (nm)
ELP 64,60	64	60	Spherical	125	24
ELP 96,60	96	60	Spherical	96	27.4
ELP 128,60	128	60	Spherical	83	28.9
ELP 96,90	96	90	Spherical	183	31.4
ELP 64,90	64	90	Spherical + nanoscale aggregates	N/A	~100
ELP 64,120	64	120	Spherical + nanoscale aggregates	N/A	~90

ELP micelle cores are assumed to be dense cores based on the previously determined phase diagrams of temperature and composition. From this assumption, it follows that then the concentration of the core is uncoupled from the surface tension of the core[21]. To fit the model, a core volume fraction (ϕ_B) of 0.6 was estimated from Urry and coworkers' previous work[21, 22]. The numerical coefficients, C_F and C_H, that arise during the derivation of the corona free energy were determined by finding values of these coefficients for which predicted Q and R_h of ELP 128,60 simultaneously match the experimental values. The predicted total radius must be larger than the hydrodynamic radius. In addition, the coefficient values must meet certain conditions that the derivation of C_H and C_F sets: 1) $C_F > C_H$, 2) $0.5 \leq C_H \leq 1$ and 3) $C_F \geq 1$. The change in

predicted Q and R_h of ELP 128,60 with change in C_F is plotted for several C_H values (Figure 47). A value of 1 for C_H is the only value that yields a total radius larger than the hydrodynamic radius. For C_H =1, the C_F value that predicted Q correctly is 1.4. As such, the values of C_F and C_H were chosen to be 1.4 and 1 respectively and used to predict the total radius and aggregation number of the remaining ELP_{BC}s.

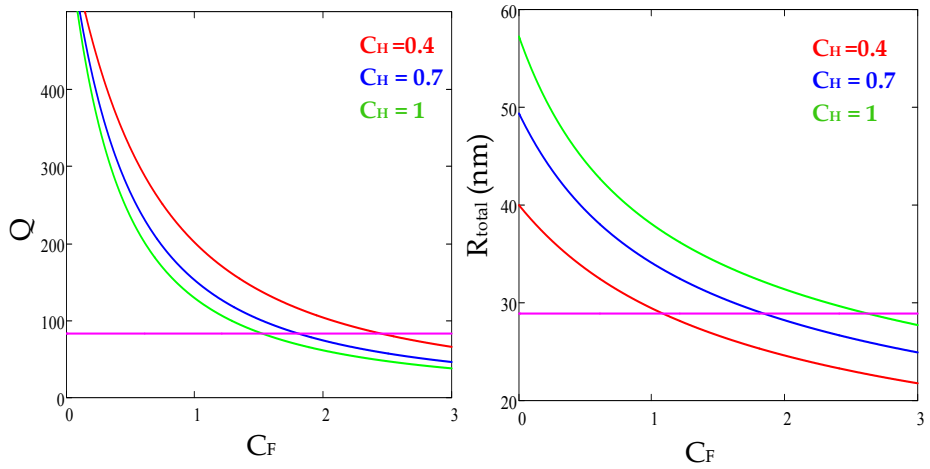

Figure 47: Predicted aggregation number (left) and total radius (right) of spherical micelles at different numerical coefficients, C_F and C_H, for ELP 128,60 at 43°C. The pink horizontal line in each plot represents the experimentally determined aggregation number and hydrodynamic radius of ELP 128,60 at 43°C.

The model qualitatively predicts trends of Q and R_h as well as their power law dependence for micelle parameters. The radius of the micelle increased with increasing N_A and increasing N_B (Figure 48) as expected. Q decreased with increasing N_A since larger hydrophilic chains occupy larger volumes within the corona and thus a smaller number of chains pack in the corona (Figure 49). For a hydrophobic block length of 60 pentapeptides, increasing N_A from 64 to 96 to 128 pentapeptides decreased Q from 125 to 96 to 83 respectively. Q increased with increasing N_B in order to reduce the surface

area per chain at the core/corona interface upon the increase in core volume caused by the larger hydrophobic blocks. This trend is observed when N_B was increased from 60 to 90 pentapeptides; ELP 96,60 has an aggregation number of 96 while ELP 96,90 has an aggregation number of 183.

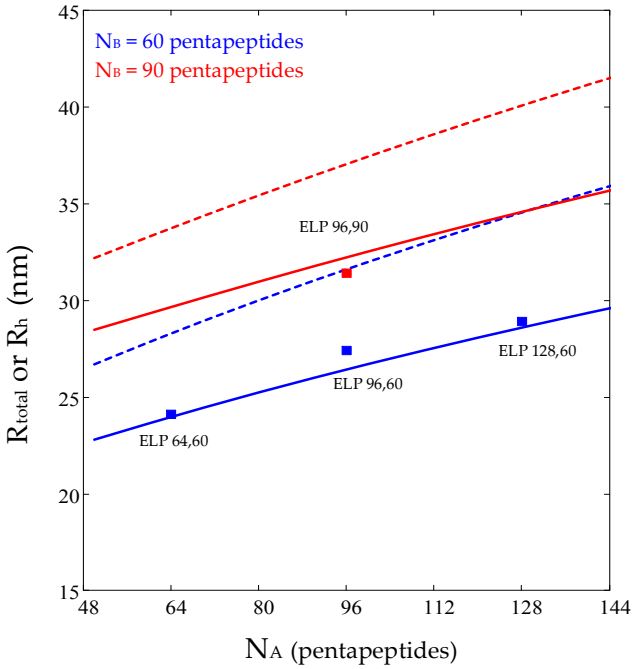

Figure 48: Change in total radius and hydrodynamic radius of spherical micelles with increasing N_A. The solid lines represent the theoretical predication of hydrodynamic radii. The dashed lines represent the predicted total radii (exact numerical solution). The dots indicate the experimentally measured hydrodynamic radii at 43 °C. A constant (C) of 0.85 was used to predict micelle hydrodynamic radius. The blue lines and dots represent ELP_{BC} with a hydrophobic block length of 60 pentapeptides. The red lines and dots represent ELP_{BC} with a hydrophobic block length of 90 pentapeptides.

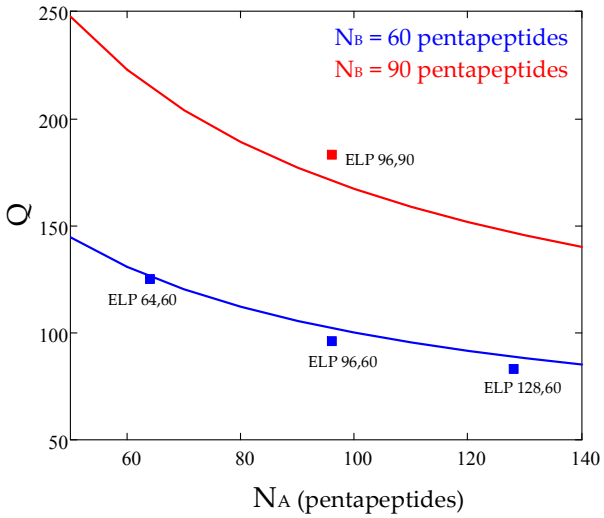

Figure 49: Change in aggregation number with increasing N_A. The solid lines represent the theoretical predication of aggregation numbers (exact numerical solution) while the dots indicate the experimentally measured aggregation numbers at 43 °C. The blue line and dots represent ELP_{BC} with a hydrophobic block length of 60 pentapeptides. The red line and dots represent ELP_{BC} with a hydrophobic block length of 90 pentapeptides.

While the qualitative trends confirm that ELPs behave similarly to synthetic diblocks and have similar power law dependence on block lengths, it is important to be able to quantitatively predict physical properties to understand if all energetic contributions are correctly accounted for within the model. Predicted aggregation numbers were found to be in good agreement with experimentally determined values as seen in Figure 49. Predicted total radii were larger than measured hydrodynamic radius values for all ELP_{BC} (Figure 48). The total radius is expected to be larger than the hydrodynamic radius as solvent drains through the last correlation blob in the corona resulting in a hydrodynamic radius that is smaller than the total radius of the micelle. The last correlation blob size is given by the following expression:

$$\xi_{last} = \frac{R_{total}}{\sqrt{Q}} p_A^{\frac{3}{4}}$$

As such, the total radius and hydrodynamic radius are related as follows:

$$R_{total} = R_h + C\xi_{last}$$

where C is constant on the order of unity. The correlation blob sizes were calculated for all six ELP$_{BC}$s and are listed in Table 8. The constant C was fit to 0.85. The experimentally determined hydrodynamic radii were compared to the predicted hydrodynamic radii (Figure 48). All four ELP$_{BC}$ predicted hydrodynamic radii are in good agreement with the corresponding experimental values.

Table 8: Size of correlation blob of spherical ELP micelles for all ELP$_{BC}$

N_A	ξ_{last} (nm)		
	N_B		
64	60	90*	120*
	5	5.3	5.1
96	60	90	
	6.1	5.7	
128	7		

* The correlation blob size for these ELP$_{BC}$s was calculated at 35 °C as opposed to the rest of the blob sizes which were calculated at 43°C.

As the total radius is an overall size, we examined the change in the two contributions to the total radius, the predicted corona thickness and core radius, with increasing N_A for ELP$_{BC}$ with a hydrophobic block length of 60 pentapeptides. Surprisingly, the model predicted that the corona thickness is close to its Gaussian size

(Figure 50). We consider, for example, ELP 96,60: the corona thickness as theoretically predicted by the model is 19.3 nm and the Gaussian size of the hydrophilic chain ($a_A\sqrt{p_A \mathrm{N}_A}$) is 19.5 nm. Yet, the model assumes that the corona is stretched. The numerical coefficients cannot be further adjusted within the set limitation and thus were precluded from further consideration. For the corona to be close to its Gaussian size, the interaction energy of the entire corona must be on the order of kT (as opposed to the interaction energy of a single correlation blob being on the order of kT). The total energy of the corona is 1.5 kT as estimated by the model which is consistent with the predicted Gaussian size. Furthermore, the core was found to be compressed in this model and while physically possible, the core block was also assumed to be stretched. Therefore, these inconsistencies in the model suggest that this model might require further modification to fit the ELP micelles.

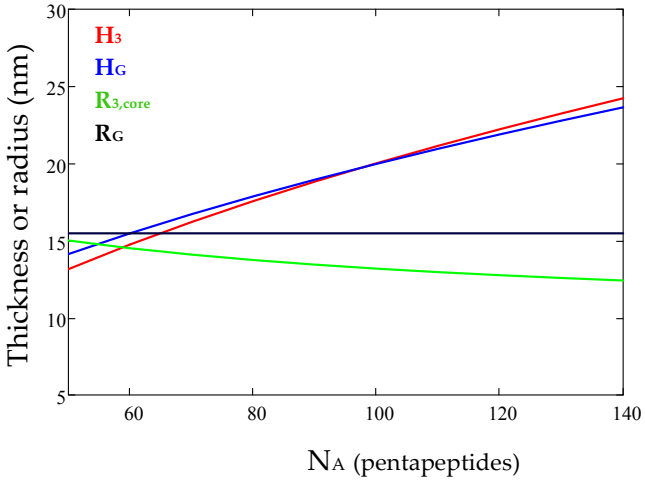

Figure 50: Predicted thickness of corona (H_3, red) and radius of core ($R_{3,core}$, green) compared to their Gaussian end-to-end distance with increasing N_A. The blue line represents the corona Gaussian end-to-end distance (H_G). The black line represents

the core radius Gaussian end-to-end distance (R_G). The hydrophobic block length for all four predicted values is fixed at 60 pentapeptides.

The phase diagram at 43 °C shows the experimentally determined morphologies as compared with the predicted phase boundaries (Figure 51). All the four ELP_{BC} with spherical morphology are above the spherical-to-cylindrical phase boundary. However, the two ELP_{BC} that are mixture of spheres and larger nano-scaled particles are also above the spherical-to-cylindrical boundary. Two explanations are possible: the model could be inaccurately predicting the spherical regime, or the two ELP_{BC} are undergoing a transition or aggregation event due to changes in the corona that are not accounted for in the model. The cylindrical and lamellar morphology regions cannot be established and verified experimentally without synthesis of additional N_A and N_B values.

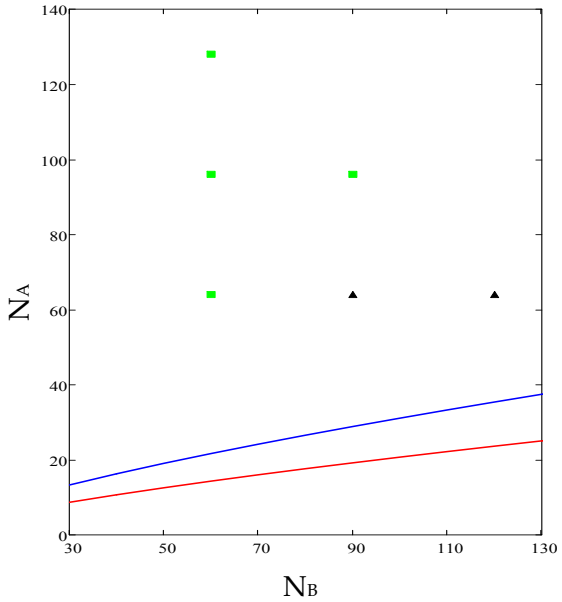

Figure 51: Theoretical and experimental phase diagram of morphologies with changing N_A and N_B (in pentapeptides) at 43°C. The blue (spherical-to-cylindrical) and red (cylindrical-to-lamellar) lines represent the exact theoretical phase boundaries while the dots represent the experimentally determined morphologies. The green

squares represent ELP_{BC} with spherical morphology. The black triangles represent the two ELP_{BC} that form mixed populations of spherical micelles and larger nano-scaled particles.

The PS-PI diblock system can be described fully by this regime in which the corona is highly stretched, the core is slightly stretched and the total free energy for the spherical micelles is large (larger than 6.5 kT). However, the ELP diblocks appear to have coronas that are unstretched and cores that are compressed. The differences between the previously studied PS/PI system and the ELP system that result in these differences are the smaller N_A and N_B of the ELP diblocks explored and the more rigid ELP chains (larger p_B values). Therefore, the next section will describe in detail a new model that describes a different regime. The new model will describe the regime in which the three-body monomer-monomer interactions in the corona are not sufficient to stretch the corona and the corona interaction energy per chain ($kT\omega a_A^6 N_A \phi_A^2$) is on the order of kT. In addition, the surface free energy per chain is less than kT. We will compare the predictions of the new model with the experimental data to test its validity.

4.7 Weak micelles

The new model expands on the previous model by describing new regimes within the N_A and N_B space. Previously, the model considered only the micelle regime in which the surface tension is greater than the thermal energy, kT, and the corona is highly stretched. This regime is referred to as regime III and the micelles are termed strong micelles. Regime I and Regime II explore the space in which these conditions do not hold (Figure 52).

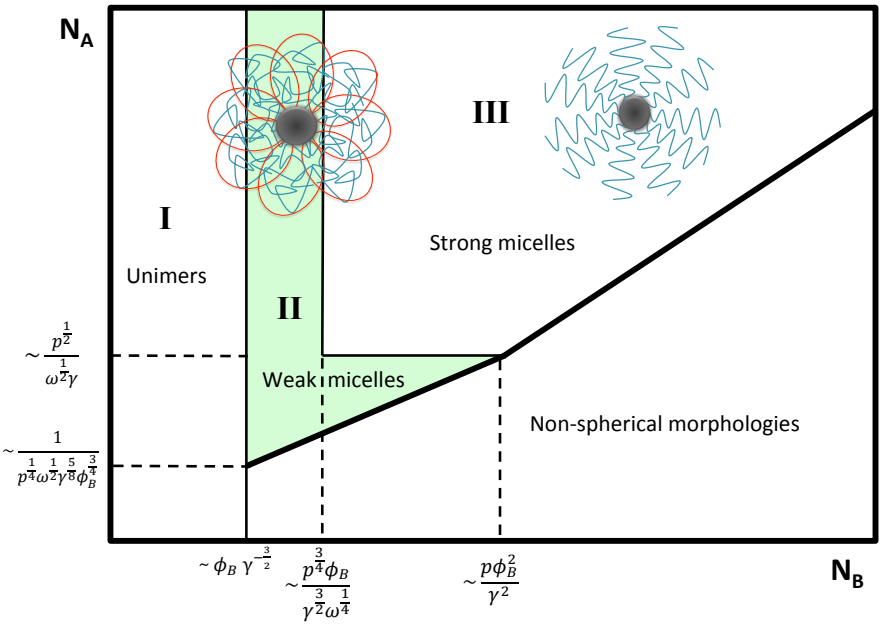

Figure 52: Schematic of states of ELP micelles in N_A and N_B space. ELP diblocks are unimers in regime I. ELP micelles are weak micelles in regime II (green). ELP micelles are strong micelles in regime III.

In regime I, the surface free energy of the collapsed hydrophobic block is not sufficient to overcome the loss in translational entropy due to self-assembly and the diblocks remain in their unimer state rather than self-assemble. The surface free energy

of the unimer ($\simeq \gamma R_{unimer}^2 \simeq \gamma\, a_B^2 (\frac{N_B}{\phi_B})^{\frac{2}{3}}$) is less than kT and thus is not sufficient to drive self-assembly. This regime is true for diblocks with small hydrophobic block lengths below a threshold of $\sim \phi_B\, \gamma^{-\frac{3}{2}}$ (i.e. small N_B values < 40 pentapeptides) for any given N_A.

In regime II, weak micelles are formed as the surface free energy of the collapsed hydrophobic block is above kT which drives self-assembly. However, upon aggregation to reduce the surface area and thereby surface free energy, the surface free energy per chain in the micelle is on the order of kT. The surface free energy expression for weak micelles is the same as for the strong micelles.

$$F_{3,interface} = kT \frac{3\gamma a_B N_B}{\phi_B R_3}$$

Upon self-assembly, the hydrophilic block forms the corona and can be considered as a brush tethered to the core surface. The corona thickness is determined by the balance of the interaction energy and the elastic energy. In the case of weak micelles, the ternary contacts are not sufficient to stretch the corona as the interaction free energy of the corona is on the order of kT and thus, the corona thickness is close to the Gaussian end-to-end distance of the hydrophilic block. As the interaction energy is on the order kT, then the elastic energy is also on the order of kT as well. The interaction free energy for a spherical morphology (j= 3) can be derived as follows:

$$F_{3,interaction} = kT\omega N_A \phi_A^2 \approx kT$$

The volume fraction of the corona (ϕ_A) is approximated with a box-like model and can be expressed in terms of the volume fraction of the core (ϕ_B). The corona volume fraction and the core volume fraction can be expressed as follows:

$$\phi_A = \frac{N_A a_A^3 Q}{\frac{4}{3}\pi((R_3 + H_3)^3 - R_3^3)}$$

$$\phi_B = \frac{N_B a_B^3 Q}{\frac{4}{3}\pi R_3^3}$$

Substituting the expression for the core volume fraction into that of the corona, we obtain the following expression:

$$\phi_A = \frac{\phi_B N_A}{N_B\left[\left(1 + \frac{H_3}{R_3}\right)^3 - 1\right]}$$

and substituting the ϕ_A expression derived above into the interaction free energy, we get the following expression:

$$F_{3,interaction} = kT\omega N_A^3 \frac{\phi_B^2}{N_B^2\left[\left(1 + \frac{H_3}{R_3}\right)^3 - 1\right]^2}$$

The elastic energy of the corona is the combination of the stretching and confinement energies as follows:

$$F_{3,coronaelastic} = kTb[\frac{H_3^2}{R_{GA}^2} + \frac{R_{GA}^2}{H_3^2}]$$

where b is a numerical coefficient. While previously the confinement penalty for the corona was ignored as the corona was assumed to be highly stretched, for weak micelles, the elastic energy is on the order of kT and thus it is important to include both

components. The balance of the two components, in the absence of interaction energy (ω = 0), results in an equilibrium state with a Gaussian end-to-end distance.

The elastic energy of the core is expressed as follows:

$$F_{3,coreelastic} = kTb[\frac{R_3^2}{R_{GB}^2}]$$

The confinement energy is ignored for the core block since it is smaller than kT because the core block is in a dense melt-like environment for which the penalty of confinement is not significant. However, the elastic energy of the core is ignored, as it is insignificant compared to the two other dominant energies.

The total free energy is composed of the sum of the two free energies:

$$F_3 = kT\omega N_A^3 \frac{\phi_B^2}{N_B^2\left[\left(1+\frac{H_3}{R_3}\right)^3-1\right]^2} + kTb\left[\frac{H_3^2}{R_{GA}^2}+\frac{R_{GA}^2}{H_3^2}\right] + kT\frac{3\gamma a_B N_B}{\phi_B R_3}$$

By finding the minimum of the first partial derivative with respect to H_3 and with respect to R_3, a numerical solution for R_3 and H_3 can be found and used to calculate the total radius and aggregation number according to the equations below.

$$R_{total} = H_3 + R_3$$

$$Q = \frac{4\pi\phi_B R_3^3}{3N_B a_B^3}$$

The model was fit with ϕ_B = 0.6, a numerical coefficient b = 1.5 (corresponding to the stretching of a Gaussian chain) and a three-body interaction parameter (ω) of 1.5.

First, we compared the predicted Q using the weak micelle model to the experimental values. The weak micelle model predicted the aggregation numbers of the

four ELP$_{BC}$s forming spherical micelles at 43 °C accurately (Figure 53). The change in aggregation numbers with N_A and N_B is predicted quantitatively and qualitatively. As expected aggregation numbers decreased with increasing N_A and increased with increasing N_B.

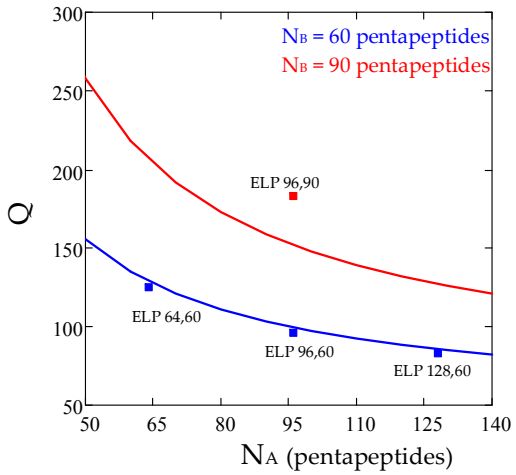

Figure 53: Change in aggregation number of weak micelles with increasing N_A. The solid lines represent the theoretical predications (exact numerical solution) while the dots indicate the experimentally measured aggregation numbers at 43 °C. The blue line and dots represent ELP$_{BC}$ with a hydrophobic block length of 60 pentapeptides. The red line and dots represent ELP$_{BC}$ with a hydrophobic block length of 90 pentapeptides.

In addition to predicting aggregation number, we compared the predicted R_{total} using the weak micelle model to the experimentally determined hydrodynamic radii (Figure 54). As expected, the radius increases with increasing N_A and increasing N_B. The hydrodynamic radii for the four ELP$_{BC}$s that form spherical micelles at 43 °C are smaller than the predicted total radii as expected. By examining the predicted corona thickness and the core radius, we observed that the corona is slightly stretched but near its Gaussian end-to-end distance as expected while the core is compressed (Figure 55). We

further examined the total radius prediction by understanding its relation to the hydrodynamic radius. As mentioned previously, the hydrodynamic radius is smaller than total radius due to solvent draining through the last correlation blob in the corona. Therefore, we estimated the correlation blob size for the corona in the weak micelle model. The correlation blob (ξ) size was calculated based on the derivation of the correlation blob of a semi-dilute solution. The corona in the weak micelles is consistent of weakly overlapping near Gaussian chains as can be inferred from estimating the overlap parameter for these chains. By dividing the surface area of micelle by the surface area of a Gaussian chain, we determined that overlap parameter for the hydrophilic chains is approximately 4 chains. Thus, we used the following expression for semi-dilute solutions to estimate the correlation blob size:

$$\xi \approx H_G \frac{\phi^*}{\phi_A}$$

where ϕ^* is the overlap concentration, ϕ_A is the corona concentration and H_G is the Gaussian end-to-end distance. These three variables can be expressed as follows:

$$H_G = a_A\sqrt{p_A \mathrm{N}_A}$$

$$\phi^* = \frac{3N_a a_A^3}{4\pi(H_G/2)^3}$$

$$\phi_A = \frac{N_A a_A^3 Q}{\frac{4}{3}\pi((R_3 + H_3)^3 - R_3^3)}$$

The correlation blob size was calculated for all six ELP$_{BC}$s for weak micelles and is listed in Table 9. The hydrodynamic radius was calculated by adjusting the total radius by the

correlation blob size and is plotted in Figure 54. The predicted hydrodynamic radii are in good agreement with measured hydrodynamic radii.

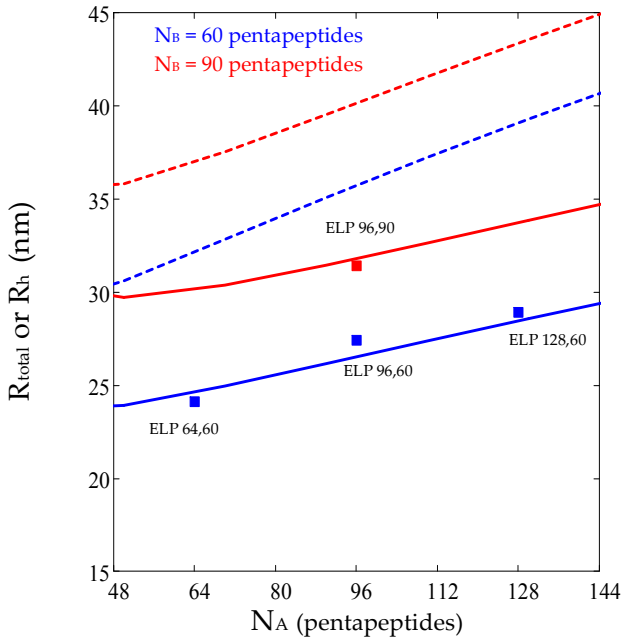

Figure 54: Change in total radius and hydrodynamic radius for weak micelles with increasing N_A. The solid lines represent the theoretical predication of hydrodynamic radii. The dashed lines represent the predicted total radii (exact numerical solution). The dots indicate the experimentally measured hydrodynamic radii at 43 °C. The blue lines and dots represent ELP_{BC} with a hydrophobic block length of 60 pentapeptides. The red lines and dots represent ELP_{BC} with a hydrophobic block length of 90 pentapeptides.

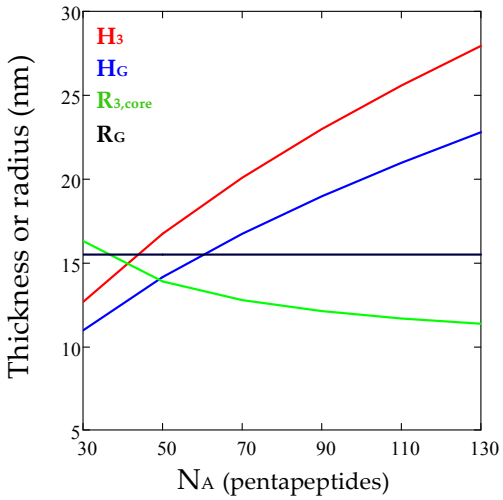

Figure 55: Predicted thickness of corona (H_3, red) and radius of core ($R_{3,core}$, green) of weak micelles compared to their Gaussian end-to-end distance with increasing N_A. The blue line represents the corona Gaussian end-to-end distance (H_G). The black line represents the core radius Gaussian end-to-end distance (R_G). The hydrophobic block length for all four predicted values is fixed at 60 pentapeptides.

Table 9: Size of correlation blob of ELP micelles for all ELP_{BC} for weak micelles

N_A	ξ Weak (nm)		
	N_B		
64	60	90*	120*
	7.5	7.9	7.4
96	60	90	
	9.2	8.4	
128	10.6		

*The correlation blob size for these ELP_{BC}s was calculated at 35 °C as opposed to the rest of the blob sizes which were calculated at 43°C.

The weak micelle model is able to predict both physical properties

simultaneously suggesting that ELP_{BC} micelles can also be described by the weak micelle

regime (regime II). As seen in Figure 56, the total free energy of the ELP_{BC} micelles in the weak micelle regime is ~3 kT and ~4 kT in the strong micelle regime. The difference is 1 kT between the two regimes stems from the difference in total corona free energy. Both regimes predict a total free energy for these micelles that is much lower than the PS-PI spherical micelles previously studied which are in the strong micelle regime and have total free energies greater than 6 kT. The ability of both models to predict the physical properties of the micelles, the predication of both models of a corona near Gaussian size, and the low total free energy suggest that the ELP micelles are in the crossover regime between weak and strong micelles. The two regimes presented here are asymptotes describing two extremes while physically a continuous spectrum between the two regimes exist as N_A and N_B are changed. A derivation describing the crossover between the two regimes will most likely be the most accurate description of these ELP micelles.

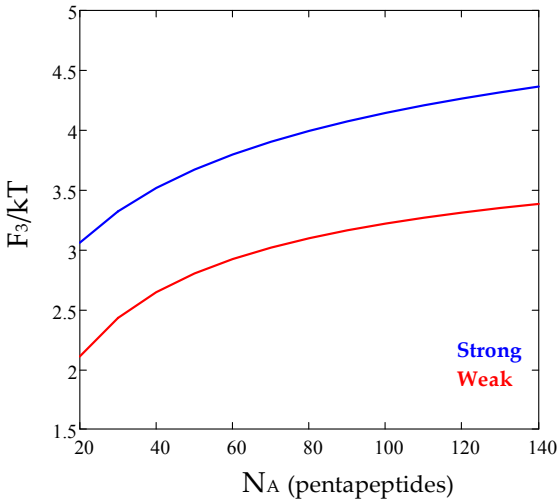

Figure 56: Total free energy of ELP_{BC} with increasing N_A for strong (blue) and weak (red) micelle regimes for hydrophobic block length of 60 pentapeptides.

In a similar fashion as described for strong micelles, the total free energies of the two remaining morphologies (cylindrical (j = 2) and lamellar (j =1)) were calculated. As with the previous model, the phase boundaries at which the morphological changes occur were calculated by finding N_A and N_B values for which the energies of the two morphologies are equal. The elastic core energy term is included in this calculation. Similar to the strong micelle model, the spherical micelles are above the spherical-to-cylindrical boundary. However, the two ELP_{BCS} (ELP 64,120 and ELP 64,90) that are composed of two populations, spherical micelles and larger nano-scaled particles are also above the spherical-to-cylindrical phase boundary. Additional ELP_{BC} with small N_A and large N_B must be examined to verify the phase boundaries correctly.

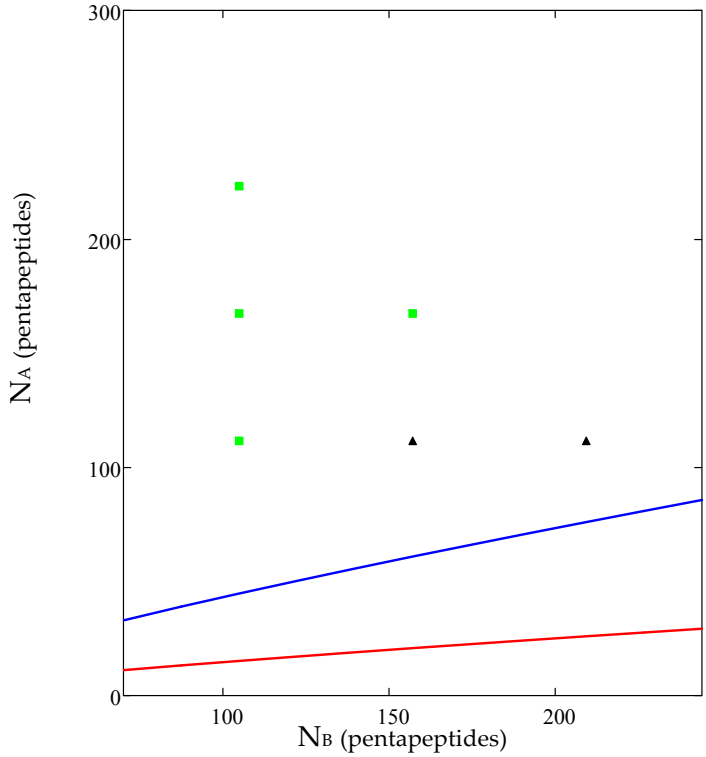

Figure 57: Theoretical and experimental phase diagram of morphologies with changing N_A and N_B (in pentapeptides) at 43°C. The blue (spherical-to-cylindrical) and red (cylindrical-to-lamellar) lines represent the exact theoretical phase boundaries calculated for the weak micelle regime while the dots represent the experimentally determined morphologies. The green squares represent ELP_{BC} with spherical morphology. The black triangles represent the two ELP_{BC} that form mixed populations of spherical micelles and larger nano-scaled particles.

4.8 Critical micelle temperature

Unimers associate to form a micelle to decrease the surface tension of the collapsed hydrophobic block at their critical micelle temperature. At this temperature, the unimer chemical potential is equal to that of micelle. The unimer chemical potential is composed of the translational entropy as well as the surface free energy. The translational entropy of the unimer is related to the concentration of the solution

($kT\ln(\phi)$). The surface free energy of the unimer (F_{s0}) is related to the surface tension per unit area ($\tilde{\gamma}$) and the surface area of the collapsed hydrophobic block.

$$\frac{F_{s0}}{kT} = 4\pi {R_o}^2 \tilde{\gamma}$$

The radius of the collapsed hydrophobic block (R_o) can be expressed in terms of volume fraction inside the globule (which is assumed to be the same as the micelle core volume fraction) as follows:

$$R_o = \left[\frac{3a_B^3 N_B}{4\pi\phi_B}\right]^{\frac{1}{3}}$$

Substituting back into the equation for the surface free energy of a unimer, we obtain the following expression:

$$\frac{F_{s0}}{kT} = (36\pi)^{\frac{1}{3}}\left(\frac{N_B}{\phi_B}\right)^{\frac{2}{3}} \tilde{\gamma} a_B^2$$

For the micelle, the translational entropy of the unimer within the micelle is negligible. The free energy of the micelles (F_3) is composed of the three free energies (corona, interface and core) and is given by the same expression discussed in the previous section.

$$F_3 = F_{3,interface} + F_{3,interaction} + F_{3,elastic}$$

F_3 is approximated to be 3 kT as calculated from the weak micelle model and 4 kT as calculated from the strong micelle model.

We equate the chemical potential of the unimer and micelle as follows to derive an expression for the critical micelle temperature:

$$kT\ln(\phi) + F_{so} = F_3$$

Substituting the expression for the surface free energy of the unimer and the approximated free energy of the weak micelles into the expression above, we get the following expression.

$$\ln\phi + (36\pi)^{\frac{1}{3}}\left(\frac{N_B}{\phi_B}\right)^{\frac{2}{3}}\tilde{\gamma}a_B^2 = 3$$

A relationship between surface tension and temperature has been previously established in section 4.3 of this chapter as follows:

$$\frac{\tilde{\gamma}}{\phi_B{}^{\frac{2}{3}}} = 0.00733CMT - 2.13$$

By combining the equation relating surface tension with temperature and surface tension with concentration, we obtain an expression that relates CMT to concentration of solution below. This equation was used to predict the CMT for a range of N_A and N_B values (Figure 58).

$$CMT = \frac{3 - \ln\phi}{0.00733(36\pi)^{\frac{1}{3}}a_B^2 N_B{}^{\frac{2}{3}}} + \frac{2.13}{0.00733}$$

The predicted values of CMT are in good agreement with the experimental values for all six ELP_{BC}s. The surface plot of CMT at various N_A and N_B values crosses the experimental data at the temperature where the unimers are observed to self-assemble into micelles as evidenced by the change in the hydrodynamic radius. If the higher micelle total free energy of 4 kT (from strong micelle model) is used, the predicted CMT shifts upward by 1-2 °C resulting in a worse fit indicating that perhaps

the weak micelle model yields a better prediction of the total free energy. The ability to predict the CMT validates the surface tension measurements and calculations used to fit the model. In addition, for any given block lengths, we can now predict the CMT prior to synthesis of that ELP diblock.

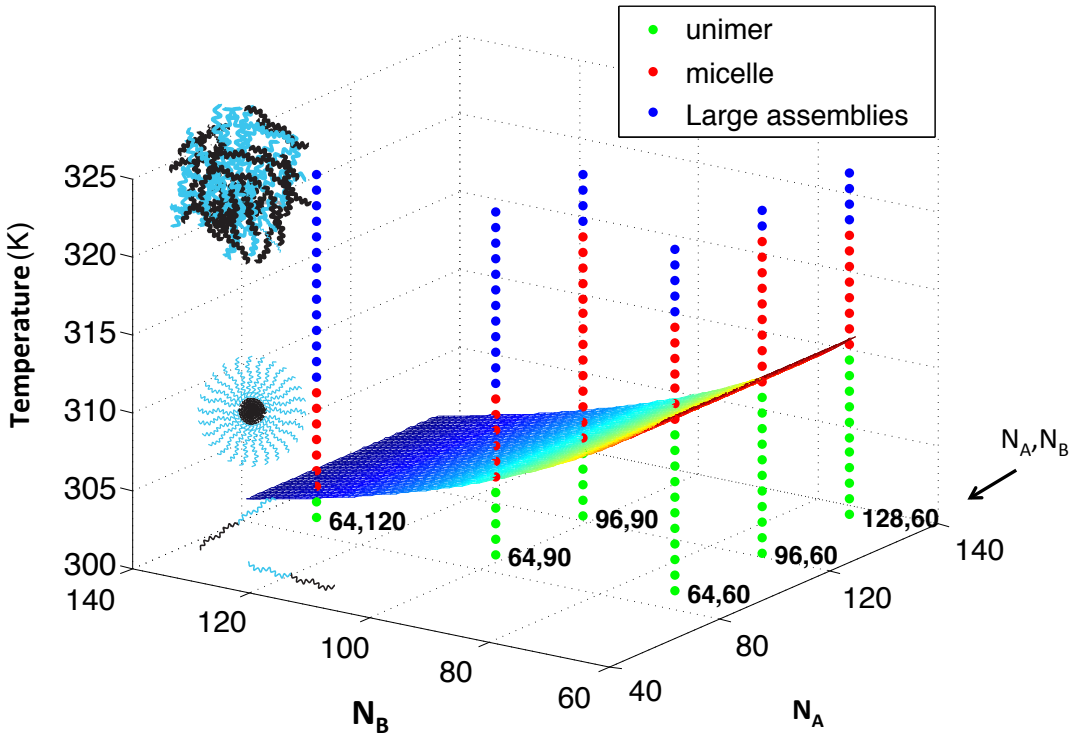

Figure 58: Critical micelle temperature as determined experimentally and theoretically. The dots represent experimental data for all six ELP$_{BC}$. Green dots represent unimers, red dots represent spherical micelles, and blue dots represent any particles larger than the spherical micelles. The surface represents the theoretically predicted critical micelle temperature. N_A and N_B here are pentapeptide repeats.

4.9 Effect of temperature on aggregation number and radius of micelles

The previous sections compared the prediction of both models to experimental data at one temperature, 43 °C. Here, we explore the effect of temperature on two

micelle properties: radius and aggregation number. Figure 59 and Figure 60 show the change in aggregation number and radius for all six ELP$_{BC}$s for the temperature range in which spherical micelles are observed. For weak micelles, the three-body interaction parameter (ω) used to fit the model was 1.5 which is the value used in the previous sections at 43 °C. For strong micelles, C_F was set to 1.4 and C_H was set to 1, the same values previously used to fit the model.

The hydrodynamic radius increases minimally with increasing temperature for all six ELP$_{BC}$s (~ 1-2 nm) while the aggregation number is observed to increase significantly for all six ELP$_{BC}$s (an increase of about 20-30 unimers in aggregation number per 1°C increase). Both weak micelle and strong micelle models predict a small slope for the change in radius with temperature that is in good agreement with the observed change in hydrodynamic radius with temperature for all ELP$_{BC}$s. The weak micelle model predicts that the total radius is larger than the hydrodynamic radius for all six ELP$_{BC}$s at all temperatures. However, the strong micelle model predicts that the total radius is larger than the hydrodynamic radius for four ELP$_{BC}$s (ELP 64,60, ELP 96,60, ELP 128,60, and ELP 96,90) which were previously studied at 43 °C but predicts a total radius equal to the hydrodynamic radius for ELP 64,90 and ELP 64,120. This result suggests that one set of values of the numerical coefficients could not predict all ELP$_{BC}$s radii correctly at all temperatures.

Qualitatively, both models predicted an increase in aggregation numbers with an increase in temperature. Quantitatively, both weak and strong micelle models did not predict the drastic increase in aggregation number with temperature for any of the six ELP_{BC}s. The strong micelle model predicted a larger increase in aggregation number than the weak micelles. However, both models underestimated this increase dramatically (a predicted increase of ~4-10 unimers in aggregation number per 1°C increase versus an experimentally measured increase of about 20-30 unimers in aggregation number per 1°C increase).

We hypothesized the perhaps the change in excluded volume (v) in the corona with temperature could account for the observed drastic increase in aggregation numbers. Therefore, the weak micelle model was modified to include a term for two-body interactions in the corona as follows:

$$F_{3,two-body\ interaction} = kTvN_A^2 \frac{\phi_B}{N_B^2\left[\left(1+\frac{H_3}{R_3}\right)^3 - 1\right]}$$

A relationship between excluded volume and temperature was determined from the previously measured excluded volume at a range of temperatures (Table 6). The slope (k) of the following equation $\frac{\boldsymbol{v}}{\boldsymbol{a_A^3}} = \boldsymbol{k}(\frac{\boldsymbol{\theta}}{\boldsymbol{T}} - \mathbf{1})$ relating measured excluded volume and temperature was fit as seen in (Figure 61) where $\boldsymbol{\theta}$ is the theta temperature and is approximated to be 41 °C. The predicted aggregation numbers from the modified weak micelle model are plotted in green in Figure 59. The slope of the aggregation number

versus temperature increased upon inclusion of the two-body interaction. However, even with this additional consideration, the increase was not sufficient to match the increase observed in the experimental data.

In conclusion, neither a single value of the three-body interaction parameter nor a single set of C_F and C_H values could predict the change in aggregation number with increasing temperature. These results indicate that an additional contribution leads to the drastic increase in aggregation numbers. One hypothesis is that the increase in Kuhn length due to increase in secondary structure could be responsible for the drastic increase in aggregation number with increasing temperature.

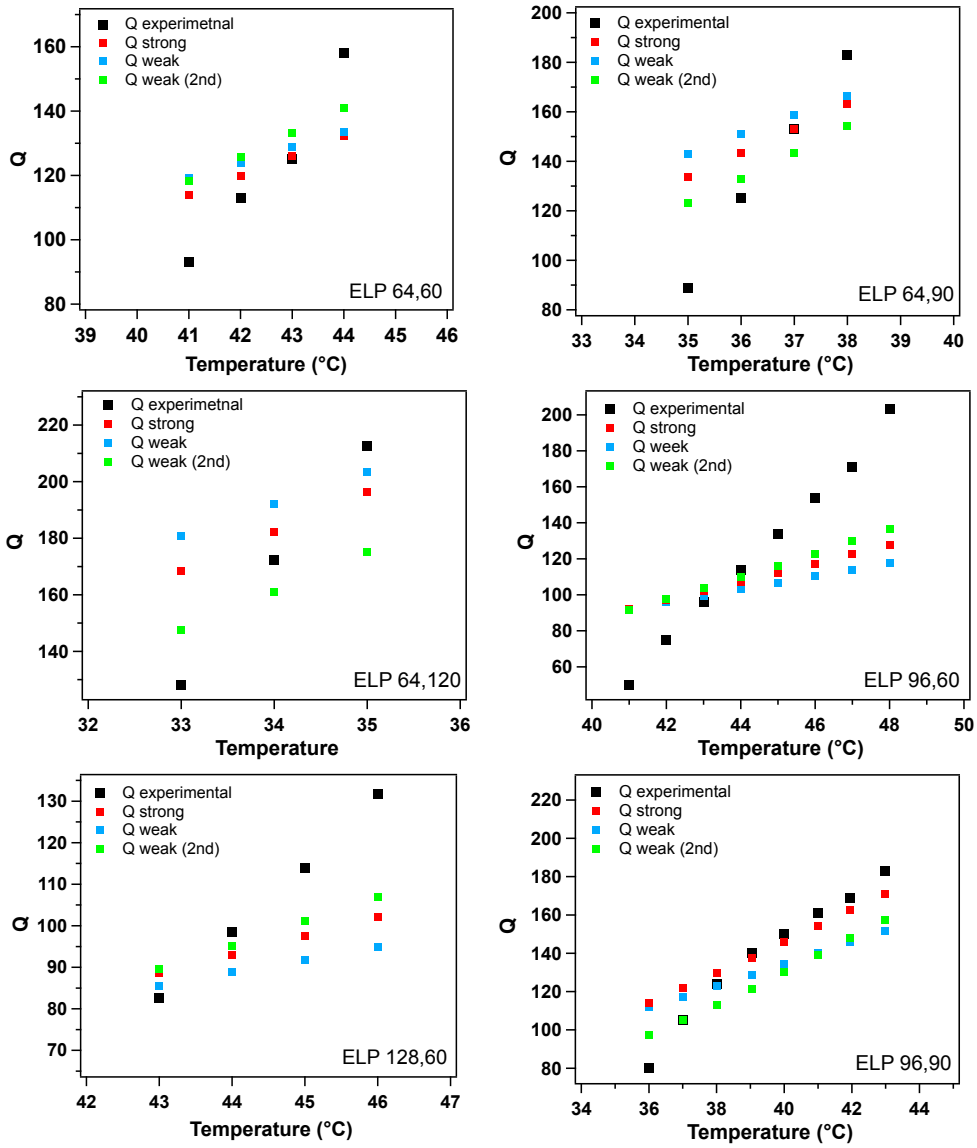

Figure 59: Change in aggregation number with temperature for all six ELP$_{BC}$s. The experimental aggregation number (black) is compared to predictions of the total aggregation number from the strong micelle model (red), the weak micelle model (blue) and the adjusted weak micelle model (green) which accounts for the two-body interactions in the corona.

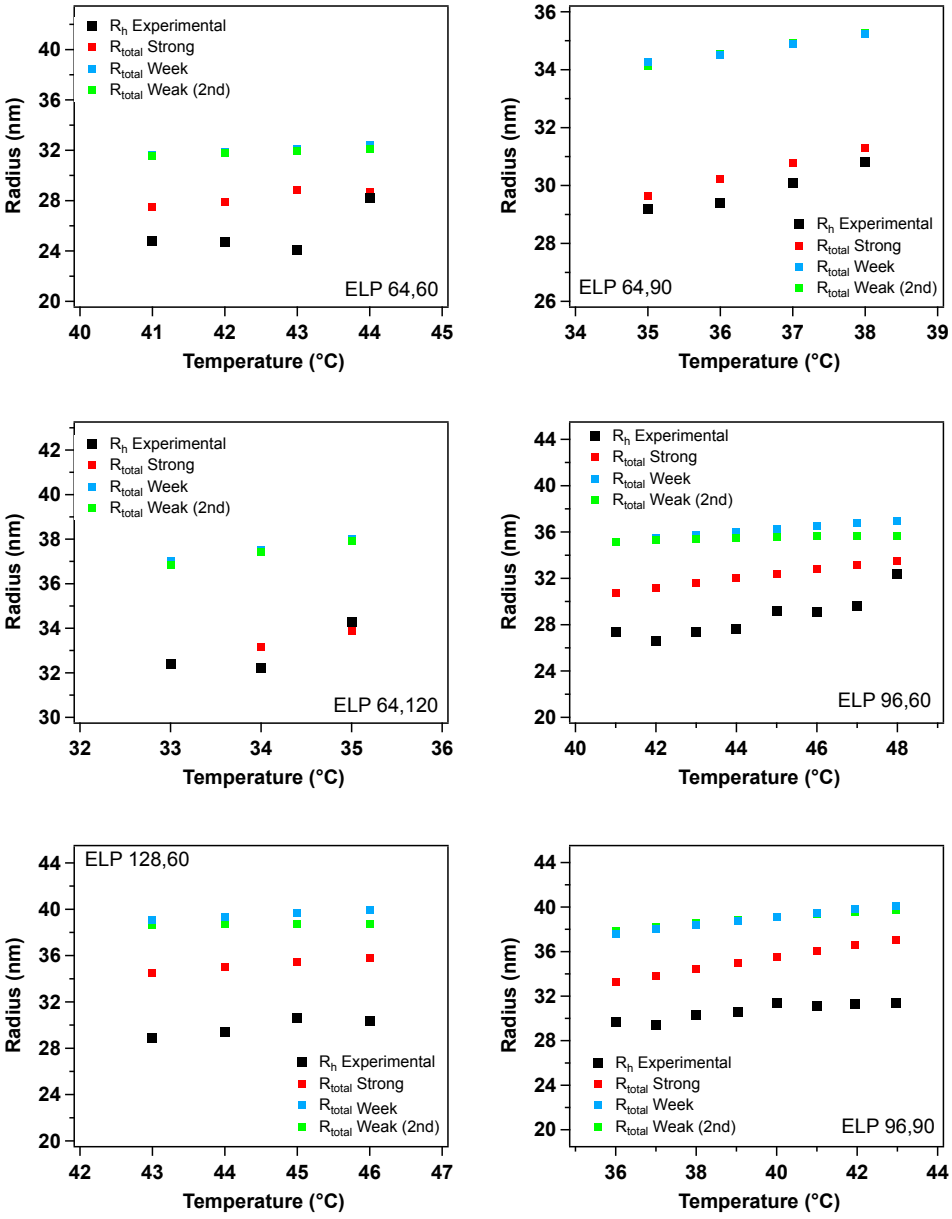

Figure 60: Change in radius with temperature for all six ELP$_{BC}$s. The experimental hydrodynamic radius (black) is compared to predictions of the total radius from the strong micelle model (red), the weak micelle model (blue) and the adjusted weak micelle model (green) which accounts for the two-body interactions in the corona.

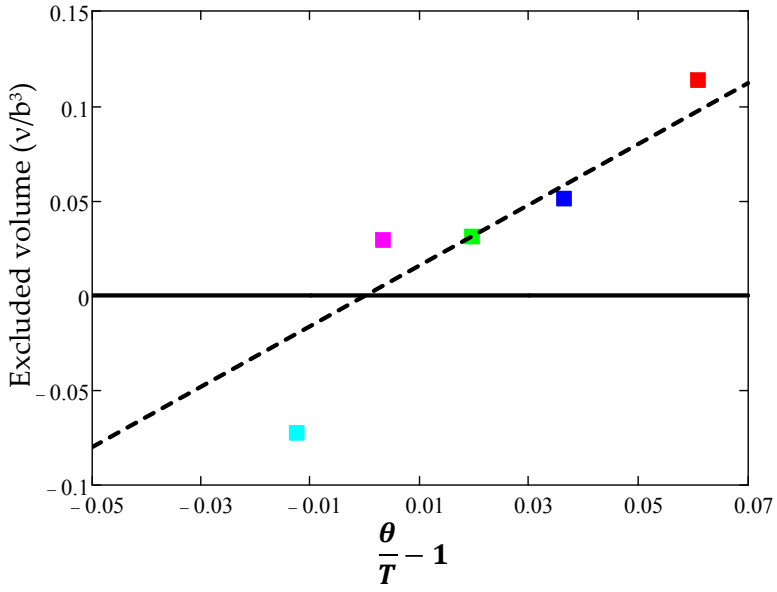

Figure 61: Experimentally determined excluded volume versus $\frac{\theta}{T} - 1$ where θ is the theta temperature. The theta temperature is approximated to be 41 °C, as it is experimentally determined to be between 40 and 45 °C. The slope of the linear fit was found to be 1.6. The y-intercept was set to zero.

5. Conclusions and future directions

5.1 Key conclusions

In this dissertation, two main studies were conducted to further the understanding of ELP_{BC} self-assembly. In chapter 2 and 3, we examined the ability of ELP_{BC} self-assembly behavior to tolerate the fusion of proteins that are 100-20 amino acids long. In chapter 2, four proteins were fused to a set of six previously synthesized and characterized ELP_{BC}s known to self-assemble into spherical micelles. The set of ELP_{BC}s differed by their block lengths and the ratio of the two fused blocks. Each fused protein was found to have the same affect on the thermal behavior of all six ELP_{BC}s indicating that the lengths and ratios of the blocks were not factors in the self-assembly of protein ELP fusions. While two of the chosen proteins, blue fluorescent protein and a nanobody against lysozyme, were found to disrupt self-assembly, the other two, Fibronectin domain against the integrin $\alpha_v\beta_3$ and thioredoxin, preserved the self-assembly behavior of ELP_{BC}s. The proteins that disrupted self-assembly caused the protein ELP_{BC} fusion to transition from unimer to aggregates rather than exhibit the three state behavior of ELP_{BC}. However, the transition of these protein ELP_{BC}s was not as smooth and sharp as the transition of ELP monoblocks. The transition occurred at a temperature close to that of the ELP_{BC} CMT. The proteins that did not disrupt self-assembly still affected the thermal behavior of the two blocks. While both proteins did not affect the CMT, they did affect the micelle-to-aggregate transition. The hydrophilic

protein, thioredoxin, increased the micelle-to-aggregate transition temperature while the hydrophobic protein, Fibronectin, decreased it. This observation indicated that the protein interacts with the hydrophilic block in a similar fashion to proteins fused to ELP monoblocks.

In chapter 3, we explored the effect of the guest residue composition of the two blocks on the self-assembly of the protein ELP_{BC}. The four proteins explored previously were used for this study. Six new ELP_{BC}s were synthesized with the goal of increasing the hydrophobicity of the core and increasing the hydrophilicity of the corona. Hydrophobic blocks were created with guest residues leucine, isoleucine and tryptophan mixed with the guest residue valine. Two hydrophilic blocks were synthesized, one with alanine and glycine as guest residue at a ratio of 1:1 and one with serine as a guest residue. While the increased hydrophobicity/hydrophilicity resulted in a significant increase in the micelle-forming temperature range (~48 °C versus 12°C), the four proteins had the same effect as observed before. This result indicated two things: the proteins dominate interactions that control self-assembly and the protein must interact with the hydrophobic block when the self-assembly is disrupted. In addition, a design rule for ELP_{BC} was illuminated in examining the thermal properties of the new free ELP_{BC}s. The CMT is unaffected by the composition of the hydrophilic block and the hydrophilic block is also unaffected by the composition or length of the hydrophobic block. As such, a desired micelle-forming temperature range can be obtained from

combining two ELP blocks with the desired CMT and micelle-to-aggregation temperature.

In chapter 4, we detailed the results of our study to gain a theoretical understanding of the self-assembly behavior of ELP_{BC}s. A theoretical model for the self-assembly of synthetic diblocks has been previously compared to experimental data and found to be in agreement. The model is based on the three free energies that control the self-assembly process: corona elastic and interaction energy, interface free energy and core elastin energy. We applied this theoretical model to polypeptides to see if the theory can be extended to predict ELP behavior. To apply the model, two parameters were measured: solvent quality of corona and surface tension of hydrophobic block. The corona was determined to be in theta solvent indicating that the three-body interactions dominate the interaction energy. The surface tension equation was derived by equating the chemical potential of a unimer globule with that of the sediment. As surface tension is related to concentration of globules in a two-phase solution, a relationship between concentration of globules and temperature was determined and subsequently used to relate surface tension to temperature.

The theoretical predictions of micelle radius and aggregation number were compared to the experimental values. The model can qualitatively and quantitatively predict the trends of change in aggregation number and radius with changing N_A and N_B. The predicted thickness of the corona was close to the Gaussian end-to-end distance

of the hydrophilic block. However, the model assumes a highly stretched corona. Therefore, a new model was developed that describes a micelle termed as a weak micelle (as opposed to the strong micelles described in the old model). Weak micelles are defined as having a Gaussian corona thickness as interaction energy, surface energy and elastic corona energy are on the order of kT (thermal energy). The model predictions of aggregation numbers and radii are comparable to experimental values for a given temperature. The total radius was larger than the hydrodynamic radius as expected. As both strong and weak micelle models are able to predict the properties of ELP micelles, we hypothesize that the ELP micelles are in the crossover regime between these two models.

A limitation of both strong micelle and weak micelle models is the inability to predict the increase in aggregation number with temperature. While both models predict the correct trend (i.e. increase in aggregation with increase in temperature), they fail to quantitative predict the increase. The weak micelle model was modified to account for two-body interactions in the corona. The excluded volume was calculated from the measured second virial coefficients at a range of temperatures. The modification in the model, however, was not sufficient to increase the slope of the predicted aggregation number versus temperature to match the experimentally determined values. These results suggest that additional factors must be considered such as increase in chain rigidity with an increase in temperature.

5.2 Future Directions

To further understand the effect of proteins on the self-assembly of ELP_{BC}, additional proteins of varying molecular weights and hydrophobicities should be fused to ELP_{BC}. These additional studies should be carried out using the ELP_{BC} composition that yielded the largest micelle-forming temperature range of 48 °C. This ELP_{BC} is composed of a hydrophilic block with serine as the guest residue and a total of 80 pentapeptides, and a hydrophobic block with tryptophan and valine at a ratio of 1:4 as the guest residues and a total of 40 pentapeptides. This ELP_{BC} should also be further characterized by measuring the fluorescence change of tryptophan as the hydrophobic block goes from a hydrated state to a desolvated state. While this composition is recommended for exploration of uncharged ELP micelles, including charged guest residues in the coronal block such as glutamic acid might prevent proteins from interaction with the core due to electrostatic repulsion between the protein and the corona and are worth exploring.

Perhaps a more fundamental study to understand the interaction between the protein and ELP_{BC} is to measure the interaction parameter between the three components of the protein ELP_{BC} fusion. The interaction can be determined by measuring the second virial coefficient using static light scattering. All permutations of a mixture of two of the three components (protein, hydrophilic ELP monoblock, hydrophobic ELP monoblock) should be measured to obtain the complete set of

interaction parameters between the components. These values will elucidate which interactions dominate the self-assembly of protein ELP_{BC} behavior and the difference in interaction patterns and strengths between proteins that disrupt self-assembly and those that do not (e.g. Fn3 versus VHH). In addition, the difference in interaction patterns between Trx and Fn3 could indicate the reason that Trx increases the micelle-to-aggregate transition temperature while Fn3 deceases it. One challenge in the execution of these experiments is the purity of the four proteins as static light scattering is sensitive to any aggregates present in the sample due to contaminants. Chromatographic methods such as ion exchange chromatography should be implemented in addition to immobilized-metal affinity chromatography.

In moving forward with the theoretical understanding of ELP_{BC}, several aspects must be addressed. First, additional block lengths and ratios must be synthesized to explore more of the N_A/N_B space. Block lengths can be chosen based on the predicted morphology phase boundaries. Exploration of this space in small N_A values and large N_B values might illuminate the cylindrical micelle regime. Second, the corona thickness and core radius should be determined experimentally using small angle neutron scattering (SANS). SANS requires the selective labeling of one block with deuterium. These measurements will confirm the state of the corona (Gaussian or stretched) and confirm that ELP micelles are within the weak/strong micelle cross-over regime. Third, equations describing the crossover regime between weak and strong micelles should be developed

and applied to the ELP$_{BC}$ system. Fourth, additional contributions must be explored to explain the change in aggregation number with temperature. This step might require the quantification of the increase in secondary structure with temperature and its energetic contribution as well as the effect on the Kuhn length. Finally, it would be of interest to also apply the model to ELP$_{BC}$s with different compositions than the initial set of ELP$_{BC}$s explored, particularly compositions such as serine and tryptophan which have displayed a wide range of micelle-forming temperatures and whose aggregation number does not change as steeply with temperature.

Appendix A

In this appendix, the thermal behavior of the two proteins ELP_{BC} sets (Trx and Fn3) which retain self-assembly behavior is detailed (Figure 62 and Figure 63). The behavior is examined through monitoring the change in absorbance and hydrodynamic radius with increasing temperature. The behavior determined from both methods is consistent. As previously detailed in chapter 2, Trx extends the micelle-forming temperature range while Fn3 reduces the range, both by increasing or decreasing the micelle-to-aggregate transition temperature respectively but not affecting the CMT. The fused protein does not affect the hydrodynamic radius for a given ELP_{BC}.

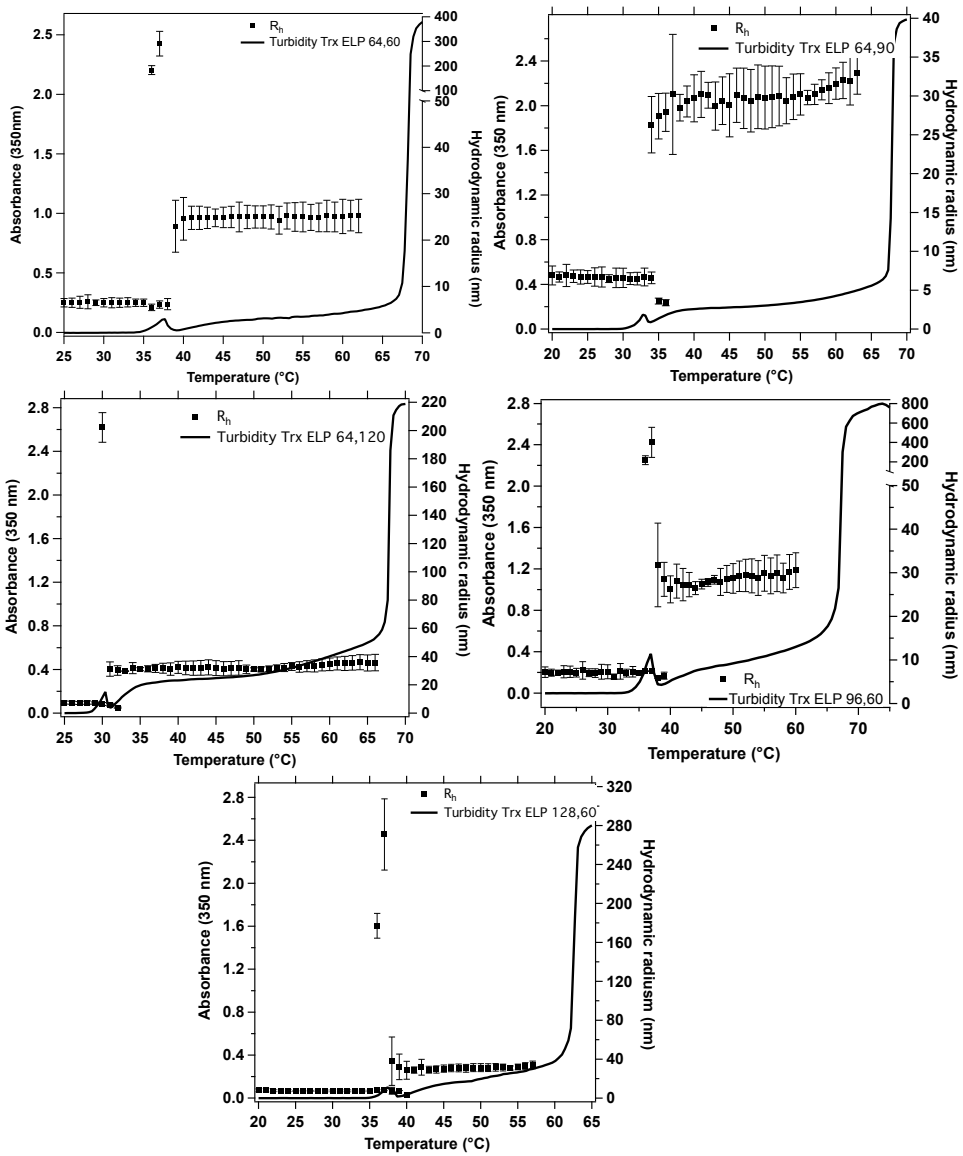

Figure 62: Thermal behavior of Trx ELP$_{BC}$s as determined by change in absorbance and hydrodynamic radius (R_h) with increasing temperature at 25μM in PBS. The thermal behavior correlates between the two methods.

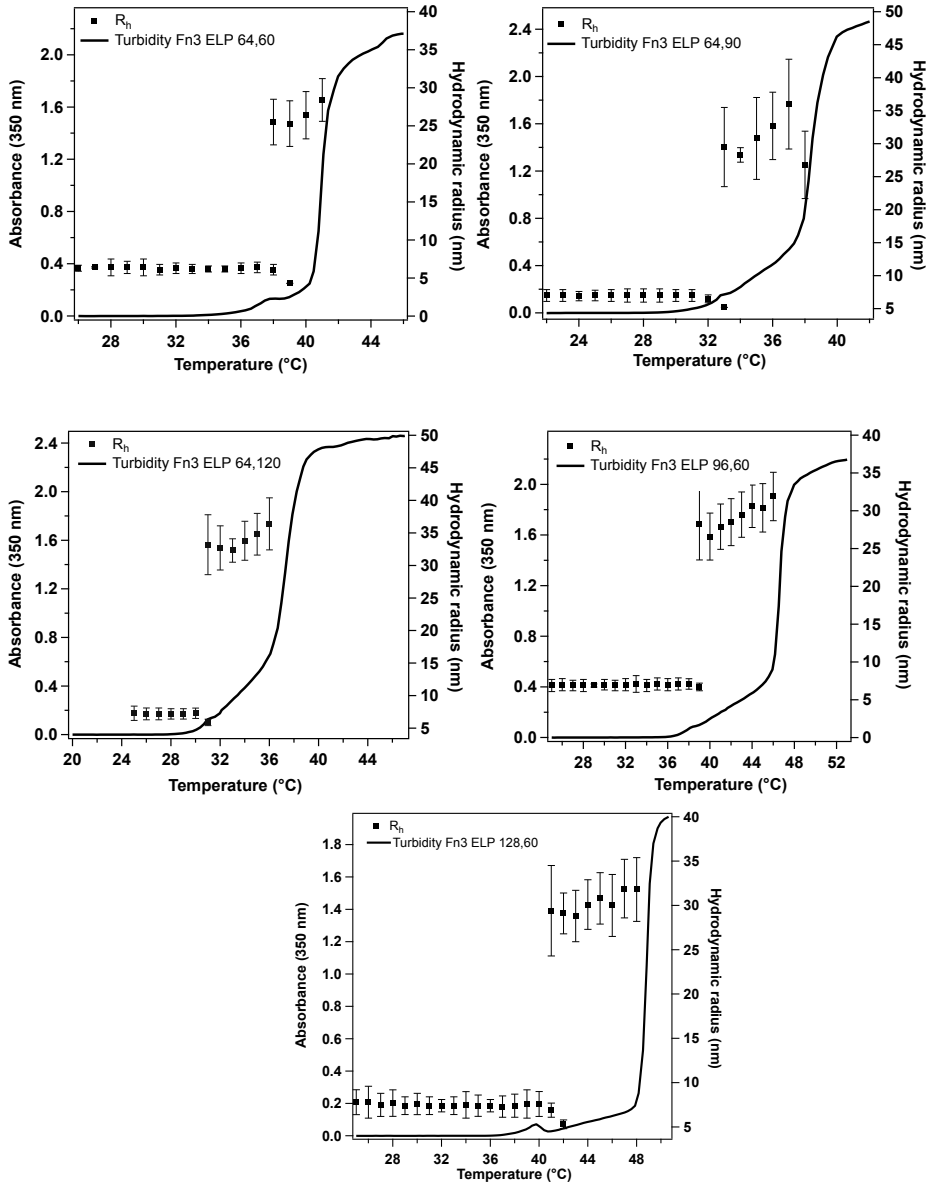

Figure 63: Thermal behavior of Fn3 ELP$_{BC}$s as determined by change in absorbance and hydrodynamic radius (R_h) with increasing temperature at 25μM in PBS. The thermal behavior correlates between the two methods.

The physical properties such as morphology and aggregation number were determined by SLS. A partial Zimm plot was constructed and the average weighted molecular weight was calculated from the y-intercept while the R_g was calculated from the slope of the linear fit. The aggregation number was calculated by dividing the Kc/R ratio extrapolated to scattering angle zero of the micelle by that of unimer. The dn/dc was assumed to be 0.186 as previously determined for proteins. However, in dividing the two Kc/R ratios (or M_w as determined for both unimer and micelle with dn/dc = 0.186), the dn/dc value inputted does not affect the calculated aggregation number.

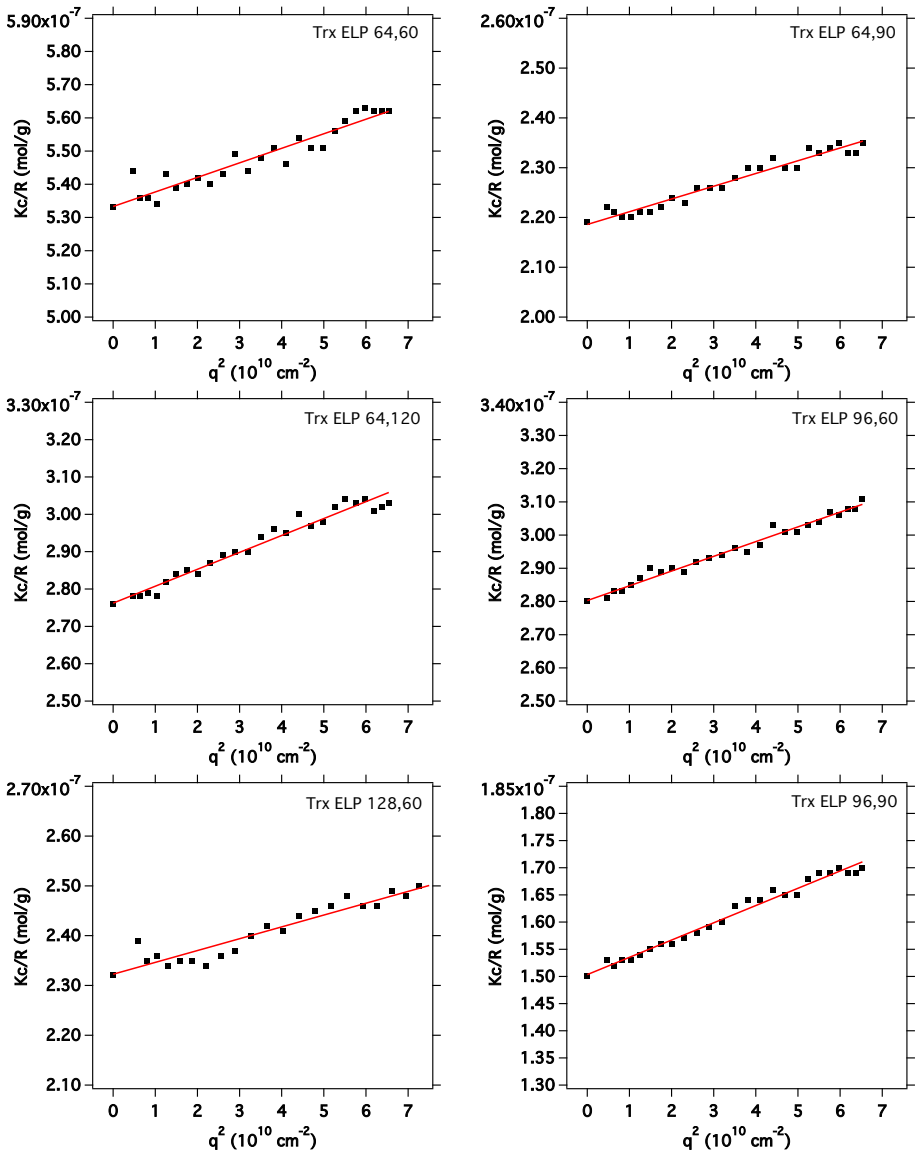

Figure 64: Zimm plots of Trx ELP$_{BCS}$ as determined by SLS. The weight average M_w was calculated from the y-intercept while R_g was determined from the slope of the linear fit.

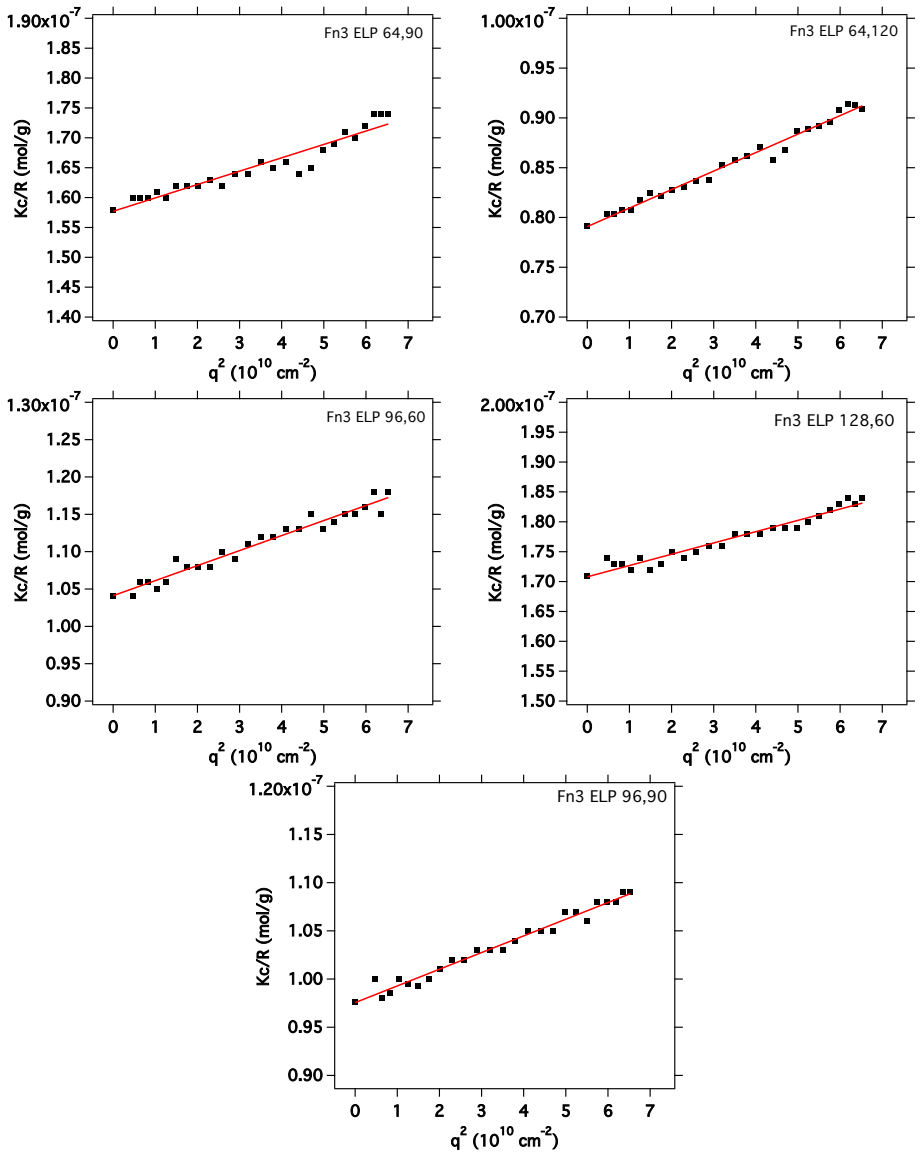

Figure 65: Zimm plots of Fn3 ELP$_{BC}$s as determined by SLS. The weight average M_w was calculated from the y-intercept while R_g was determined from the slope of the linear fit.

The apparent diffusion coefficient was measured for all samples to determine the change with scattering angle. A slope of zero indicates a spherical monodisperse particle. As can be seen in Figure 66 and Figure 67, for Trx ELP$_{BC}$ and Fn3 ELP$_{BC}$ the change in the apparent diffusion coefficient is not significant (< 10%). However, it is interesting to note that for all ELPs (whether diblock, monoblock, fused to a protein or not) the linear fit of the apparent diffusion coefficient versus scattering angle has a small negative slope.

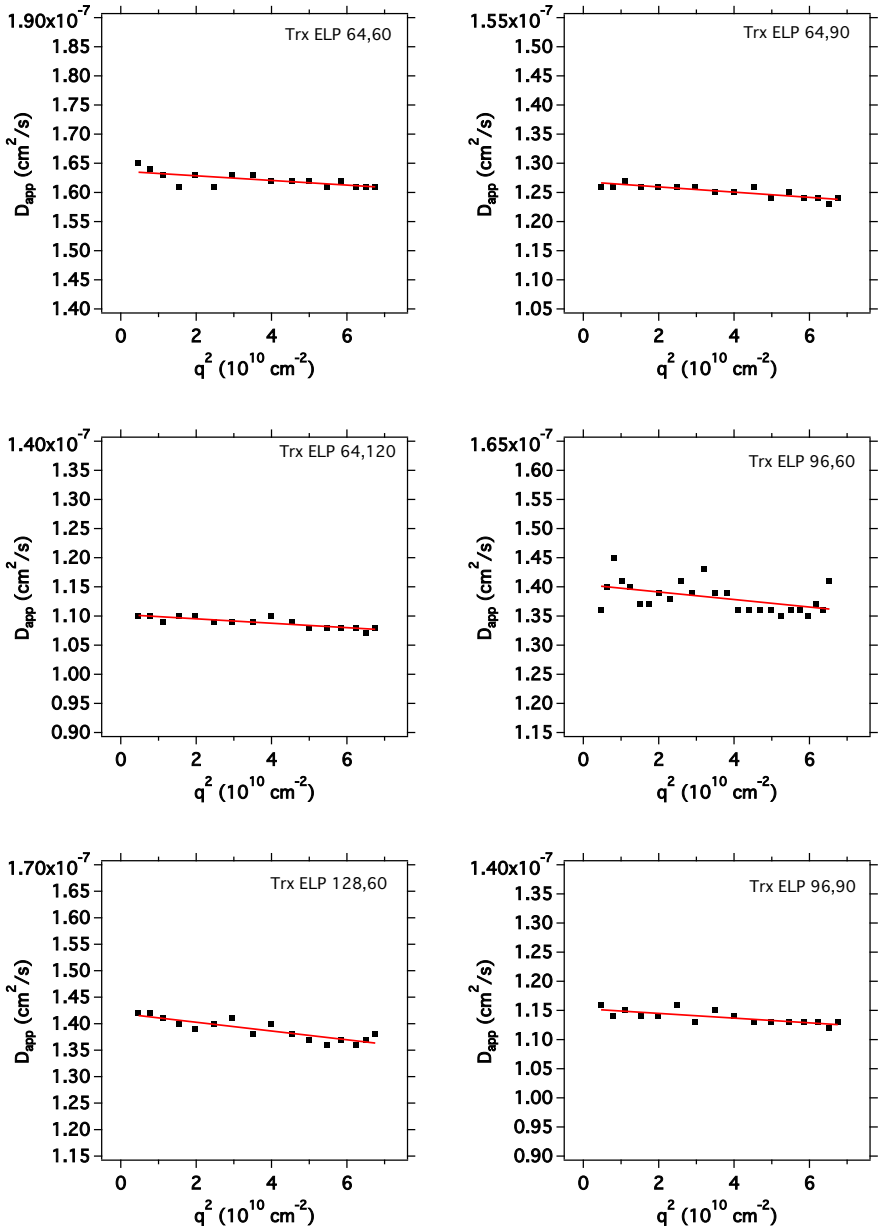

Figure 66: Change in the apparent diffusion coefficient with change in scattering wavevector as measured by DLS for Trx ELP$_{BCS}$. No angular dependence is observed indicating monodisperse spherical particles.

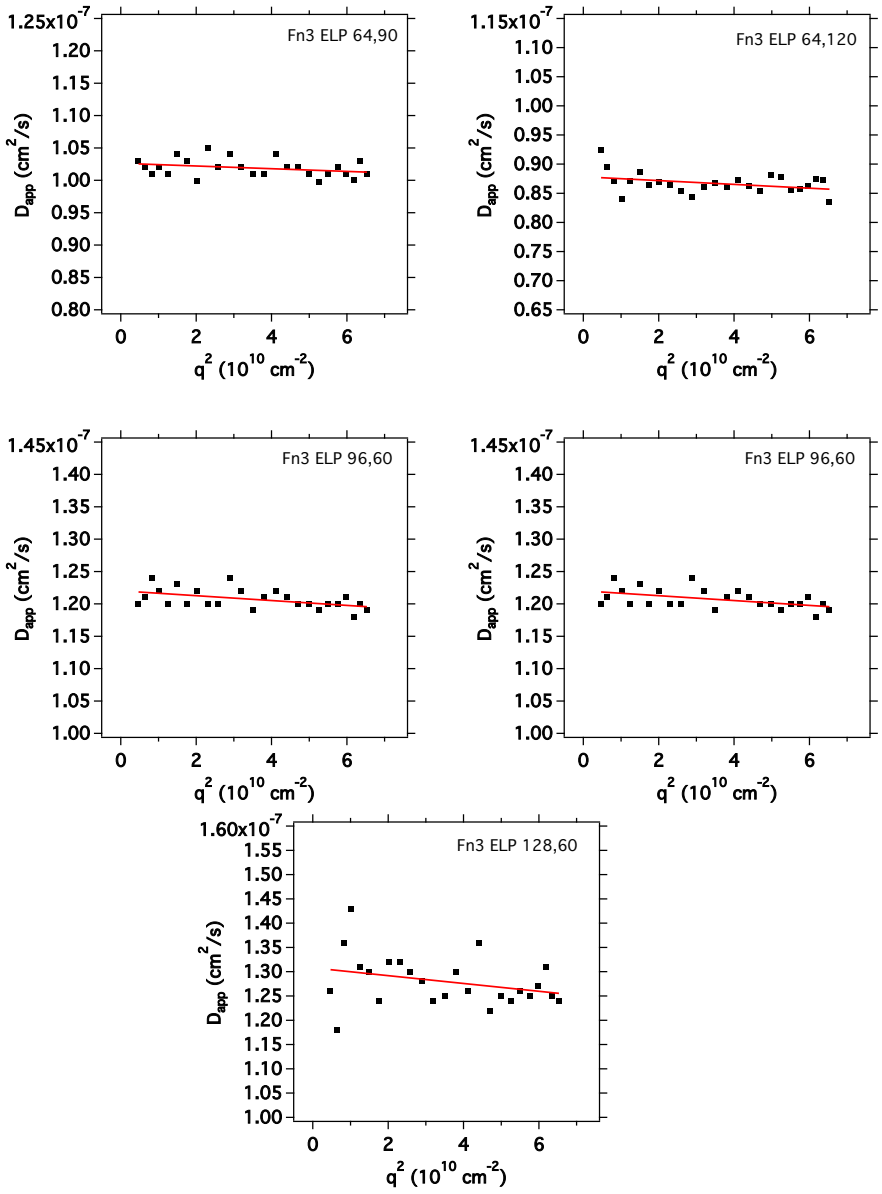

Figure 67: Change in the apparent diffusion coefficient with change in scattering wavevector as measured by DLS for Fn3 ELP$_{BC}$s. No angular dependence is observed indicating monodisperse spherical particles.

To investigate the interaction between the proteins and the hydrophobic block, we investigated the thermal behavior of the mixture of the hydrophobic ELP (ELP[V]-60) and a protein fused to the hydrophilic block ELP ([V$_1$:A$_8$:G$_7$]-96) (Figure 68). VHH

ELP[V_1:A_8:G_7]-96 and Fn3 ELP[V_1:A_8:G_7]-96 were investigated as both proteins are the same molecular weight and hydrophobicity but VHH disrupts the self-assembly behavior while Fn3 does not. As a control, the hydrophilic block ELP was mixed with the hydrophobic block ELP. As expected, each ELP transitioned separately and behaved as it would in a solution by itself. For the protein ELP[V_1:A_8:G_7]-96 fusions, Fn3 ELP[V_1:A_8:G_7]-96 was expected to transition separately from ELP[V]-60 as self-assembly is retained for Fn3 ELP 96,60 and the thermal behavior confirmed what was expected. However, VHH [V_1:A_8:G_7]-96 also transitioned separately from ELP[V]-60. This observation indicates that the interaction between VHH and the hydrophobic block is not strong enough to overcome the loss in entropy if VHH [V_1:A_8:G_7]-96 coprecipitates.

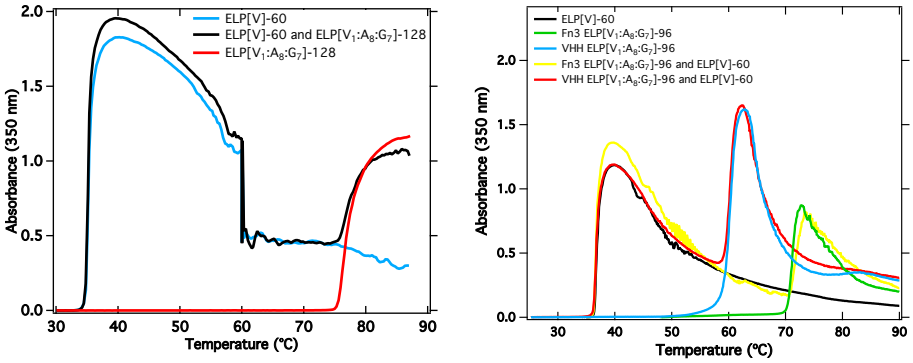

Figure 68: Left: thermal behavior of mixtures of monoblock hydrophilic and hydrophobic ELP that were combined to create an ELP$_{BC}$. The absorbance at 350 nm was measured for a sample of 0.5g/L ELP[V]-60 or 1g/L ELP[V_1:A_8:G_7]-128 or a mixture of both from 25 to 60 °C at a heating rate of 0.3°C/min then held at 60°C for 90 min then heated to 90°C at a heating rate of 1°C/min. Each block transitions separately and is not affected by the presence of the other block. Right: thermal behavior of mixtures of monoblock ELP[V]-60 and VHH ELP[V_1:A_8:G_7]-96 or Fn3 ELP[V_1:A_8:G_7]-96 fusions. The absorbance at 350 nm was measured for a sample of 10μM ELP[V]-60 or 12.5 μM protein ELP[V_1:A_8:G_7]-96 fusion or a mixture from at a heating rate of 0.3°C/min. Each block transitions separately and is not affected by the presence of the other block.

Appendix B

In this appendix, the SLS data for the new ELP$_{BCS}$ discussed in chapter 3 are detailed. A partial Zimm plot is constructed and the average weighted molecular weight was calculated from the y-intercept and the R_g was calculated from the slope of the linear fit (Figure 69). The dn/dc was assumed to be 0.186. The change in apparent diffusion coefficient with scattering angle (Figure 70) indicates spherical monodisperse particles as no significant slope is observed. However, as is consistent with previous observation a persistent small negative slope is present for all ELP samples.

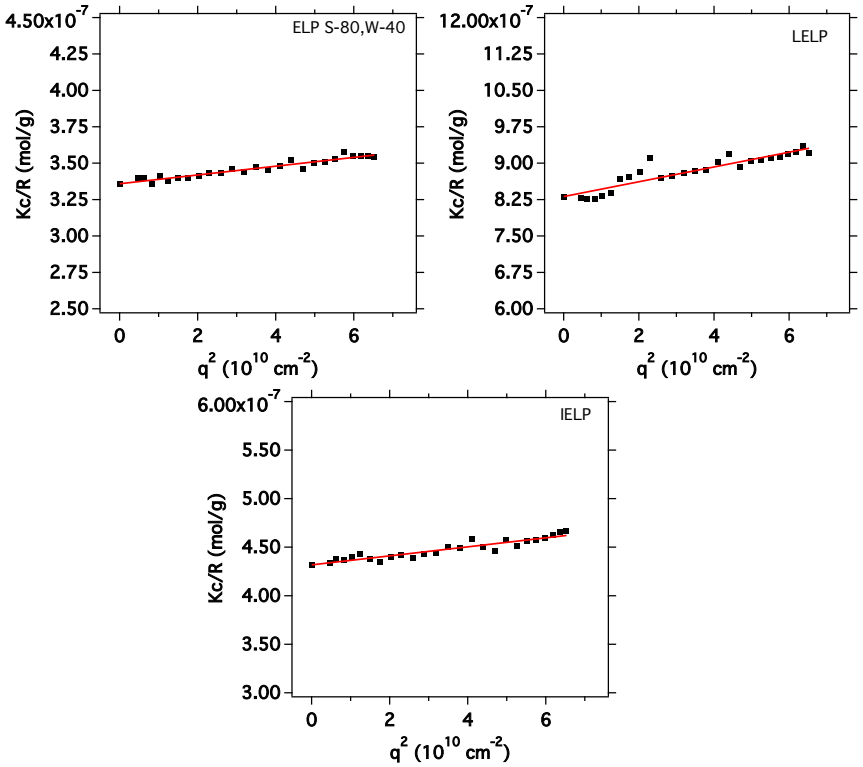

Figure 69: Zimm plots of new ELP$_{BCS}$ as determined by SLS. The weight average M_w was calculated from the y-intercept while R_g was determined from the slope of the linear fit.

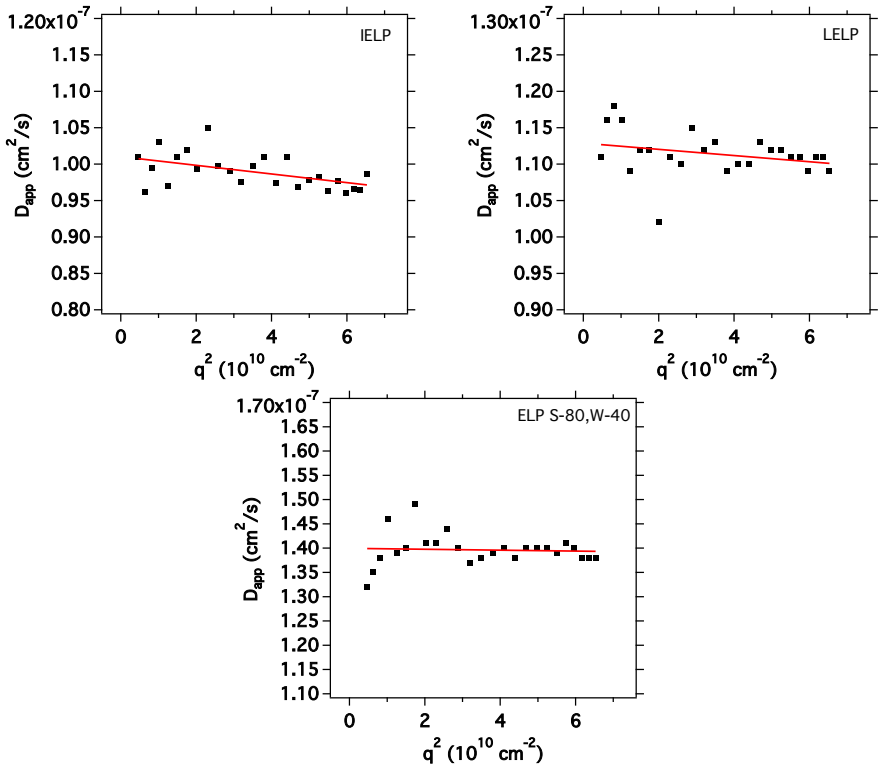

Figure 70: The figure shows the change in the apparent diffusion coefficient with change in scattering wavevector as measured by DLS for new ELP$_{BC}$. No angular dependence is observed indicating monodisperse spherical particles.

The four proteins were fused to LELP and the thermal behavior of the four fusions was determined (Figure 71). The protein LELP fusions behave similarly to protein WELP fusions. Trx LELP and Fn3 LELP are observed to self-assemble as indicated by similar thermal behavior to LELP. VHH LELP disrupts self-assembly and transitions around the CMT of LELP while BFP LELP again displays a complex behavior in which self-assembly is observed but a higher absorbance than that of LELP in the micelle-forming temperature range indicates the presence of BFP LELP aggregates as well as micelles.

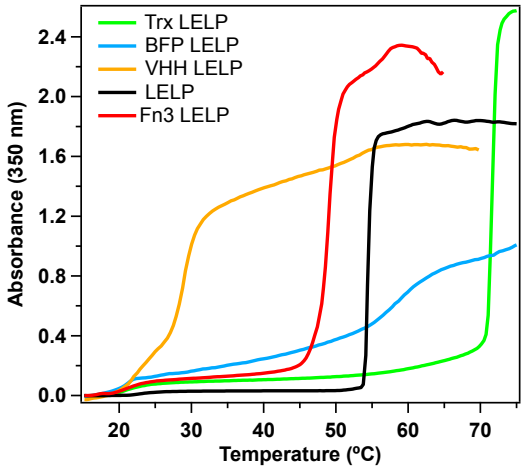

Figure 71: Thermal behavior of protein LELP fusions. The absorbance at 350 nm was measured for a 25 μM sample while heating at a rate of 1°C/min. The effect of the protein on LELP is similar to that on WELP. Trx and Fn3 do not disrupt self-assembly while VHH causes LELP to transition around its CMT and BFP shows an intermediate behavior of displaying self-assembly behavior but not as well defined as LELP.

BFP WELP thermal behavior was monitored when free WELP is added to the solution. As can be observed in Figure 72, the mixture displays an intermediate behavior between WELP and BFP WELP. While an initial increase to an O.D. of 0.6 is observed for both BFP WELP and the mixture, the presence of the free WELP with BFP WELP causes a drop in absorbance for the mixture at 30°C. This drop could be due to incorporation of BFP WELP into WELP micelles thus causing formation of fewer aggregates. However, the absorbance remains larger than the WELP absorbance between 30 °C and 54 °C and the sharper transition at the micelle-to-aggregate transition temperature is broad for the mixture. These observations indicate that some aggregates are still present and not all BFP WELP unimers have been incorporated into WELP micelles. Therefore, including

free WELP does help incorporate BFP WELP into micelles but does not completely alter its self-assembly behavior.

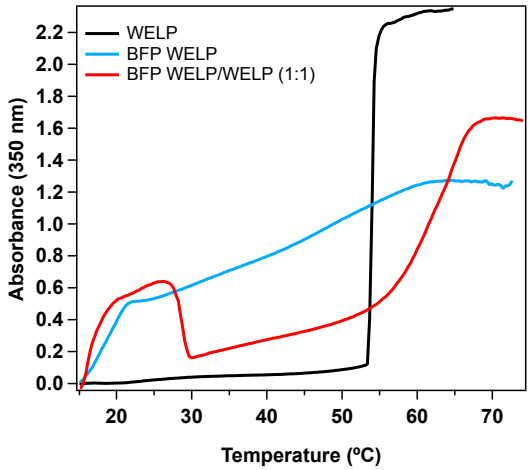

Figure 72: Thermal behavior of WELP, BFP WELP or a 1:1 mixture of WELP and BFP WELP. The absorbance at 350 nm was measured at 25 μM in PBS while heating at a rate of 1°C/min.

Appendix C

To determine the surface tension of the hydrophobic block, the transition temperature was determined for a wide range of concentrations. ELP[V] with 60, 90 and 120 pentapeptides were expressed and purified as previously described. The samples were lyophilized overnight and solutions of concentrations ranging from 0.002 g/L to 316 g/L were prepared. More accurate concentrations are obtained through preparing samples from lyophilized material (as opposed to absorbance measurements). The transition temperature was determined by measuring absorbance at 350 nm at a heating rate of 1°C/min. The heating rate does not affect the transition temperature as no difference was observed between the transition temperatures for two concentrations (25 μM and 5.5 mM) at two heating rates (0.1°C/min and 1°C/min). The transition temperature was determined as the temperature at which the tangent through the steepest part of the absorbance versus temperature curve intercepts the x-axis.

Zimm plots were obtained by measuring the average scattering intensity over a range of scattering angles and concentrations. ELP[V_1:A_8:G_7]-96 was expressed and purified as previously described. The purified ELP was dialyzed overnight against water to remove trace salts and the sample was lyophilized overnight. An ELP sample was prepared at a concentration of 5 g/L in PBS. Additional concentrations (1, 2, 3, and 4 g/L) were all prepared from the 5 g/L sample. All five samples were filtered through an

Anotop 10 Whatman 20 nm filter directly into a 10 mm borosilicate glass tube that has been prewashed with filtered ethanol (0.22 μm cellulose acetate filter).

SLS measurements were performed using an ALV/ CGS-3 goniometer system (ALV, Langen, Germany). A standard calibration measurement and a solvent (PSB) measurement were obtained at all measurement temperatures (23, 30, 35, 40 and 45°C). The average scattering intensity for each of the five concentrations was measured at the five temperatures at a scattering angle range of 30° to 150° in 5° steps in 3 runs each 15 seconds at each angle (Figure 73).

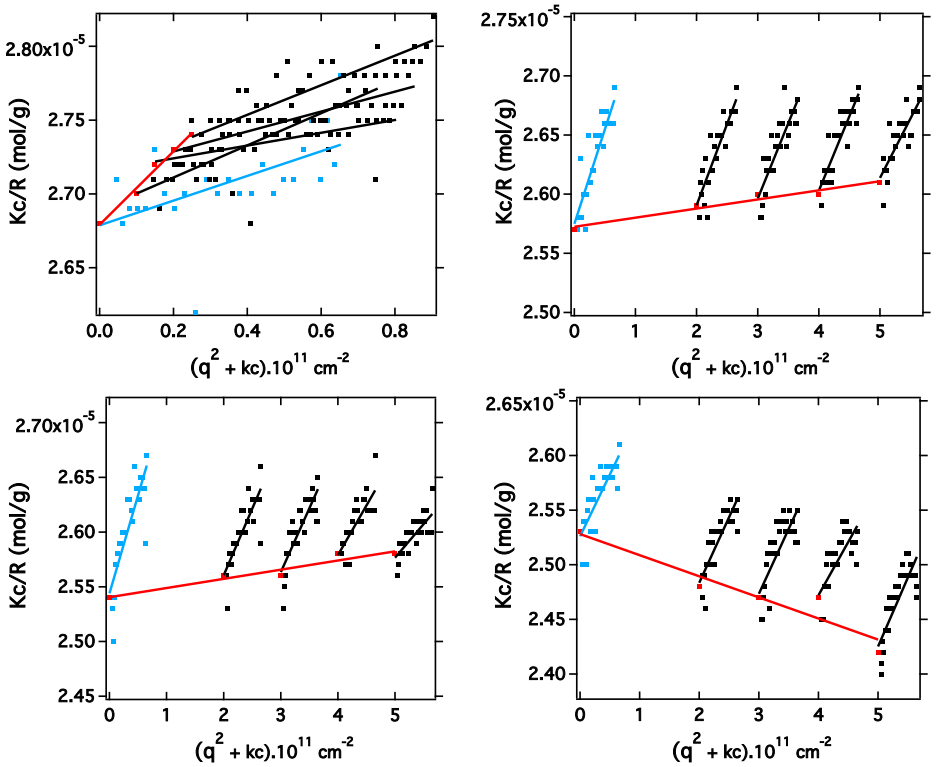

Figure 73: Zimm plots of ELP[V_1:A_8:G_7]-96 at temperatures 30°C (top-left), 35°C (top-right), 40°C (bottom-left), and 45°C (bottom-right). The average intensity was measured at four concentrations (2, 3, 4, and 5 g/L) at scattering angles between 30° and 150°. Kc/R was extrapolated to concentration zero (blue) and scattering angle 0°

(red). M_w was determined from the y-intercept of the blue linear fit and A_2 was determined from the slope of the red linear fit. The arbitrary constant k value used for Zimm plot at 30°C is 50 while for the rest of the temperatures the k value was 1000.

Aggregation numbers for all six ELP_{BC}s were determined for all temperatures at which spherical micelles are formed. As described above, the ELP_{BC}s were lyophilized after purification and solutions of 25 μM in PBS were filtered into precleaned tubes. The samples were measure at room temperature while in unimer state. The samples were then heated above the CMT and measurements were taken at 1°C intervals up to the first temperature at which the apparent diffusion coefficient versus scattering angle slope is positive. The measurements at each temperature were taken between scattering angles of 30° to 150° in 3 runs each 15 seconds at each angle. The aggregation number was calculated by taking the ratio of extrapolated Kc/R to scattering angle zero for both unimer and micelle measurements. The aggregation numbers were obtained from partial Zimm plots (i.e. one concentration) as A_2 values of the ELP_{BC} are not significant as determined from the complete Zimm plot (Figure 74).

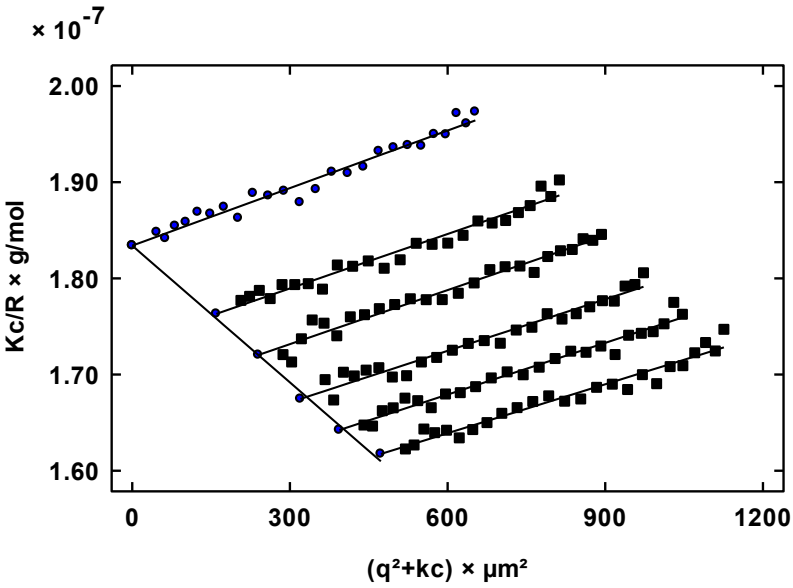

Figure 74: Zimm plot of ELP 96,60 for concentrations (25, 37.5, 50, 62.5, 75 µM) at 44.5 °C. A_2 is -2.4x10^{-9} mol.L/g^2; the micelles experience a small insignificant attraction.

Cryo-TEM images were obtained for ELP 64,90 and ELP 64,120 at 44 °C. A this temperature, these two diblocks are expected to self-assemble into two population of spherical micelles as well as larger nanoscale aggregates (~100 nm) as determined by DLS. The two ELP$_{BC}$ were expressed, purified and lyophilized and a solution of 50 µM in PBS was prepared. The samples were incubated in a heat block at 44 °C before preparing the cryo-TEM sample. In addition, the carbon grids were heated to maintain the temperature during preparation of the sample. The samples were imaged using a JEOL TEM at 80 keV as ELP samples are of low contrast. As can be seen from the representative images below of the two ELP$_{BC}$, larger nanoscale aggregates as well as small spherical micelles are present (Figure 75 and Figure 76).

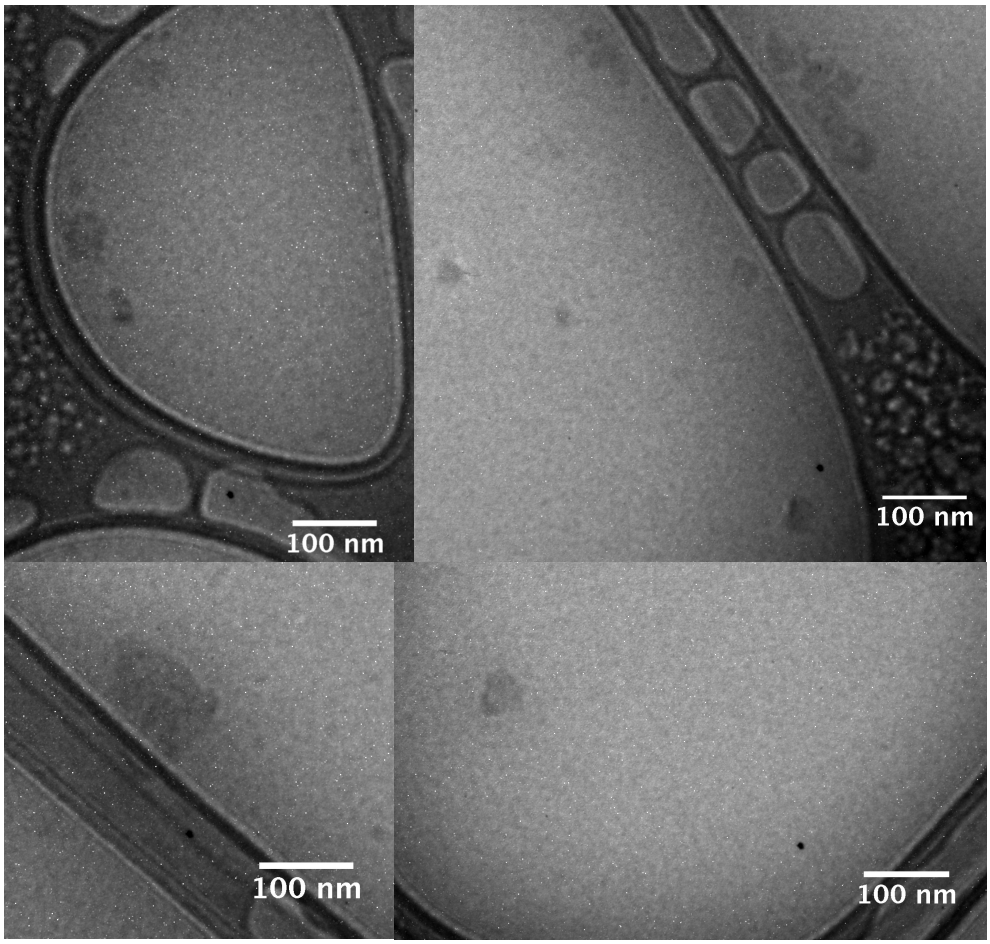

Figure 75: Cryo-TEM images of ELP 64,90 at 44 °C. As can be seen by the four representative images, spherical micelles are present as well as larger nano-scaled aggregates with no defined morphology.

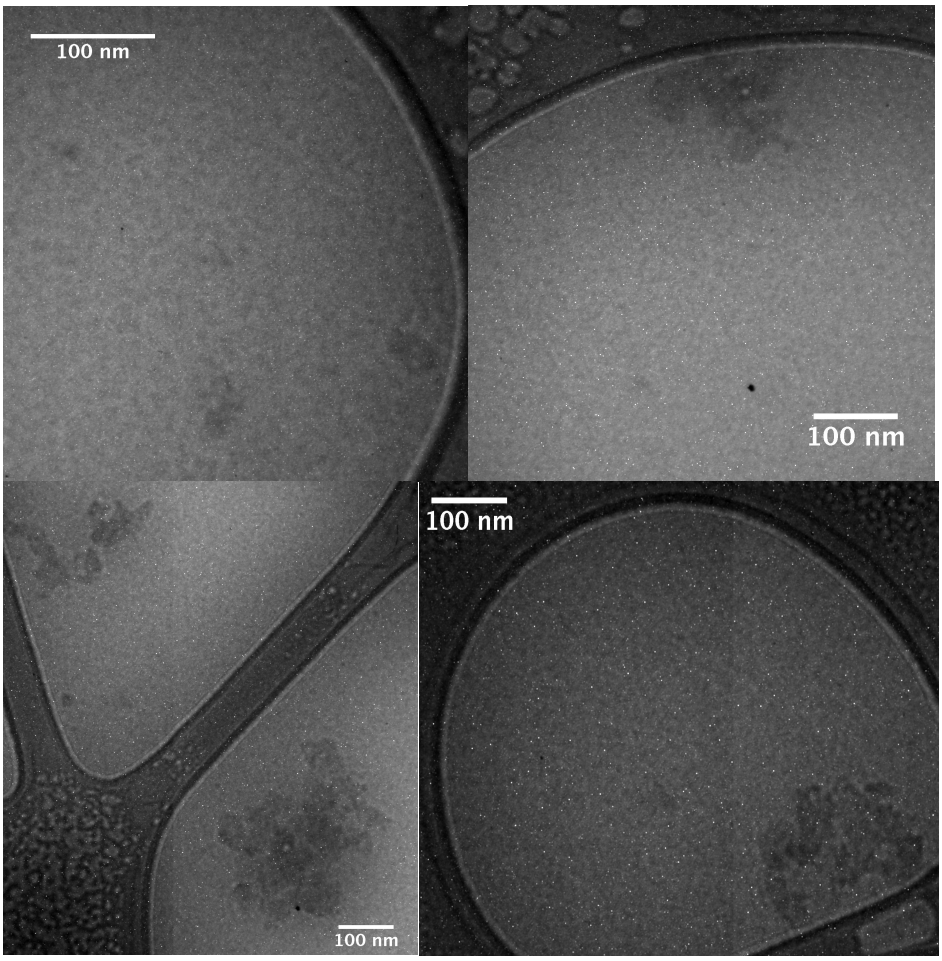

Figure 76: Cryo-TEM images of ELP 64,120 at 44 °C. As can be seen by the four representative images, spherical micelles are present as well as larger nano-scaled aggregates with no defined morphology.

The dn/dc of ELP[V_1:A_8:G_7]-96 was measured using an Optilab® T-rEX™ (Wyatt instruments, Santa Barbara, CA). The instrument was precleaned and prepared for measurements by injecting the series of solvents: ethanol, water and PBS. The instrument was set to the desired temperatures and allowed to equilibrate. The dn/dc was determined at 25, 35, 40, and 45 °C. A sample of 2 g/L in PBS was prepared from

lyophilized ELP[V_1:A_8:G_7]-96 and samples of concentrations 0.125, 0.25, 0.5, and 1 g/L were all prepared from the 2 g/L sample. A volume of approximately 1 mL of each sample was injected into the instrument in the order of increasing concentration. Each injection was followed by a minimum of 3 mL of PBS to ensure complete clearance of the previous concentration. dn/dc was determined from the slope of the linear fit of the differential refractive index versus concentration (Figure 77).

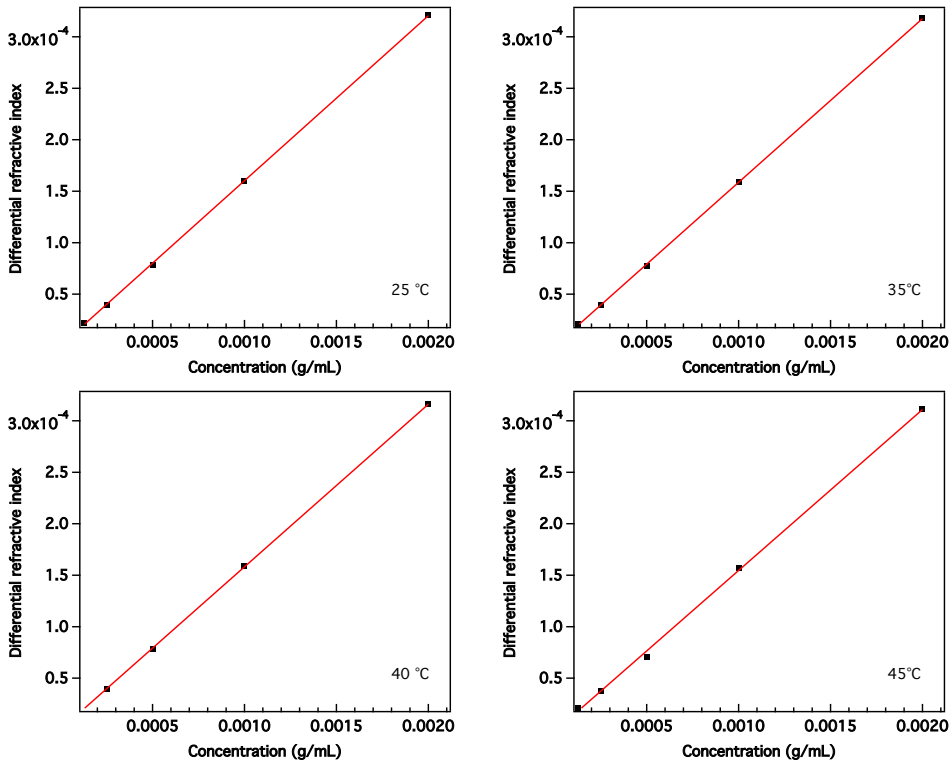

Figure 77: Measurement of dn/dc for ELP[V_1:A_8:G_7]-96 at temperatures 25, 35, 40 and 45 °C. The differential refractive index was measured at concentrations 0.125, 0.25, 0.5,1 and 2 g/L and dn/dc was determined from the slope.

To ensure that the micelles are thermodynamically stable at the measured temperatures, the hydrodynamic radius was measured while heating and cooling the

sample (Figure 78). No significant difference is observed between the measured radii while heating and cooling indicating that these structures are not kinetically driven but are thermodynamically stable.

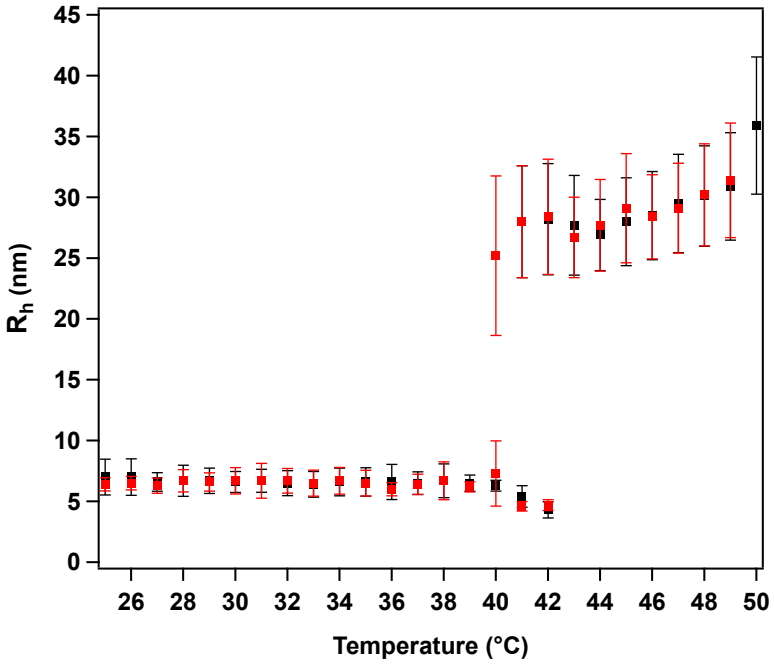

Figure 78: Hydrodynamic radius of ELP 96,60 as measured by DLS at a concentration of 25 μM in PBS while heating (black) and cooling (red). The measured radii are reproducible and match while heating and cooling sample indicating that the micelles are thermodynamically stable and the measured physical properties are not kinetically controlled.

References

1. Vrhovski, B.; Weiss, A. S., Biochemistry of Tropoelastin. *Eur J Biochem* **1998,** *258* (1), 1-18.

2. Urry, D. W.; Gowda, D. C.; Parker, T. M.; Luan, C. H.; Reid, M. C.; Harris, C. M.; Pattanaik, A.; Harris, R. D., Hydrophobicity Scale for Proteins Based on Inverse Temperature Transitions. *Biopolymers* **1992,** *32* (9), 1243-1250.

3. Meyer, D. E.; Chilkoti, A., Quantification of the Effects of Chain Length and Concentration on the Thermal Behavior of Elastin-Like Polypeptides. *Biomacromolecules* **2004,** *5* (3), 846-851.

4. Meyer, D. E.; Chilkoti, A., Genetically Encoded Synthesis of Protein-Based Polymers with Precisely Specified Molecular Weight and Sequence by Recursive Directional Ligation: Examples from the Elastin-Like Polypeptide System. *Biomacromolecules* **2002,** *3* (2), 357-367.

5. McDaniel, J. R.; Mackay, J. A.; Quiroz, F. G.; Chilkoti, A., Recursive Directional Ligation by Plasmid Reconstruction Allows Rapid and Seamless Cloning of Oligomeric Genes. *Biomacromolecules* **2010,** *11*, 944-952.

6. Asai, D.; Xu, D.; Liu, W.; Garcia Quiroz, F.; Callahan, D. J.; Zalutsky, M. R.; Craig, S. L.; Chilkoti, A., Protein Polymer Hydrogels by in Situ, Rapid and Reversible Self-Gelation. *Biomaterials* **2012,** *33* (21), 5451-5458.

7. MacKay, J. A.; Chen, M.; McDaniel, J. R.; Liu, W.; Simnick, A. J.; Chilkoti, A., Self-Assembling Chimeric Polypeptide-Doxorubicin Conjugate Nanoparticles That Abolish Tumours after a Single Injection. *Nat Mater* **2009,** *8* (12), 993-999.

8. Dreher, M. R.; Simnick, A. J.; Fischer, K.; Smith, R. J.; Patel, A.; Schmidt, M.; Chilkoti, A., Temperature Triggered Self-Assembly of Polypeptides into Multivalent Spherical Micelles. *J Am Chem Soc* **2008,** *130* (2), 687-694.

9. Kim, W.; Thevenot, J.; Ibarboure, E.; Lecommandoux, S.; Chaikof, E. L., Self-Assembly of Thermally Responsive Amphiphilic Diblock Copolypeptides into Spherical Micellar Nanoparticles. *Angew Chem Int Edit* **2010,** *49* (25), 4257-4260.

10. Massodi, I.; Bidwell, G. L.; Raucher, D., Evaluation of Cell Penetrating Peptides Fused to Elastin-Like Polypeptide for Drug Delivery. *J Control Release* **2005,** *108* (2-3), 396-408.

11. Macewan, S. R.; Chilkoti, A., Digital Switching of Local Arginine Density in a Genetically Encoded Self-Assembled Polypeptide Nanoparticle Controls Cellular Uptake. *Nano Lett* **2012,** *12* (6), 3322-3328.

12. Prieto, S.; Shkilnyy, A.; Rumplasch, C.; Ribeiro, A.; Arias, F. J.; Rodriguez-Cabello, J. C.; Taubert, A., Biomimetic Calcium Phosphate Mineralization with Multifunctional Elastin-Like Recombinamers. *Biomacromolecules* **2011,** *12* (5), 1480-1486.

13. Hassouneh, W.; Nunalee, M. L.; Shelton, M. C.; Chilkoti, A., Calcium Binding Peptide Motifs from Calmodulin Confer Divalent Ion Selectivity to Elastin-Like Polypeptides. *Biomacromolecules* **2013,** *14* (7), 2347-2353.

14. Rubinstein, M.; Colby, R., *Polymer Physics*. Oxford University Press: 2003.

15. Urry, D. W.; Trapane, T. L.; Prasad, K. U., Phase-Structure Transitions of the Elastin Polypentapeptide-Water System within the Framework of Composition-Temperature Studies. *Biopolymers* **1985,** *24* (12), 2345-2356.

16. Urry, D. W., The Change in Gibbs Free Energy for Hydrophobic Association: Derivation and Evaluation by Means of Inverse Temperature Transitions. *Chemical Physics Letters* **2004,** *399* (1,Äì3), 177-183.

17. Zhang, Y.; Furyk, S.; Sagle, L. B.; Cho, Y.; Bergbreiter, D. E.; Cremer, P. S., Effects of Hofmeister Anions on the Lcst of Pnipam as a Function of Molecular Weight. *J. Phys. Chem. C* **2007,** *111* (25), 8916-8924.

18. Zhang, Y.; Furyk, S.; Bergbreiter, D. E.; Cremer, P. S., Specific Ion Effects on the Water Solubility of Macromolecules: Pnipam and the Hofmeister Series. *J. Am. Chem. Soc.* **2005,** *127* (41), 14505-14510.

19. Cho, Y.; Zhang, Y.; Christensen, T.; Sagle, L. B.; Chilkoti, A.; Cremer, P. S., Effects of Hofmeister Anions on the Phase Transition Temperature of Elastin-Like Polypeptides. *J. Phys. Chem. B* **2008,** *112*, 13765-13771.

20. Hofmeister, F., Zur Lehre Von Der Wirkung Der Salze. *Archiv f. experiment. Pathol. u. Pharmakol* **1888,** *25* (1), 1-30.

21. Sciortino, F.; Urry, D. W.; Palma, M. U.; Prasad, K. U., Self-Assembly of a Bioelastomeric Structure: Solution Dynamics and the Spinodal and Coacervation Lines. *Biopolymers* **1990,** *29* (10-11), 1401-1407.

22. Sciortino, F.; Prasad, K. U.; Urry, D. W.; Palma, M. U., Self-Assembly of Bioelastomeric Structures from Solutions: Mean-Field Critical Behavior and Flory-Huggins Free Energy of Interactions. *Biopolymers* **1993,** *33* (5), 743-752.

23. Fluegel, S.; Fischer, K.; McDaniel, J. R.; Chilkoti, A.; Schmidt, M., Chain Stiffness of Elastin-Like Polypeptides. *Biomacromolecules* **2010**.

24. Chow, D.; Nunalee, M. L.; Lim, D. W.; Simnick, A. J.; Chilkoti, A., Peptide-Based Biopolymers in Biomedicine and Biotechnology. *Mater Sci Eng R Rep* **2008,** *62* (4), 125-155.

25. Bellomo, E. G.; Wyrsta, M. D.; Pakstis, L.; Pochan, D. J.; Deming, T. J., Stimuli-Responsive Polypeptide Vesicles by Conformation-Specific Assembly. *Nat Mater* **2004,** *3* (4), 244-248.

26. Holowka, E. P.; Sun, V. Z.; Kamei, D. T.; Deming, T. J., Polyarginine Segments in Block Copolypeptides Drive Both Vesicular Assembly and Intracellular Delivery. *Nat Mater* **2007,** *6* (1), 52-57.

27. Holowka, E. P.; Pochan, D. J.; Deming, T. J., Charged Polypeptide Vesicles with Controllable Diameter. *Journal of the American Chemical Society* **2005,** *127* (35), 12423-12428.

28. Potekhin, S. A.; Melnik, T. N.; Popov, V.; Lanina, N. F.; Vazina, A. A.; Rigler, P.; Verdini, A. S.; Corradin, G.; Kajava, A. V., De Novo Design of Fibrils Made of Short Alpha-Helical Coiled Coil Peptides. *Chem Biol* **2001,** *8* (11), 1025-1032.

29. Pandya, M. J.; Spooner, G. M.; Sunde, M.; Thorpe, J. R.; Rodger, A.; Woolfson, D. N., Sticky-End Assembly of a Designed Peptide Fiber Provides Insight into Protein Fibrillogenesis. *Biochemistry* **2000,** *39* (30), 8728-8734.

30. Zimenkov, Y.; Conticello, V. P.; Guo, L.; Thiyagarajan, P., Rational Design of a Nanoscale Helical Scaffold Derived from Self-Assembly of a Dimeric Coiled Coil Motif. *Tetrahedron* **2004,** *60* (34), 7237-7246.

31. Santoso, S.; Hwang, W.; Hartman, H.; Zhang, S., Self-Assembly of Surfactant-Like Peptides with Variable Glycine Tails to Form Nanotubes and Nanovesicles. *Nano Lett* **2002,** *2* (7), 687-691.

32. von Maltzahn, G.; Vauthey, S.; Santoso, S.; Zhang, S., Positively Charged Surfactant-Like Peptides Self-Assemble into Nanostructures. *Langmuir* **2003,** *19* (10), 4332-4337.

33. Zhao, X.; Pan, F.; Xu, H.; Yaseen, M.; Shan, H.; Hauser, C. A.; Zhang, S.; Lu, J. R., Molecular Self-Assembly and Applications of Designer Peptide Amphiphiles. *Chem Soc Rev* **2010,** *39* (9), 3480-3498.

34. Li, L.; Charati, M. B.; Kiick, K. L., Elastomeric Polypeptide-Based Biomaterials. *J Polym Sci A Polym Chem* **2010,** *1* (8), 1160-1170.

35. Megeed, Z.; Cappello, J.; Ghandehari, H., Genetically Engineered Silk-Elastinlike Protein Polymers for Controlled Drug Delivery. *Adv Drug Deliv Rev* **2002,** *54* (8), 1075-1091.

36. Nagarsekar, A.; Crissman, J.; Crissman, M.; Ferrari, F.; Cappello, J.; Ghandehari, H., Genetic Engineering of Stimuli-Sensitive Silkelastin-Like Protein Block Copolymers. *Biomacromolecules* **2003,** *4* (3), 602-607.

37. Cappello, J.; Crissman, J. W.; Crissman, M.; Ferrari, F. A.; Textor, G.; Wallis, O.; Whitledge, J. R.; Zhou, X.; Burman, D.; Aukerman, L.; Stedronsky, E. R., In-Situ Self-Assembling Protein Polymer Gel Systems for Administration, Delivery, and Release of Drugs. *Journal of controlled release : official journal of the Controlled Release Society* **1998,** *53* (1-3), 105-117.

38. Megeed, Z.; Haider, M.; Li, D.; O'Malley, B. W., Jr.; Cappello, J.; Ghandehari, H., In Vitro and in Vivo Evaluation of Recombinant Silk-Elastinlike Hydrogels for Cancer Gene Therapy. *Journal of controlled release : official journal of the Controlled Release Society* **2004,** *94* (2-3), 433-445.

39. Charati, M. B.; Ifkovits, J. L.; Burdick, J. A.; Linhardt, J. G.; Kiick, K. L., Hydrophilic Elastomeric Biomaterials Based on Resilin-Like Polypeptides. *Soft Matter* **2009,** *5* (18), 3412-3416.

40. Shamji, M. F.; Betre, H.; Kraus, V. B.; Chen, J.; Chilkoti, A.; Pichika, R.; Masuda, K.; Setton, L. A., Development and Characterization of a Fusion Protein between Thermally Responsive Elastin-Like Polypeptide and Interleukin-1 Receptor Antagonist: Sustained Release of a Local Antiinflammatory Therapeutic. *Arthritis Rheum* **2007,** *56* (11), 3650-3661.

41. Shamji, M. F.; Chen, J.; Friedman, A. H.; Richardson, W. J.; Chilkoti, A.; Setton, L. A., Synthesis and Characterization of a Thermally-Responsive Tumor Necrosis Factor Antagonist. *Journal of controlled release : official journal of the Controlled Release Society* **2008,** *129* (3), 179-186.

42. Sallach, R. E.; Cui, W.; Wen, J.; Martinez, A.; Conticello, V. P.; Chaikof, E. L., Elastin-Mimetic Protein Polymers Capable of Physical and Chemical Crosslinking. *Biomaterials* **2009,** *30* (3), 409-422.

43. Trabbic-Carlson, K.; Setton, L. A.; Chilkoti, A., Swelling and Mechanical Behaviors of Chemically Cross-Linked Hydrogels of Elastin-Like Polypeptides. *Biomacromolecules* **2003,** *4* (3), 572-580.

44. Sallach, R. E.; Wei, M.; Biswas, N.; Conticello, V. P.; Lecommandoux, S.; Dluhy, R. A.; Chaikof, E. L., Micelle Density Regulated by a Reversible Switch of Protein Secondary Structure. *Journal of the American Chemical Society* **2006,** *128* (36), 12014-12019.

45. Callahan, D. J.; Liu, W.; Li, X.; Dreher, M. R.; Hassouneh, W.; Kim, M.; Marszalek, P.; Chilkoti, A., Triple Stimulus-Responsive Polypeptide Nanoparticles That Enhance Intratumoral Spatial Distribution. *Nano Lett* **2012,** *12* (4), 2165-2170.

46. Chen, T. H.; Bae, Y.; Furgeson, D. Y., Intelligent Biosynthetic Nanobiomaterials (Ibns) for Hyperthermic Gene Delivery. *Pharm Res* **2008,** *25* (3), 683-691.

47. Strzegowski, L. A.; Martinez, M. B.; Gowda, D. C.; Urry, D. W.; Tirrell, D. A., Photomodulation of the Inverse Temperature Transition of a Modified Elastin Poly(Pentapeptide). *Journal of the American Chemical Society* **1994,** *116* (2), 813-814.

48. Lee, T. A. T.; Cooper, A.; Apkarian, R. P.; Conticello, V. P., Thermo-Reversible Self-Assembly of Nanoparticles Derived from Elastin-Mimetic Polypeptides. *Advanced Materials* **2000,** *12* (15), 1105-1110.

49. Kim, W.; Thévenot, J.; Ibarboure, E.; Lecommandoux, S.; Chaikof, E. L., Self-Assembly of Thermally Responsive Amphiphilic Diblock Copolypeptides into Spherical Micellar Nanoparticles. *Angewandte Chemie International Edition* **2010,** *49* (25), 4257-4260.

50. Martin, L.; Castro, E.; Ribeiro, A.; Alonso, M.; Rodriguez-Cabello, J. C., Temperature-Triggered Self-Assembly of Elastin-Like Block Co-Recombinamers:The Controlled Formation of Micelles and Vesicles in an Aqueous Medium. *Biomacromolecules* **2012,** *13* (2), 293-298.

51. Ghoorchian, A.; Holland, N. B., Molecular Architecture Influences the Thermally Induced Aggregation Behavior of Elastin-Like Polypeptides. *Biomacromolecules* **2011,** *12* (11), 4022-4029.

52. Ghoorchian, A.; Cole, J. T.; Holland, N. B., Thermoreversible Micelle Formation Using a Three-Armed Star Elastin-Like Polypeptide. *Macromolecules* **2010,** *43* (9), 4340-4345.

53. Fujita, Y.; Mie, M.; Kobatake, E., Construction of Nanoscale Protein Particle Using Temperature-Sensitive Elastin-Like Peptide and Polyaspartic Acid Chain. *Biomaterials* **2009,** *30* (20), 3450-3457.

54. Le, D. H. T.; Hanamura, R.; Pham, D.-H.; Kato, M.; Tirrell, D. A.; Okubo, T.; Sugawara-Narutaki, A., Self-Assembly of Elastin-Mimetic Double Hydrophobic Polypeptides. *Biomacromolecules* **2013,** *14* (4), 1028-1034.

55. Simnick, A. J.; Valencia, C. A.; Liu, R.; Chilkoti, A., Morphing Low-Affinity Ligands into High-Avidity Nanoparticles by Thermally Triggered Self-Assembly of a Genetically Encoded Polymer. *ACS Nano* **2010,** *4* (4), 2217-2227.

56. Davis, M. E.; Chen, Z. G.; Shin, D. M., Nanoparticle Therapeutics: An Emerging Treatment Modality for Cancer. *Nat Rev Drug Discov* **2008,** *7* (9), 771-782.

57. Peer, D.; Karp, J. M.; Hong, S.; Farokhzad, O. C.; Margalit, R.; Langer, R., Nanocarriers as an Emerging Platform for Cancer Therapy. *Nat Nanotechnol* **2007,** *2* (12), 751-760.

58. Ruoslahti, E.; Bhatia, S. N.; Sailor, M. J., Targeting of Drugs and Nanoparticles to Tumors. *J Cell Biol 188* (6), 759-768.

59. Sutton, D.; Nasongkla, N.; Blanco, E.; Gao, J., Functionalized Micellar Systems for Cancer Targeted Drug Delivery. *Pharm Res* **2007,** *24* (6), 1029-1046.

60. Yu, B.; Tai, H. C.; Xue, W.; Lee, L. J.; Lee, R. J., Receptor-Targeted Nanocarriers for Therapeutic Delivery to Cancer. *Mol Membr Biol* **2010,** *27* (7), 286-298.

61. Doherty, G. J.; McMahon, H. T., Mechanisms of Endocytosis. *Annu Rev Biochem* **2009,** *78*, 857-902.

62. Wadia, J. S.; Stan, R. V.; Dowdy, S. F., Transducible Tat-Ha Fusogenic Peptide Enhances Escape of Tat-Fusion Proteins after Lipid Raft Macropinocytosis. *Nat Med* **2004,** *10* (3), 310-315.

63. Gabrielson, N. P.; Pack, D. W., Efficient Polyethylenimine-Mediated Gene Delivery Proceeds Via a Caveolar Pathway in Hela Cells. *J Control Release* **2009,** *136* (1), 54-61.

64. Kerr, M. C.; Teasdale, R. D., Defining Macropinocytosis. *Traffic* **2009,** *10* (4), 364-371.

65. Mammen, M.; Choi, S.-K.; Whitesides, G. M., Polyvalent Interactions in Biological Systems: Implications for Design and Use of Multivalent Ligands and Inhibitors. *Angewandte Chemie International Edition* **1998,** *37* (20), 2754-2794.

66. Zhou, Y.; Drummond, D. C.; Zou, H.; Hayes, M. E.; Adams, G. P.; Kirpotin, D. B.; Marks, J. D., Impact of Single-Chain Fv Antibody Fragment Affinity on Nanoparticle Targeting of Epidermal Growth Factor Receptor-Expressing Tumor Cells. *J Mol Biol* **2007,** *371* (4), 934-947.

67. Reulen, S. W.; Dankers, P. Y.; Bomans, P. H.; Meijer, E. W.; Merkx, M., Collagen Targeting Using Protein-Functionalized Micelles: The Strength of Multiple Weak Interactions. *Journal of the American Chemical Society* **2009,** *131* (21), 7304-7312.

68. Jule, E.; Nagasaki, Y.; Kataoka, K., Lactose-Installed Poly(Ethylene Glycol)-Poly(D,L-Lactide) Block Copolymer Micelles Exhibit Fast-Rate Binding and High Affinity toward a Protein Bed Simulating a Cell Surface. A Surface Plasmon Resonance Study. *Bioconjug Chem* **2003,** *14* (1), 177-186.

69. Bae, Y.; Jang, W. D.; Nishiyama, N.; Fukushima, S.; Kataoka, K., Multifunctional Polymeric Micelles with Folate-Mediated Cancer Cell Targeting and Ph-Triggered Drug Releasing Properties for Active Intracellular Drug Delivery. *Mol Biosyst* **2005,** *1* (3), 242-250.

70. Yoo, H. S.; Park, T. G., Folate Receptor Targeted Biodegradable Polymeric Doxorubicin Micelles. *Journal of controlled release : official journal of the Controlled Release Society* **2004,** *96* (2), 273-283.

71. Allen, T. M., Ligand-Targeted Therapeutics in Anticancer Therapy. *Nat Rev Cancer* **2002,** *2* (10), 750-763.

72. Carter, P., Improving the Efficacy of Antibody-Based Cancer Therapies. *Nature reviews. Cancer* **2001,** *1* (2), 118-129.

73. Maynard, H. D.; Heredia, K. L.; Li, R. C.; Parra, D. P.; Vazquez-Dorbatt, V., Thermoresponsive Biohybrid Materials Synthesized by Atrp. *J. Mater. Chem.* **2007,** *17* (38), 4015-4017.

74. Wang, J.; Tian, S.; Petros, R. A.; Napier, M. E.; Desimone, J. M., The Complex Role of Multivalency in Nanoparticles Targeting the Transferrin Receptor for

Cancer Therapies. *Journal of the American Chemical Society* **2010,** *132* (32), 11306-11313.

75. Torchilin, V. P.; Lukyanov, A. N.; Gao, Z.; Papahadjopoulos-Sternberg, B., Immunomicelles: Targeted Pharmaceutical Carriers for Poorly Soluble Drugs. *Proc Natl Acad Sci U S A* **2003,** *100* (10), 6039-6044.

76. Park, J. W.; Hong, K.; Kirpotin, D. B.; Colbern, G.; Shalaby, R.; Baselga, J.; Shao, Y.; Nielsen, U. B.; Marks, J. D.; Moore, D.; Papahadjopoulos, D.; Benz, C. C., Anti-Her2 Immunoliposomes: Enhanced Efficacy Attributable to Targeted Delivery. *Clin Cancer Res* **2002,** *8* (4), 1172-1181.

77. Ho, K.; Lapitsky, Y.; Shi, M.; Shoichet, M. S., Tunable Immunonanoparticle Binding to Cancer Cells: Thermodynamic Analysis of Targeted Drug Delivery Vehicles. *Soft Matter* **2009,** *5* (5), 1074-1080.

78. Reynhout, I. C.; Cornelissen, J. J.; Nolte, R. J., Self-Assembled Architectures from Biohybrid Triblock Copolymers. *Journal of the American Chemical Society* **2007,** *129* (8), 2327-2332.

79. Christensen, T.; Amiram, M.; Dagher, S.; Trabbic-Carlson, K.; Shamji, M.; Setton, L.; Chilkoti, A., Fusion Order Controls Expression Level and Activity of Elastin-Like Polypeptide Fusion Proteins. *Protein Science* **2009,** *18* (7), 1377-1387.

80. Meyer, D. E.; Chilkoti, A., Purification of Recombinant Proteins by Fusion with Thermally-Responsive Polypeptides. *Nature Biotechnology* **1999,** *17* (11), 1112-1115.

81. Meyer, D. E.; Trabbic-Carlson, K.; Chilkoti, A., Protein Purification by Fusion with an Environmentally Responsive Elastin-Like Polypeptide: Effect of Polypeptide Length on the Purification of Thioredoxin. *Biotechnol Prog* **2001,** *17* (4), 720-728.

82. Trabbic-Carlson, K.; Liu, L.; Kim, B.; Chilkoti, A., Expression and Purification of Recombinant Proteins from Escherichia Coli: Comparison of an Elastin-Like Polypeptide Fusion with an Oligohistidine Fusion. *Protein Science* **2004,** *13* (12), 3274-3284.

83. Trabbic-Carlson, K.; Meyer, D. E.; Liu, L.; Piervincenzi, R.; Nath, N.; LaBean, T.; Chilkoti, A., Effect of Protein Fusion on the Transition Temperature of an Environmentally Responsive Elastin-Like Polypeptide: A Role for Surface Hydrophobicity? *Protein Engineering Design & Selection* **2004,** *17* (1), 57-66.

84. Christensen, T.; Hassouneh, W.; Trabbic-Carlson, K.; Chilkoti, A., Predicting Transition Temperatures of Elastin-Like Polypeptide Fusion Proteins. *Biomacromolecules* **2013,** *14* (5), 1514-1519.

85. Zhulina, E. B.; Adam, M.; LaRue, I.; Sheiko, S. S.; Rubinstein, M., Diblock Copolymer Micelles in a Dilute Solution. *Macromolecules* **2005,** *38* (12), 5330-5351.

86. LaRue, I.; Adam, M.; Zhulina, E. B.; Rubinstein, M.; Pitsikalis, M.; Hadjichristidis, N.; Ivanov, D. A.; Gearba, R. I.; Anokhin, D. V.; Sheiko, S. S., Effect of the Soluble Block Size on Spherical Diblock Copolymer Micelles. *Macromolecules* **2008,** *41* (17), 6555-6563.

87. Halperin, A., Polymeric Micelles: A Star Model. *Macromolecules* **1987,** *20* (11), 2943-2946.

88. Duan, J.; Wu, J.; Valencia, C. A.; Liu, R., Fibronectin Type Iii Domain Based Monobody with High Avidity. *Biochemistry* **2007,** *46* (44), 12656-12664.

89. Richards, J.; Miller, M.; Abend, J.; Koide, A.; Koide, S.; Dewhurst, S., Engineered Fibronectin Type Iii Domain with a Rgdwxe Sequence Binds with Enhanced Affinity and Specificity to Human Alphavbeta3 Integrin. *J Mol Biol* **2003,** *326* (5), 1475-1488.

90. Binz, H. K.; Amstutz, P.; Pluckthun, A., Engineering Novel Binding Proteins from Nonimmunoglobulin Domains. *Nat Biotech* **2005,** *23* (10), 1257-1268.

91. Bloom, L.; Calabro, V., Fn3: A New Protein Scaffold Reaches the Clinic. *Drug Discov Today* **2009,** *14* (19-20), 949-955.

92. Holt, L. J.; Herring, C.; Jespers, L. S.; Woolven, B. P.; Tomlinson, I. M., Domain Antibodies: Proteins for Therapy. *Trends Biotechnol* **2003,** *21* (11), 484-490.

93. Vincke, C.; Loris, R.; Saerens, D.; Martinez-Rodriguez, S.; Muyldermans, S.; Conrath, K., General Strategy to Humanize a Camelid Single-Domain Antibody and Identification of a Universal Humanized Nanobody Scaffold. *J Biol Chem* **2009,** *284* (5), 3273-3284.

94. Headd, J. J.; Immormino, R. M.; Keedy, D. A.; Emsley, P.; Richardson, D. C.; Richardson, J. S., Autofix for Backward-Fit Sidechains: Using Molprobity and Real-Space Refinement to Put Misfits in Their Place. *J Struct Funct Genomics* **2009,** *10* (1), 83-93.

95. Davis, I. W.; Murray, L. W.; Richardson, J. S.; Richardson, D. C., Molprobity: Structure Validation and All-Atom Contact Analysis for Nucleic Acids and Their Complexes. *Nucleic Acids Res* **2004,** *32* (Web Server issue), W615-619.

96. de Marco, A., Strategies for Successful Recombinant Expression of Disulfide Bond-Dependent Proteins in Escherichia Coli. *Microbial cell factories* **2009,** *8* (1), 26.

97. Schärtl, W., *Light Scattering from Polymer Solutions and Nanoparticle Dispersions*. Springer: 2007; p 191.

98. Antonietti, M.; Bremser, W.; Schmidt, M., Microgels - Model Polymers for the Cross-Linked State. *Macromolecules* **1990,** *23* (16), 3796-3805.

99. Antonietti, M.; Heinz, S.; Schmidt, M.; Rosenauer, C., Determination of the Micelle Architecture of Polystyrene Poly(4-Vinylpyridine) Block-Copolymers in Dilute-Solution. *Macromolecules* **1994,** *27* (12), 3276-3281.

100. McDaniel, J. R.; Mackay, J. A.; Quiroz, F. G.; Chilkoti, A., Recursive Directional Ligation by Plasmid Reconstruction Allows Rapid and Seamless Cloning of Oligomeric Genes. *Biomacromolecules* **2010,** *11* (4), 944-952.

Biography

Wafa Hassouneh was born October 29th in the town of Irbid, Jordan; a nice rural town at the time. She attended University of Washington where she majored in Bioengineering and graduated with a Bachelor of Engineering in 2007. After earning her Bachelors, she came to Duke University to complete her Ph.D. work in the lab of Professor Ashutosh Chilkoti in the Biomedical Engineering department. Wafa has been a fellow in the Materials Research Science and Engineering Center (MRSEC) since 2011. She has published and coauthored the following articles:

1) Hassouneh, W., Fischer, K., MacEwan, S.R., Branscheid, R., Fu, C.L., Liu, R., Schmidt, M., Chilkoti, A., 2012. Unexpected Multivalent Display of Proteins by Temperature Triggered Self-Assembly of Elastin-like Polypeptide Block Copolymers. Biomacromolecules 13, 1598-1605.
2) Hassouneh, W.; Nunalee, M.; Shelton, M. C.; Chilkoti, A.; Calcium binding peptide motifs from calmodulin confer divalent ion selectivity to elastin-like polypeptides. Biomacromolecules. 2013 *14* (7), 2347-2353
3) Christensen, T.*, Hassouneh, W.*, Trabbic-Carlson, K., Chilkoti, A., 2013. Predicting Transition Temperatures of Elastin-Like Polypeptide Fusion Proteins. Biomacromolecules 2013 14 (5), 1514-1519

*First co-author

4) Kurzbach D., Hassouneh W., McDaniel J. R., Jaumann E.A., Chilkoti A., and Hinderberger D.; Hydration Layer Coupling and Cooperativity in Phase Behavior of Stimulus Responsive Peptide Polymers. Journal of the American Chemical Society (Just Accepted)

5) Hassouneh, W., MacEwan, S.R., Chilkoti, A., 2012. Fusions of elastin-like polypeptides to pharmaceutical proteins. Methods in enzymology 502, 215-237.

6) Christensen, T., Hassouneh, W., Callahan, DJ., Chilkoti, A., Protein Switches. In: Edward H. Egelman, editor: Comprehensive Biophysics, Vol 3, The Folding of Proteins and Nucleic Acids, Valerie Daggett. Oxford: Academic Press, 2012. pp. 238-266.

7) Hassouneh, W., Christensen, T., and Chilkoti, A. 2010. Elastin-like polypeptides as a purification tag for recombinant proteins. Curr Protoc Protein Sci 2010 Chapter 6: Unit 6.11

8) McDaniel, J.R., Bhattacharyya, J., Vargo, K.B., Hassouneh, W., Hammer, D.A., Chilkoti, A., 2013. Self-Assembly of Thermally Responsive Nanoparticles of a Genetically Encoded Peptide Polymer by Drug Conjugation. Angewandte Chemie International Edition 52, 1683-1687

9) Callahan, D. J.; Liu, W.; Li, X.; Dreher, M. R.; Hassouneh, W.; Kim, M.; Marszalek, P.; Chilkoti, A., Triple Stimulus-Responsive Polypeptide Nanoparticles That Enhance Intratumoral Spatial Distribution. Nano Lett. 2012, 12 (4), 2165-2170.